UNIVERSITAT POLITÈCNICA DE VALÈNCIA

CSIC

Consejo Superior de Investigaciones Científicas

Acoustic holograms for hyperthermia and transcranial ultrasound

Diana Andrés Bautista

Instituto de Instrumentación para Imagen Molecular (I3M)
Universitat Politècnica de València / CSIC

A thesis submitted in partial fulfillment of the requirements of the degree of
Doctor of Philosophy

May 4th, 2024

Thesis Advisors:

Noé Jiménez González	Consejo Superior de Investigaciones Científicas (CSIC)
José María Benlloch Baviera	Consejo Superior de Investigaciones Científicas (CSIC)

Thesis Jury:

Kai Melde	Max Planck Institute for Medical Research
Itzíar González	Consejo Superior de Investigaciones Científicas (CSIC)
Antonios Pouliopoulos	King's College London

Thesis Evaluators:

Athanasios Athanassiadis	Heidelberg University
Itzíar González	Consejo Superior de Investigaciones Científicas (CSIC)
Meaghan O'Reilly	Sunnybrook Research Institute

“La ciencia siempre vale la pena porque sus descubrimientos, tarde o temprano, siempre se aplican”.

Severo Ochoa

“Science is always worth it because its discoveries, sooner or later, are always applied”.

Severo Ochoa

Agradecimientos

Aún recuerdo el día en que mi profesor de la carrera de Física, Santiago González, me presentó a Paco, ante mis dudas sobre hacia dónde encaminar mi carrera profesional más allá de los estudios universitarios. Recuerdo que me habló de la investigación que hacían en su laboratorio sobre el uso de ultrasonidos para el tratamiento de enfermedades cerebrales. Nunca antes había oído hablar de ello y me impresionó bastante, sin embargo, al acabar la carrera necesitaba un cambio radical de ámbito y me fui al sector bancario. Aquella experiencia confirmó que echaba de menos la física, y me vino a la mente aquella reunión. Sin dudar contacté con Paco y, así de fácil, me vi envuelta en el maravilloso mundo de la investigación. Desde el inicio, con una pequeña beca compaginada con la realización del Máster en Física Médica, hasta la finalización de la tesis he disfrutado con esta increíble labor que no solo aporta valor a la sociedad, sino que especialmente me ha hecho crecer como profesional.

Por todo esto, mis primeros agradecimientos van a tí, Paco, por haberme mostrado la investigación y haberme acogido con tanta amabilidad y cariño en tu grupo. Un grupo que has hecho crecer enormemente desde los primeros momentos, y no sólo en número de personas, sino en complicidad y alegría. Gracias especialmente por haber entendido en todo momento mis necesidades e inquietudes y haber hecho lo posible para que yo pudiese trabajar en ellas. Por haberme valorado, haberme incluido en múltiples proyectos y haber sido tan buen líder. También a José María Benlloch, director del Instituto de Instrumentación para Imagen Molecular (i3M) y de mi tesis, por su apoyo, conocimiento y gran experiencia investigadora.

Mi mayor agradecimiento a nivel personal y laboral es para tí, Noé. Durante todo este proceso siempre has estado a mi lado, guiándome, tutorizándome y dándome increíbles

nuevas ideas (¡que no sé ni de dónde te sacas!) que me han inspirado y animado a seguir cada día. Gracias por tu enorme paciencia en mi proceso de aprendizaje, por esas muchas y muchas correcciones de manuscritos y códigos. Quiero que sepas que te admiro profundamente y eres mi ejemplo a seguir en el ámbito científico. Agradezco cada discusión científica que he tenido contigo, porque estos años han sido un no parar de aprender, pero también cada conversación fuera del laboratorio en la que has mostrado la magnífica persona que eres.

Todo este trabajo no hubiera sido posible (hubiera dimitido antes seguro) sin los mejores compañeros de laboratorio que se pueden tener. Gracias Josep, por hacerme compañía todos los días desde primera hora convirtiendo el duro comienzo de las jornadas laborales en el momento más alegre. Gracias Alicia e Irene, mi equipo ventana y mis más íntimas confesoras. Gracias a Sergio por ser mi primer mentor, y a Jandri y Quique, porque teneros de compañeros ha hecho que cada día fuera más divertido. A Juanjo, José Luis y Adrián por salvarnos de tantos apuros. A Alba, por ser mi primera y gran aprendiz, a Javi, por haberse hecho tanto de querer estos meses literalmente a mi lado, y a Suso, porque sin sus comentarios el lab no habría sido lo mismo.

Gracias a Jonathan por ser mi primer contacto internacional en esta tesis y por haberme apoyado y ayudado en la idea de los hologramas térmicos. Solo lamento no haber podido hacer una interesante visita a Estrasburgo.

Special acknowledges to Ian, Petros and Gail for making my research stay so special and fruitful, and teaching me so much about hyperthermia, ultrasound and biology. Making cell cultures and manipulating spheroids was fascinating for a physicist like me.

También agradezco a mis padres y mis tíos toda su ayuda en esta etapa de mi vida y por intentar entender qué es exactamente lo que he estado haciendo. A Jesús, Wendy, Nico y Blanca, por su comprensión y ánimos.

Finalmente, gracias Alex, por haber sido mi pilar estos años, haberme apoyado a seguir en todo lo que me he propuesto y haber decidido dar un paso más conmigo a pesar de todo el tiempo que la ciencia te ha quitado.

Abstract

Ultrasound has been used since the 1990s for the treatment of multiple pathologies thanks to its non-invasive and non-ionising nature, from localised cancer treatment to neurological therapies. The focusing of these pressure waves and beam shaping has been a problem that has been tackled from various perspectives, with the use of focusing lenses, focused transducers and the more sophisticated phased-array systems composed of multiple transducers with electronic amplitude and phase control. These systems have several drawbacks, such as the poor beam control offered by focused transducers, with a fixed focus and no control of possible field distortions introduced by the medium, or the high cost due to the complex electronics of phased-array systems, although they provide better focus control and aberration compensation.

The revolutionary idea of acoustic holograms as passive 3D printed elements came as a low-cost alternative to these previous systems. They were first described to be used in homogeneous media to generate a wide range of acoustic images, but their feasibility for focusing ultrasound beams inside the brain was soon studied and proved to be very useful in correcting the aberrations that the skull introduces into the wavefront. Holographic lenses are capable of encoding both the field to be generated and the phase distortions that may be introduced by the medium in which the ultrasound propagates.

This thesis studies the design of acoustic holograms and their application in the biomedical field. The thesis can be divided into three main parts: a first one in which new methods for the design of holographic lenses are described, a second one in which ultrasonic holograms are used for hyperthermia generation, and a third one in which their use for transcranial therapies is studied.

The first part of the thesis investigates the design of holographic lenses for transducers with spherical geometry as an alternative to the previously described flat lenses. In addition, a new method is studied to encode the acoustic field in the lenses in order to improve the image produced by them, adjusting it more closely to the desired image.

The second part studies the thermal pattern generated by the acoustic field produced by a holographic lens when it is applied to an absorbing material and how thermal diffusion affects it. This diffusion has the effect that the thermal pattern over time does not resemble the acoustic pattern, and lenses must take this process into account in their design for thermal applications, especially if uniform regions of heating are desired. The method is tested on multiple tumour spheroids, and results show that ultrasound-mediated hyperthermia is shown to be more damaging to tumour cell spheroids than traditional hyperthermia.

The third part demonstrates the feasibility of ultrasonic holograms for neural treatments, applied from the temporal window to reduce the bone heating that occurs. In addition, the acoustic field produced by holographic lenses through a macaque skull is studied in ex-vivo experiments, applying holographic projection techniques to obtain even more information from these experiments. A system is designed to apply these holograms in in-vivo experiments with macaques to test the feasibility of opening the blood-brain barrier in a localized manner.

This thesis focuses on a better design and understanding of the emerging holographic lenses, as well as on studying their validity in biomedical applications of great interest such as hyperthermia, neuromodulation and the opening of the blood-brain barrier for drug delivery to the brain.

Resumen

Los ultrasonidos se han empleado desde los años 90 para el tratamiento de múltiples patologías gracias a su carácter no invasivo y no ionizante, desde el tratamiento localizado del cáncer hasta terapias neurológicas. La focalización de estas ondas de presión y la conformación del haz ha sido un problema que desde varias perspectivas se ha intentado abordar, con el uso de lentes focalizadoras, transductores focalizados y los más sofisticados sistemas phased-array compuestos por múltiples transductores con control electrónico de amplitud y fase. Estos sistemas presentan varios inconvenientes, como el escaso control del haz que ofrecen los transductores focalizados, con un foco fijo y sin control de las posibles distorsiones del campo que puede introducir el medio, o el elevado coste derivado de la compleja electrónica de los sistemas phased-arrays, aunque proporcionan un mejor control del foco y compensación de aberraciones.

La revolucionaria idea de los hologramas acústicos como elementos pasivos impresos con tecnología 3D llegó como una alternativa de bajo coste a los previos sistemas. En primer lugar se describió su uso en medios homogéneos para generar las más diversas imágenes acústicas, pero pronto se empezó a estudiar su viabilidad para focalizar haces de ultrasonidos en el interior del cerebro, resultando ser muy útiles en la corrección de las aberraciones que el cráneo introduce en el frente de ondas. Las lentes holográficas son capaces de codificar tanto el campo que se desea generar como las distorsiones de fase que puede introducir el medio en el que se propagan los ultrasonidos.

En esta tesis se estudia el diseño de hologramas acústicos y su aplicación en el ámbito biomédico. La tesis puede ser dividida en tres grandes partes: una primera en la cual se describen nuevos métodos para el diseño de lentes holográficas, una segunda en la que

se emplean los hologramas ultrasónicos para generación de hipertermia y una tercera en la que se estudia su uso para terapias transcraneales.

En la primera parte de la tesis se investiga el diseño de lentes holográficas para transductores con geometría esférica como alternativa a las lentes planas ya descritas previamente. Además, se estudia un nuevo método para codificar el campo acústico en las lentes de forma que se mejore la imagen producida por ellas, ajustándose más a la deseada.

En la segunda parte se estudia cómo es el patrón térmico que genera el campo acústico producido por una lente holográfica cuando se aplica sobre un material absorbente y cómo afecta la difusión térmica a éste. Esta difusión tiene como efecto que el patrón térmico con el tiempo no se parezca al acústico, y que las lentes deban tener en cuenta este proceso en su diseño para aplicaciones térmicas, especialmente si se desean regiones uniformes de calentamiento. Se demuestra cómo la hipertermia generada por ultrasonidos es más dañina en esferoides de células tumorales que la hipertermia tradicional.

En la tercera parte se demuestra la viabilidad de los hologramas ultrasónicos para tratamientos neurológicos, aplicados desde la ventana temporal para reducir el eventual calentamiento del hueso que se produce. Además, se estudia en experimentos ex-vivo el campo acústico producido por lentes holográficas a través de un cráneo de macaco, aplicando técnicas de proyección holográfica para obtener aún más información de estas medidas y se diseña un sistema para aplicar estos hologramas en experimentos in-vivo con macacos y comprobar la viabilidad de la apertura de la barrera hematoencefálica de forma localizada.

Esta tesis se enfoca a un mejor diseño y entendimiento de las emergentes lentes holográficas, así como a estudiar su validez en aplicaciones biomédicas de gran interés como son la hipertermia, la neuromodulación y la apertura de la barrera hematoencefálica para la administración de fármacos en el cerebro.

Resum

Els ultrasons s'han emprat des dels anys 90 per al tractament de múltiples patologies gràcies al seu caràcter no invasiu i no ionitzant, des del tractament localitzat del càncer fins a teràpies neurològiques. La focalització d'estes ones de pressió i la conformació del feix acústic ha sigut un problema que des de diverses perspectives s'ha intentat abordar, amb l'ús de lents focalizadores, transductors focalitzats i els més sofisticats sistemes phased-array compostos per múltiples transductors amb control individual d'amplitud i fase. Estos sistemes presenten diversos inconvenients, com l'escàs control del feix que ofereixen els transductors focalitzats, amb un focus fix i sense control de les possibles distorsions del camp que pot introduir el medi, o l'elevat cost derivat de la complexa electrònica dels sistemes phased-array, encara que proporcionen un millor control del focus i compensació d'aberracions.

La revolucionària idea dels hologrames acústics com a elements passius impresos amb tecnologia 3D va arribar com una alternativa de baix cost als previs sistemes. En primer lloc es va descriure el seu ús en medis homogenis per a generar les més diverses imatges acústiques, però prompte es va començar a estudiar la seua viabilitat per a focalitzar feixos d'ultrasons a l'interior del cervell, resultant ser molt útils en la correcció de les aberracions que el crani introduïx en el front d'ones. Les lents hologràfiques són capaces de codificar tant el camp que es desitja generar com les distorsions de fase que pot introduir el medi en el qual es propaguen els ultrasons.

En esta tesi s'estudia el disseny d'hologrames acústics i la seua aplicació en l'àmbit biomèdic. La tesi pot ser dividida en tres grans parts: una primera en la qual se descriuen nous mètodes per al disseny de lents hologràfiques, una segona en la qual s'empren els

holograms ultrasònics per a generació d'hipertèrmia i una tercera en la qual s'estudia el seu ús per a teràpies transcranials.

En la primera part de la tesi s'investiga el disseny de lents hologràfiques per a transductors amb geometria esfèrica com a alternativa a les lents planes ja descrites prèviament. A més, s'estudia un nou mètode per a codificar el camp acústic en les lents de manera que es millore la imatge produïda per elles, ajustant-se més a la desitjada.

En la segona part s'estudia com és el patró tèrmic que genera el camp acústic produït per una lent hologràfica quan s'aplica sobre un material absorbent i com afecta la difusió tèrmica a aquest. Esta difusió té com a efecte que el patró tèrmic amb el temps no se semble a l'acústic, i les lents hagen de tindre en compte aquest procés en el seu disseny per a aplicacions tèrmiques, especialment si es desitgen regions uniformes de calfament. Es demostra com la hipertèrmia generada per ultrasons és més nociva en esferoides tumorals que la hipertèrmia tradicional.

En la tercera part es demostra la viabilitat dels holograms ultrasònics per a tractaments neurològics, aplicats des de la finestra temporal per a reduir el calfament de l'os que es produïx. A més, s'estudia en experiments ex-vivo el camp acústic produït per lents hologràfiques a través d'un crani de macaco, aplicant tècniques de projecció hologràfica per a obtindre encara més informació d'estes mesures i es dissenya un sistema per a aplicar estos holograms en experiments in-vivo amb macacos i comprovar la viabilitat de l'obertura de la barrera hematoencefàlica de forma localitzada.

Esta tesi s'enfoca a un millor disseny i enteniment de les emergents lents hologràfiques, així com en l'estudi de la seua validesa en aplicacions biomèdiques de gran interés com són la hipertèrmia, la neuromodulació i l'obertura de la barrera hematoencefàlica per a l'administració de fàrmacs en el cervell.

Contents

Chapter 1

Introduction

Medical use of ultrasound started back in the 1927, when it was first described for therapeutical purposes. Main applications of this technology were hyperthermia and thermal ablation, studied a lot for cancer treatment, even into the brain.Since then, several techniques have been developed to achieve targeting in a desired region from single element focused transducers to more sophisticated phased-array systems. Nevertheless, these systems present various drawbacks that need to be addressed, such as their focus quality specially into heterogeneous media and their cost of production. Acoustic holographic lenses appear as a compromise solution to solve the inconveniences encountered in these previous systems. In this first chapter, a brief introduction on the history of therapeutic ultrasound and methods to generate a quality focus are reviewed, and the new holographic techniques based on 3D-printed lenses are presented, to end with the motivation and objectives of the present thesis.

1.1 Brief state-of-the-art

Ultrasound use for body imaging is widely spread and known. Nevertheless, this is not the only potential of ultrasound in medicine. The use of these high-frequency waves for therapy inside the body can be traced back to the year 1927, when Wood and Loomis [1] reported the physical effects produced by high-intensity ultrasound in solids and liquids (radiation pressure force, heating, enhancement of chemical processes), and also in biological systems, reporting the death of bacteria, decomposition of red blood cells, and

even the death of small animals such as fish due to internal heating. Successful studies on ultrasound effects for cancer treatment date as far as back as 1944, when ultrasound was used to treat skin cancer [2], but also in the 1950's it was used to create focal and controlled lesions in the brain [3] and first reports on blood-brain barrier disruption appeared [4]. After these initial discoveries, a period of less investigation on ultrasound for therapy occurred due to negative results, specially when applying it to cancer treatment, in which studies reported no effects on cancer growth or even stimulation of it, leading even into a resolution that clinical use of ultrasound should be stopped [5]. During that period of time, ultrasound was investigated in combination with x-rays [6] and chemotherapy, reporting an enhancement of their effects due to thermal and mechanical effects produced by sound waves. At the beginning, ultrasound was applied in a continuous and high intensity manner, but studies dated from the 1970's started to study high intensity ultrasound in short pulses and also low-intensity ultrasound. Low-intensity ultrasound is defined for waves with intensities ranging from 0,125 to 3 W/cm^2 while the high-intensity term is used for waves with intensities higher than 5 W/cm^2 [7].

Since then, ultrasound for therapy has been extensively studied. There has been a great interest on applying ultrasound at high intensities for hyperthermia (tissue temperature increase from 41 to 45 C), specially as a radio- and chemotherapy sensitizer [8, 9, 10] and thermal ablation, particularly in cancer treatment [11, 12, 13, 14]. Also, the ultrasound applied in short but high intensity pulses, which is known as histotrypsy, provides a new method to ablate tissue without thermal effects [15]. Histotripsy has been demonstrated to even enhance the immune system [16] .Furthermore, ultrasound has appeared as a potential technique to perform transcranial therapy in the brain in a non-invasive and non-ionizing way. In this field of study, ultrasound has been used to perform blood-brain barrier opening (BBBO) [17, 18], allowing the dosage of specific drugs for neurological diseases' treatment such as Parkinson's disease [19] or Alzheimer's disease [20], and even for the dosage of chemotherapy in metastases treatment [21]. Other potential application of ultrasound in the brain is generating neuromodulation when applying ultrasonic waves in a low-intensity manner [22, 23], and precise brain surgery without the need of removing the scalp at high intensities [24]. Thermal ablation of a region in the thalamus called the ventral intermediate nucleus (Vim) with ultrasound is an effective treatment of the essential tremor [25].

1.2 Motivation

In all the above presented applications, and specially in those involving the high impedance barrier that presents the skull, one main concern is the correct application of the ultrasound energy only in an area of interest. In early studies, the way to generate the ultrasound waves was with plane transducers made from quartz crystals. These transducers were arranged in a particular way to obtain an overlap of several transducer beams into the target [3], or a plastic focusing lens attached to a single element transducer to obtain a net energy focus [26, 4].

Gruetzmacher was the first to suggest giving a concave curvature to the quartz crystal [27], whilst Lynn et al [28] were the first to apply this extracorporeal technique into the brain of five animals to study the biological effects of ultrasound. This same group developed a system to focus energy into a spot using reflectors which allow them to reduce side lobes in the focus compared to the other developed techniques, but found it more difficult to locate the focusing region [29]. In the 1970's, coinciding with the renewed interest in ultrasound for therapy, piezo-ceramic materials were discovered such as the barium titanate (BaTiO3) and the lead zirconate titanate (PZT), facilitating the manufacturing of ultrasonic transducers and increasing their output power [30]. Single-element piezo-ceramic focused transducers have been widely used for ultrasound therapy, e.g. for cancer treatment [31]. They have also been applied to focus ultrasound beams through the skull [32, 33, 34]. Even though single-element focused transducers allow focusing ultrasonic energy in an area of interest, in transcranial applications the skull introduces great focal distortions and aberrations. This is caused by the uneven refraction, absorption and scattering phenomena generated by the irregular skull bones. Also, the characteristic focus of each transducer cannot be modified in position, shape or dimensions, so for some applications like sonicating a whole tumour might require translation and rotation of the transducer to cover the area of treatment.

To overcome these inconveniences, phased array systems were proposed for therapy, even though they have already been used for ultrasound imaging [35]. This technology has been developed for therapy since the 1980's, studying various distributions of the elements [36, 37, 38] and optimal phase shifts to obtain the desired ultrasound beam [39]. In phased-array systems, the elements must be spaced a distance shorter than half wavelength from centre to centre to obtain a full range of steering angle. However, due to the poor scalability of the electronics, the total number of elements is limited. In addition, therapeutic phase arrays require a large surface to generate intense fields. Therefore, usually the elements of a therapeutic phase array are larger than a wavelength. This results in a limited steering range due to the emergence of secondary grating lobes and the narrow directivity of each individual element [40]. To mitigate this problem, sparse distributions of elements have been proposed [41, 42], but in these systems less area is

emitting and thus energy at the focus is lost. Other arrangements based on Fresnel spirals have been studied to overcome both problems [43], and even designed with previous simulations to maximize the gain at the focus while getting less grating lobes [44].

The main advantage of these systems is that they are able to cover a wide area by scanning several spots within the target as they allow a fast steering of the focus and the generation a homogeneous region of hyperthermia with little temperature fluctuation [45], adapting this region into a volume or a desired shape [46]. Another strength of these systems is their ability to correct the wavefront aberrations that appear in the propagation of ultrasonic waves into heterogeneous media, specially when propagating through the skull. In this sense, each individual emitted signal can be modified in phase and amplitude to compensate the aberrations introduced by the skull [47]. Phased-array systems can generate precise thermal ablation inside the brain and blood-brain barrier opening. Examples of these systems are the Exablate Neuro (TM) (InSightec, Hayfa, Israel) [48] which consists on 1024/2048 small elements distributed into a helmet-shaped structure, or the NaviFus system (NaviFus, Taipei City, Taiwan), a hemispherical phased-array [49]. Also, other clinical systems as the Sonalleve MR-HIFU employ advanced phased-array technology mainly for hyperthermia in organs located at the abdominal cavity [50]. Despite the great reception and track record of these systems, their complicated electronics makes them high-cost devices that can be sometimes unaffordable for certain medical facilities and applications. In addition, although some phased-array systems such as NaviFus use neuronavigation guidance, others such as Exablate Neuro use a magnetic resonance imaging (MRI) system due to their therapeutic accuracy requirements, making them even more expensive in economic and logistical terms.

3D printed holographic lenses appeared as an alternative to the previous systems. These devices were first proposed by Melde et al. for homogeneous media [51] as an analogue of optical holograms. Computer-generated holograms are able to codify the information of the wavefront needed to create an acoustic image in a desired region into a monolithic lens, in which each pixel acts as an acoustic source. With these elements, they have proven that obtaining good quality images is possible. For example, the complex acoustic images retrieved have been applied for contactless particle trapping and manipulation using a simple device. The main advantages of these lenses are their low-cost and their ease of production, providing an accurate control over the phase distribution due to their multiple emitting elements [52]. Nevertheless, they present some drawbacks. Conventional 3D-printed acoustic holograms are not reconfigurable, i.e. they need to be made specifically for each application and desired image, and also they are not able to completely codify both amplitude and phase information. Different groups have been working on optimizing acoustic holograms to overcome these disadvantages and offer new solutions. Brown et al. have designed holograms able to codify different images at the same position for various driving frequencies [53], stackable holograms that can be

relocated to create different images [54], and also holograms able to codify phase and amplitude with two lenses [55]. Recently, Melde et al. have shown for the first time the creation of 3D holographic images using three steered transducers and one lens coupled to each of them [56] and applied it to matter assembly. Holographic lenses have also been used in combination with phased-arrays with low number of elements to enhance their potential as certain electronic steering can be achieved with these systems. Using multilayer holograms that form a multiplanar diffractive acoustic network, different patterns can be reconfigured by switching phased-array elements [57].

Applications of holographic lenses are multiple, for both industrial and biomedical fields. In biomedicine, some discussed applications are cell-patterning [58], the creation of cavitation patterns inside bubble-filled phantoms [59], matter assembly [56] or their use for lithotripsy [60].

Other biomedical application of ultrasonic holograms which is attracting great interest is their use for brain therapy. In this case, instead of being designed for an homogeneous or quasi-homogeneous media, holograms should capture all the information of phase aberrations introduced by the skull and be able to correct them. First, holographic lenses were described to correct skull aberrations and create a single focus on a location of interest [61] and their robustness to location misalignment was measured [62]. Later, more complex aberration-corrected holograms were designed to be focused inside the skull [63], and were tested ex-vivo to encode acoustic vortices [64]. Acoustic vortices in the brain allow transferring angular momentum and study neuromodulatory responses, but also would allow for particle trapping and moving in the event that a blood clot blocks a cerebral vein. Several studies have been performed in-vivo with small animals to generate bilateral blood-brain barrier opening (BBBO) [65, 66] or neuromodulation via lineal momentum transfer[67].

Figure 1.1 is shown to illustrate how holographic lenses correct skull aberrations and even adapt the focus to a desired area of interest. In Figure 1.1(a) the natural focus of a 500 kHz focused transducer in water is presented. Then, the same transducer is considered for a transcranial application, and Figure 1.1(b) shows how the focus is aberrated by the skull. This image exemplifies how the focal quality of a focused ultrasound beam is decreased when using single-element focused transducers for brain therapies. Finally, the problem is compensated by using a lens made to correct the specific phase shifts introduced by the cranial bones (Figure 1.1(c)). Moreover, holographic lenses can go beyond correcting aberrations and are able to focus the acoustic energy in a desired brain structure, like the hippocampus presented in Figure 1.1(d).

Throughout the introduction, the strengths and weaknesses of 3D-printed holographic lenses have been presented. They are used as a low-cost alternative for precise wavefront

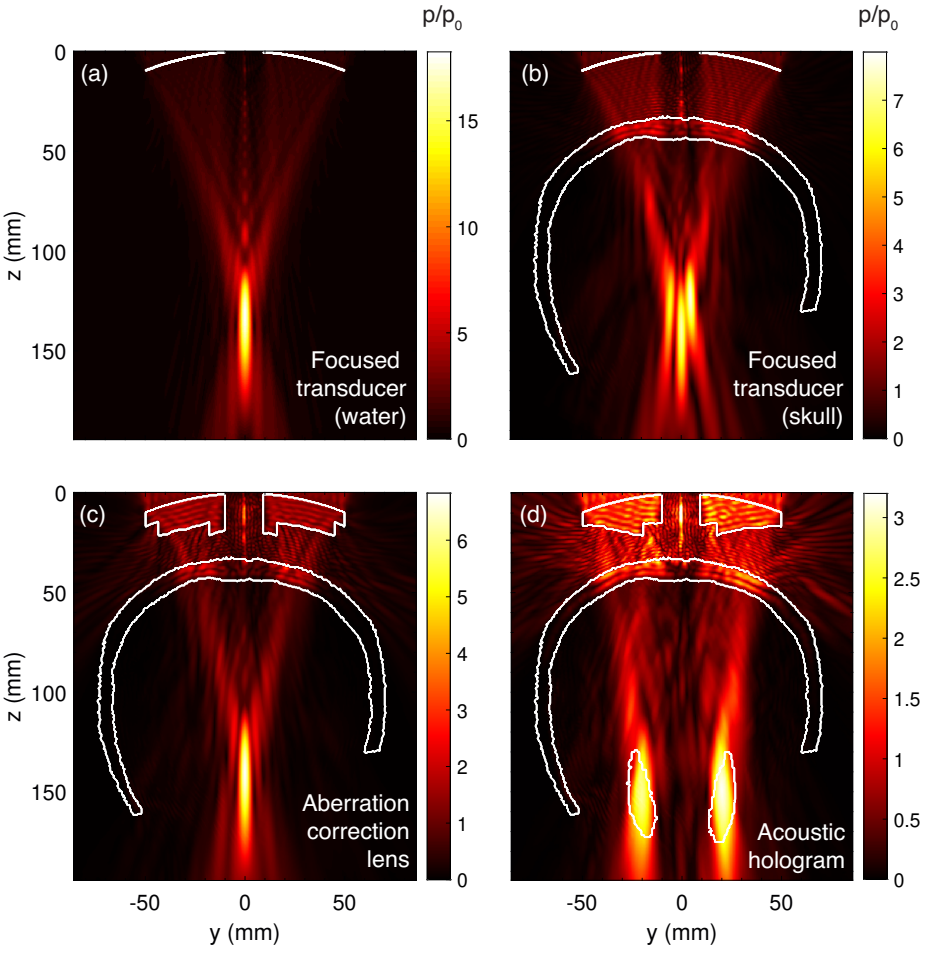

Figure 1.1: (a) Focused transducer focus in water. (b) Focused transducer focus in water after trespassing the skull. (c) Acoustic lens used to correct skull aberrations. (d) Aberration-corrected acoustic hologram adapted to both hippocampus

control to phased-arrays systems. Nevertheless, improvements on their design need to be implemented to become as competitive as their high-cost analogous.

1.3 Thesis objectives

The objective of this thesis is, on the one hand, to develop new methods to generate holographic lenses with the aim of better encoding the necessary phase field to create a desired acoustic image and, on the other hand, to explore further biomedical applications of them, mainly focused on hyperthermia and transcranial ultrasound.

This dissertation is structured in nine chapters, including this first introductory chapter. On Chapter 2 a new method to design lenses adapted to focused transducers is presented and compared to other methods described in previous works, which were based on flat lenses coupled to the transducer through a bulk of lens material. On Chapter 3, a new method to create acoustic holograms is explored, based on matching the phase of the acoustic field of the desired image and the phase of the transmission coefficient of the lens for each possible lens height. In Chapter 4, it is presented the use of acoustic holograms to generate controlled thermal patterns and their potential use in hyperthermia applications, with measurements in ex-vivo tissue and phantoms with an infra-red camera and using MRI-thermometry. Chapter 5 presents an application of these acoustically-induced thermal patterns to expose several cancer-cell spheroids to an homogeneous temperature field and thus to the same thermal dose, and study their response in a 10-day basis. Transcranial applications of acoustic holograms are presented in Chapters 6, 7 and 8. Chapter 6 is a numerical study on how holographic lenses perform when applied through the temporal bone window and their robustness under displacements and rotations of the skull. In Chapter 7 holography is presented for both designing a lens to focus on a specific target inside a macaque's skull and to experimentally evaluate this field. The whole 3D volume of the acoustic image, its shape and dimensions are retrieved with holographic projection techniques. Finally, Chapter 8 presents the design and calibration of an experimental setup to produce in-vivo BBB-opening inside a macaque's brain in the frame of a collaboration with HM-CINAC. The final chapter brings all the thesis ideas together and contains general conclusions and potential future works.

Chapter 2

Holograms in curvilinear coordinates

Holographic lenses are usually described to be coupled with plane transducers. To have a good coupling with this geometry, they are designed as a planar surface on the one side and with pixels on the other side. Nevertheless, holographic lenses can also be coupled with focused transducers, whose geometry is semi-spherical. This can be accomplished following two strategies. On the one hand, the curvature of the transducer can be compensated and obtain a flat lens with a bulk of lens material and, on the other hand, it can be designed a curvilinear hologram that matches the geometry of the transducer and whose pixels have the shape of truncated pyramids. In this Chapter we describe the design of both lenses and analyse their response in terms of focus gain, shape and location.

2.1 Introduction

Acoustic lenses have been used mainly to focus the ultrasonic waves coming from a planar transducer. These lenses were designed with different geometries, normally with spherical [3] or elliptical [68] shape, aiming to concentrate all the acoustic energy into a single focus. Other approaches used annular lenses to produce two foci [69] or lenses with sectorial design to generate annular focusing [70], inspired in the same spherical geometry.

These lenses, despite they had a good performance, were too large for some medical applications [71]. Several studies were then performed to make focusing lenses with lower profiles, like using binary lenses with phase-shifting regions [71] and based on Fresnel zone plates [72], with the possibility to not only focus the ultrasound but also generating acoustic vortices [73].

Recent works using 3D-printed holographic lenses to adapt a transducer's focus into a desired region and even correcting skull aberrations are described for flat transducers, in the form of thin phase plates [51, 63] or unwrapped phase profiles [61]. There is not much work about acoustic lenses to tune the focus of a curved transducer. Wu et al. theoretically described flat lenses to disperse the waves coming from a focused transducer into several foci to create a volumetric focusing [74] and Lalonde et al. designed a flat lens coupled to a curved transducer to generate three foci [75]. Recently, Jiménez-Gambín et al. designed flat lenses that adapted to the curvature of the transducer with a bulk of the same lens material [64].

In this Chapter we describe a new method to design curvilinear holograms that couple to focused transducers and compare this method with that described by Jiménez-Gambín et al. [64] on their work, where a bulk of lens material was used as coupling between the transducer and a flat lens.

2.2 Materials and methods

2.2.1 Lens design

The first step of the lens design consists in calculating the field radiated by a set of virtual sources distributed over the target area. The resulting wavefront, $P(\mathbf{r}_0)$, is recorded at the holographic surface, located at coordinates $\mathbf{r}_0 = (x_0, y_0, z_0)$. The field is complex-conjugated to produce a time-reversal version of the recorded wavefront at the desired frequency, $P^*(\mathbf{r}_0)$, and only the phase of the hologram is retained.

When we want to use a focused transducer to produce a hologram we can study different strategies. One option is to design a flat lens and locate it on the top of the curved transducer, using the same lens material as the coupling medium, filling the gap between the transducer and the exit plane of the corresponding flat lens (bulk holograms). Another option is to create a lens with the same curvature of the transducer that couples directly to it (curvilinear holograms).

Bulk holograms for focused transducers

The bulk lens need to compensate for the phase profile introduced by the curved transducer, which is described by:

$$P_t = \exp\left(ik_L\sqrt{r^2 + F_t^2}\right), \tag{2.1}$$

where $k_L = 2\pi f_0/c_{L,0}$ is the wave number at the lens material, with f_0 the transducer central frequency and c_L the sound speed in the lens. F_t denotes the radius of curvature of the transducer and r the coordinates of the points of evaluation. These points of evaluation are defined as the points of the holographic surface. In this same surface we record the wavefront produced by the virtual sources, P_s. The phase profile codified is the composition of these two wavefronts considering their propagation direction as

$$P = P_s^* P_t^*, \tag{2.2}$$

where the operand $(\cdot)^*$ denotes complex conjugation. A schematic of this process can be seen in Figure 2.1 (a).

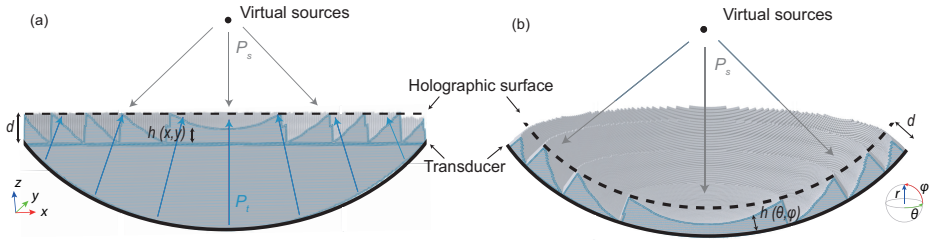

Figure 2.1: (a) Schematic of how bulk holograms are designed, with each pixel's height calculated in cartesian coordinates. (b) Schematic of how curvilinear holograms are designed, with each pixel's height calculated in spherical coordinates.

Holograms in curvilinear coordinates

On the one hand, for the bulk lens, the surface at the exit plane of the transducer is divided into square pixels of different height. On the other hand, to design the curved lens, a uniform cartesian grid is designed and projected on the curved surface. This simple procedure results in a very uniform pixel distribution for moderately focused sources. Note that a spherical coordinate grid will produce much smaller pixels at the centre of the source. A schematic of this process can be seen in Figure 2.1 (b)

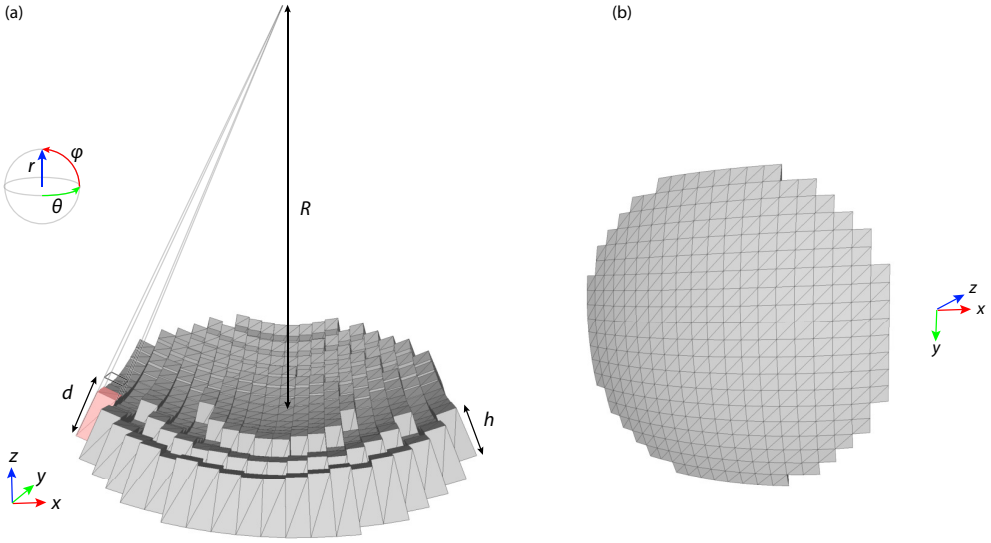

Figure 2.2: (a) Detail of the curvilinear hologram design. Each pixel is constructed as a truncated pyramid pointing at the radius of curvature of the transducer, as schematically seen for the red pixel. (b) Bottom of a curvilinear hologram where the geometry of each pixel is shown.

Lens building

In both cases, we design the lens height profile using the phase information at each pixel of the holographic surface, located at a distance d from the transducer surface, assuming that each pixel vibrates longitudinally as an elastic Fabry-Perot resonator. To design the bulk hologram, the column height is computed in cartesian coordinates $h = h(x_0, y_0)$, each column presenting the shape of an orthohedron. For the curvilinear hologram, the height of each pixel is calculated in spherical coordinates $h = h(\theta_0, \phi_0)$. Therefore, each pixel presents the shape of a truncated pyramid, with the chopped apex located at the center of curvature of the spherical surface, as can be seen in Figure 2.2 (a). Note that the top and bottom faces of the pyramidal frustum are non-congruent squares, but in practice these faces are very similar and pixels resemble orthohedrons because the lens in thin and located far from the center of curvature of the focused source, R. In this way, all pixels of the resulting lenses are perpendicular to the radiating surface. Figure 2.2 (b) shows the shape of the curvilinear hologram at the bottom. Each pixel has a squared base but with a certain curvature adapting to the transducer surface.

The complex frequency-dependent transmission coefficient of each Fabry-Perot resonator, measured in a surface parallel to the transducer and at a distance $d = z_h$ in cartesian co-

ordinates for the bulk hologram case (and would apply for a flat transducer as well), and $d = r_h$ in spherical coordinates for the curvilinear hologram, is given by

$$T = \frac{2Z_n e^{-ik_0(d-h)}}{2Z_n \cos(k_L h) + i(Z_n^2 + 1)\sin(k_L h)}, \tag{2.3}$$

where $Z_n = Z_L/Z_0$ is the normalized impedance, $Z_0 = \rho_0 c_0$, $k_0 = \omega/c_0$, c_0, ρ_0 and $Z_L = \rho_L c_L$, $k_L = \omega/c_L$, c_L, and ρ_L, are the acoustic impedance, wavenumber, sound speed, and density in water and in the lens material, respectively.

The phase of transmitted acoustic waves can be varied from 0 to 2π tuning the height of each pixel. As an analytic inversion of Eq. (2.3) is not possible due to the trigonometric functions, we must use an interpolation method of this expression to estimate the height of each pixel that fulfils $\arg(P^*) = \arg(T)$. In this way, we obtain the height of all pixels of the holographic lens that will generate the desired acoustic image. As a result, each pixel of the hologram acts as a phased-array emitter, enabling a fine control of the generated phase profile.

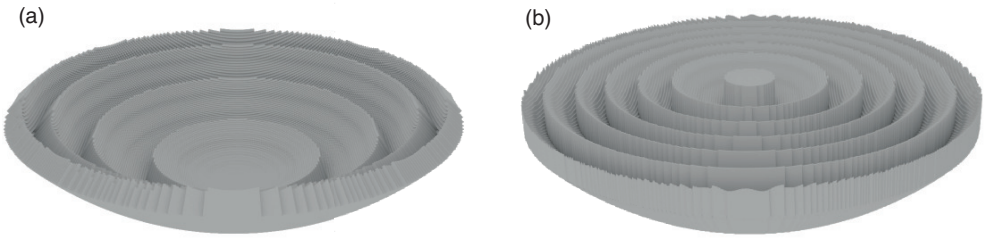

Figure 2.3: 3D models of lenses made for a focused transducer with 100-mm aperture 100 mm and radius of curvature of R=60 mm to focus at F=50 mm from the transducer surface. (a) Curvilinear hologram and (b) bulk hologram.

2.2.2 Simulations

Calculations of the acoustic field resulting from the radiation of the virtual source or sources and transducer are made using a pseudo-spectral time-domain method implemented in the Matlab package *k-Wave* [76]. This method allows to calculate the pressure field in a heterogeneous and absorbing media in a faster way than calculations using finite-difference time-domain (FDTD) methods as it can use a coarse spatiotemporal numerical mesh, e.g. theoretically they can use 2 points per wavelength instead of the 10 points per wavelength required in the FDTD calculations. The three-coupled first-order

partial differential equations solved are the continuity equation, the momentum conservation equation and the pressure-density relation:

$$\frac{\partial \rho}{\partial t} = -\rho_0 \nabla \cdot \vec{v} - \vec{v} \cdot \nabla \rho_0, \tag{2.4}$$

$$\frac{\partial \vec{v}}{\partial t} = -\frac{1}{\rho_0} \nabla p, \tag{2.5}$$

$$p = c^2(\rho + \vec{d} \cdot \nabla \rho_0 - \mathbf{L}\rho), \tag{2.6}$$

where ρ_0 is the equilibrium density, ρ is the acoustic density, p is the acoustic pressure, c_0 is the medium sound speed, $\vec{d}$ is the acoustic displacement of the particle, $\vec{v}$ is the acoustic particle velocity, and $\mathbf{L}$ is an integro-differential operator that takes into account acoustic absorption and scattering and follows an exponential relationship with frequency, characterized by $\alpha(\omega) = \alpha_0 \omega^\gamma$ where α_0 is the absorption coefficient and γ is the exponent of the frequency power law, both characteristics of each material.

Two simulations are performed to evaluate each case. First, a backward simulation is performed, where the virtual source or sources are the origin of spherical pressure waves. The acoustic wavefront resulting from the interaction of the multiple sources fields is recorded at the holographic surface. The complex-conjugated phase information of the wavefront in this surface is used to design the lens. Second, a forward simulation where the designed lens is considered and the transducer is the emitter of sound waves is performed to check the resulting field.

Each source is set to radiate a sinusoidal continuous wave at the central frequency of the transducer, which is set to 500 kHz. The used grid have a homogeneous spatial step of $\Delta x = \lambda/6 = 0.491$ mm and a temporal step of $\Delta x = 71.4$ ns. These parameters are fixed for both backward (when the virtual source radiates) and forward (when the transducer is the acoustic source) simulations.

2.2.3 Studies

To evaluate and compare the performance of bulk and curvilinear holograms, two studies have been carried out.

First, a study with different focused transducers with a fixed aperture of 100 mm and a radius of curvature equivalent to a desired f-number, which were of 0.6, 0.8, 1 and 1.4, in which the main objective was to focus on its axis at different depths, controlling the

axial location with both kind of lenses. In this study, only water medium was considered with sound speed and density of c_0 = 1483 m/s and ρ_0 = 1000 kg/m^3, respectively, and the 3D-printing lens material (Clear resin, Formlabs), whose acoustic properties were evaluated at our laboratory and have a value of sound speed and density of c_L = 2600 m/s and ρ_L = 1186 kg/m^3 respectively [77]. Absorption coefficient of water was set to 0.0013 dB/(cm·MHz$^\gamma$) given by the fitted experimetal data of Pinterkon [78] and the absorption coefficient of the lens to 2.95 dB/(cm·MHz$^\gamma$), with γ = 1.1, according to previously reported values for similar photopolymers [51].

Second, a study considering an ex-vivo skull, cut and empty, and aiming to a bilateral focusing with both kind of lenses. For this study, transducers with f-numbers of 0.6 and 1.4 were considered. Properties of the skull were obtained from a CT image with a spatial resolution of 0.33×0.33×1.25 mm^3. The skull was interpolated to the resolution of the simulation grid and the CT values of linear x-ray attenuation in Hounsfield units were converted into sound speed and density values using empirical linear relationships [79, 80]. Values of mean and maximum sound speed and density at the skull are the following: $c_{\mathrm{mean}} = 2114$ m/s, $c_{\mathrm{max}} = 2939$ m/s, $\rho_{\mathrm{mean}} = 1466$ kg/m^3, $\rho_{\mathrm{max}} = 2072$ kg/m^3. Acoustic attenuation was set constant in all the skull and with a value of 8.371 dB/(cm·MHz$^\gamma$), according to bibliography [81]. All the medium surrounding the skull was water.

2.3 Results

2.3.1 Single focus

Results of gain in the focus are shown in Figure 2.4. As shown in this graph, higher gains are obtained for curvilinear holograms compared with its equivalent bulk holograms when focusing at closer distances to the transducer than its corresponding radius of curvature ($F < R$) for all geometries. The difference in gain is higher as the f-number is smaller, i.e. for highly focused transducers. For these highly focused transducers and when the lens focus is far from the transducer focus, the resulting curvilinear holograms have a strong defocusing geometry. For these unusual cases in which a highly focused transducer is used to focus on locations further from its radius of curvature, bulk holograms perform better in terms of focus gain and quality. It can be seen that for f-numbers of 0.6, when focusing closer than 60 mm the optimal hologram in terms of gain and focus location is the curvilinear one and the same is observed for an f-number of 0.8 when focusing closer than 80 mm, whilst a bulk hologram should be used when wanting to focus further. On the other hand, for moderately focused transducers, in general it is

preferable to use curvilinear holograms due to their higher gain by not having the lens material filling the curvature of the source.

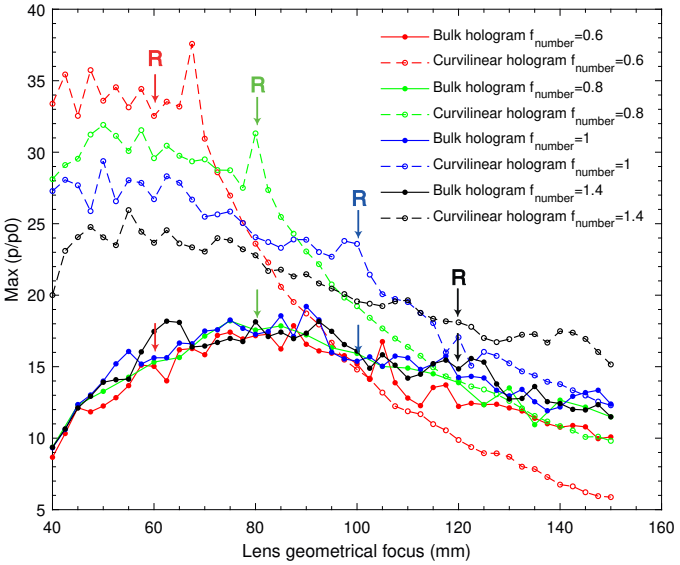

Figure 2.4: Gain at the focus location for bulk lenses (continuous line) and curved lenses (dashed line), for transducer with f-numbers of 0.6 (red line) 0.8 (green line) 1 (blue line) and 1.4 (black line). The letter R in the graph represents the radius of curvature of each transducer.

In terms of focus location, shown in Figure 2.5, a similar effect is seen. When focusing near the transducer, all geometries present a similar behaviour. For transducers with small f-number, focusing location starts to change at the natural focus of the transducer, when the optimal focusing is achieved, but when using curvilinear holograms these are not able to get a good quality focus and with a controlled location at further locations. For very narrowly focussed transducers, this effect is not seen when using curvilinear holograms. In all cases, bulk holograms present a more constant focusing location, even though failing to maintain the focus location at far distances. The main difference is that for curved lenses, they fail to focus further from the natural focus of the transducer, but for bulk holograms the focus location is constant for all transducers, bringing the focus closer to the transducer when focusing at longer distances.

In Figure 2.6 fields produced by both kind of lenses in the case of a highly focused transducer are shown. Figures 2.6 (a) and 2.6 (b) present the acoustic field produced by a bulk hologram and a curvilinear hologram, respectively, when focusing at a distance

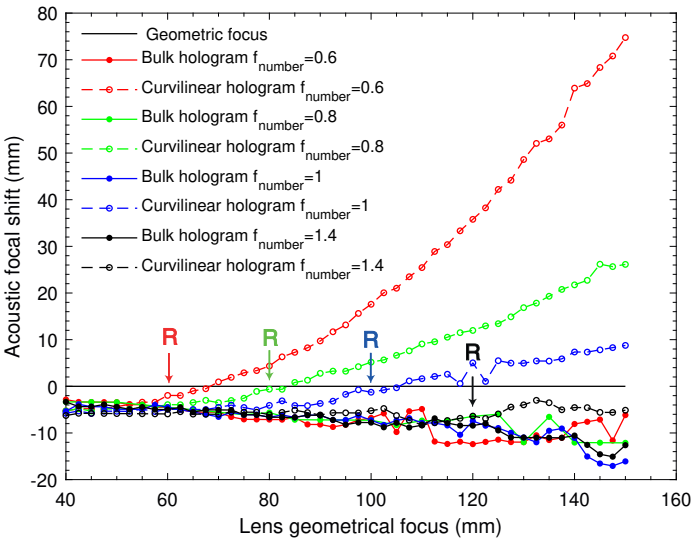

Figure 2.5: Location of the maximum for bulk lenses (continuous line) and curved lenses (dashed line), for transducer with f-numbers of 0.6 (red line) 0.8 (green line) 1 (blue line) and 1.4 (black line). The letter R in the graph represents the radius of curvature of each transducer.

smaller than the radius of curvature of the transducer. It can be seen that the focus gain and quality is much better in the case of the curvilinear hologram. Figures 2.6 (c) and 2.6 (d) show the same fields but when focusing at a distance further from the transducer. In this case, the bulk hologram compensates the curvature of the transducer and is able to focus at the desired distance whilst the curvilinear hologram presents several lobes at the axis and a last maximum at a distance 80 mm further from the desired distance.

2.3.2 Transcranial scenario

In this case, both extreme cases with f-numbers of 0.6 and 1.4 have been studied. In both cases, two virtual sources were located inside the ex-vivo skull, at a depth of 107 mm and separation of 35 mm (17.5 mm from the centre of the skull). When using the transducer with the small f-number, using the bulk hologram two defined foci appeared at 114 mm with gains of 3.1 p/p_0 (focus at -17 mm) and 3.3 p/p_0 (focus at 17 mm) (Figure 2.7 (a)), whilst for the curved lens these two foci were at an axial distance of 144 mm, with gains of 3.8 p/p_0 (focus at -21 mm) and 3.9 p/p_0 (focus at 21 mm) (Figure 2.7 (b)). When using the transducer with the highest f-number, using the bulk hologram two

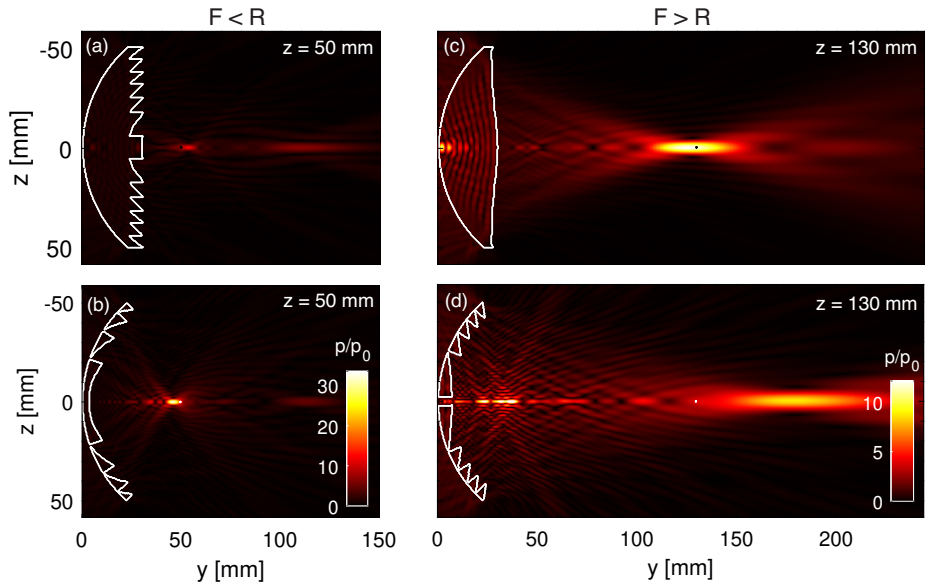

Figure 2.6: Acoustic fields for a transducer with f-number = 0.6. (a) Bulk hologram to focus at z=50 mm. (b) Curvilinear hologram to focus at z=50 mm. (c) Bulk hologram to focus at z=130 mm. (d) Curvilinear hologram to focus at z=130 mm.

foci appeared at 115 mm with gains of 5.6 p/p_0 (focus at -17 mm) and 5.1 p/p_0 (focus at 17 mm) (Figure 2.7 (c)), whilst for the curved lens these two foci were at an axial distance of 113 mm, with gains of 5.6 p/p_0 (focus at -17 mm) and 5.4 p/p_0 (focus at 17 mm) (Figure 2.7 (d)).

This example shows that for very focused transducers, when using curved lenses they fail to set the focus at the desired distance, bringing it further from the transducer, as discussed in the previous section. Bulk lenses bring the focus at the correct place but present a significant loss in gain mainly due to the important bulk of lens material. For slightly-focused transducers, both lenses present a similar behaviour, with a higher gain when using curved lenses.

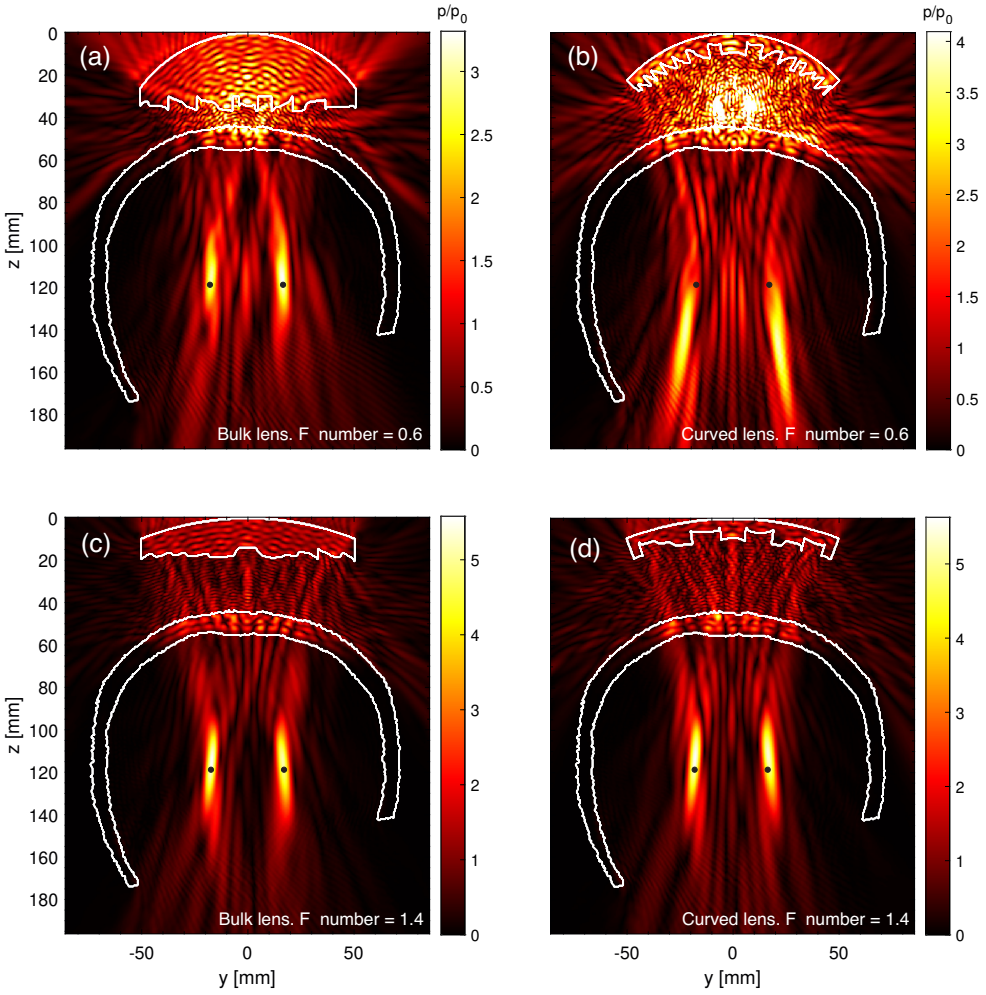

Figure 2.7: Simulations for bilateral focusing through an ex-vivo skull in water. (a) Using transducer with f-number of 0.6 and bulk lens. (b) Using transducer with f-number of 0.6 and curved lens. (c) Using transducer with f-number of 1.4 and bulk lens. (d) Using transducer with f-number of 1.4 and curved lens.

2.4 Chapter conclusions

In this Chapter, we have presented two methods to design holographic lenses for focused transducers. Two different approaches, curvilinear holograms and bulk holograms, have been discussed, one designing the lens adapting to the geometry of the transducer, in which the pixels are perpendicular to the transducer's surface at each point and are designed as truncated pyramids, and a second designing a bulk lens that fills all the curvature of the transducer. Both strategies have been studied to focus at different locations in the axis of the transducer, for focused transducers with f-numbers of 0.6, 0.8, 1 and 1.4. Curvilinear holograms present better gain when focusing near the transducer, specially for transducers with small f-numbers, which are the more common in these holographic applications. In the odd case of trying to focus beyond the natural focus of the transducer, specially for small f-number transducers, these lenses are not able to bring the focus at the desired place and bulk holograms are preferable despite the loss in gain due to the absorption of the lens material.

A transcranial propagation scenario has been studied, aiming to create a double focus inside a skull and correcting the aberrations introduced by the bones. Two extremal cases have been evaluated: one using a transducer with an f-number of 0.6 and other with an f-number of 1.4, both using bulk and curvilinear holograms and aiming to target the same spots. Results show the same trend: when using slightly focused transducers, curvilinear holograms are preferable due to their better gain at the focus. When aiming to a distance further than the natural transducer's focus, specially for highly focused transducers, bulk holograms are preferable. To give an example of clinical applications, when focusing on the motor cortex to study neuromodulation effects of ultrasound we would be, in general, focusing nearer from the transducer than its radius of curvature, but whilst focusing on deep brain targets, normally for neuromodulation or blood-brain barrier opening applications, we would be probably focusing further from the radius of curvature of the transducer. Is important to keep this in mind to use the optimal hologram for each application depending on the transducer being used.

Along this thesis, when designing lenses for focused transducers, the curvilinear hologram strategy is going to be followed for its better focusing and the lack of absorption in a bulk of lens material, always considering the region where these lenses present a better performance.

Publications

Results related with this Chapter have been presented in the following publications:

Journal papers

Andrés, D., Jiménez-Gambín, S., J., Jiménez, N., & Camarena, F. (2021). Hologramas acústicos multifocales para el tratamiento con ultrasonidos de estructuras cerebrales profundas. Revista de Acústica, 52(1-2), 17-25.

Conference papers

Andrés, D., Jiménez-Gambín, S., J., Jiménez, N., & Camarena, F. Multifocal acoustic holograms for ultrasound focusing at deep-brain structures. *TECNIACUSTICA 2020. XI Congreso Ibérico de Acústica. 51 Congreso Español de Acústica*. Online. October 21-23, 2020. Published by *Sociedade Portuguesa de Acústica (SPA) (ISBN: 978-989-33-1221-6)*. **Award: Premio Andrés Lara para Jóvenes Investigadores**.

Andrés, D., Jiménez-Gambín, S., J., Jiménez, N., & Camarena, F. Multifocal acoustic holograms for deep-brain neuromodulation and BBB opening. *2020 IEEE International Ultrasonics Symposium (IUS)*. Online. September 6-11, 2020. Published in *Proceedings of the 2020 IEEE International Ultrasonics Symposium (IUS) (ISBN:978-1-7281-5448-0)*

Andrés, D., Jiménez-Gambín, S., J., Jiménez, N., & Camarena, F. Transcranial multifocal acoustic holograms. *7th International Symposium on Focused Ultrasound*. Online. November 10-13, 2020.

Andrés, D., Míguez-Abad, D., Jiménez-Gambín, S., J., Jiménez, N., & Camarena, F. Hologramas acústicos bilaterales para terapia transcraneal. *III Jornadas RSEF (Real Sociedad Española de Física) / IFIMED de Física Médica*. Online. December 14-15, 2020.

Chapter 3

Field-matching holograms

Acoustic holograms are gaining importance due to their multiple biomedical and industrial applications. Generating holograms with 3D-printed materials, i.e. with holographic lenses, makes it very economical and affordable. Nevertheless, the creation of these lenses to accurately codify the full amplitude and phase information of a desired acoustic image is challenging and needs of further improvements. In this Chapter, we investigate a new phase-only holographic lens design technique that aims to create a perfect match between the field we want to reconstruct and the field created by the lens in each of its pixels. This is accomplished by recording the field information and performing the matching with the transmission coefficient of the lens material in a volume instead of in a plane as done in previous works. In this way, we capture the full angular spectrum of the wavefront beyond the thin lens approximation. This technique paves the way to a better understanding of holographic lenses and provides an accurate method for designing acoustic holograms.

3.1 Introduction

Acoustic holographic lenses, first described by Melde et al. [51], are based on the coding of a wave phase profile into the height of pixels in a lens that can be printed afterwards. This coding is performed in a planar surface in front of the transducer, usually called the holographic plane, and the lens is designed so that at each pixel location the amount of lens material provides of the desired phase change at the holographic plane. Several op-

timization methods are used to calculate the acoustic wavefront at the holographic plane, like iterative angular spectrum (IASA) [51, 55], the iterative back propagation (IBP) method [82], or even more sophisticated propagators based on a phase-only, gradient-descent algorithm with automatic differentiation [83]. Other methods can be used to calculate the wavefront information, specially when a heterogeneous medium is considered, like the time-reversal method [63] or the angular spectrum method adapted to these media [84]. However, one thing is to know the required phase of the wavefront at one location, and other thing is to find a lens geometry that exactly produces that phase distribution at that location. Usually, efforts are done on finding the former, but to solve the latter, an accurate lens topology is needed. Common topologies for 3D printing materials used in ultrasonics assume a linear (or quasi linear) relation between the phase and the local lens height [51, 55, 63, 61]. Nevertheless, that relation is only valid in the thin lens approximation, as we will show here.

In this Chapter we describe a new method, that we are going to call field-matching holograms, to encode phase information for 3D holographic lenses design, based on recording the phase in a holographic volume instead of just in a plane and match this information with the phase given by the transmission coefficient of the lens material for every possible lens height.

We are going to study the advantages and limitations of field-matching holograms and their performance and characteristics when using them to focus on a single location and when using them to codify more complex fields (holograms). The study in this Chapter will be carried out for 50-mm aperture flat transducer and central frequency of 1.1 MHz. The performance of these new lenses will be compared to that of classical holographic lenses, referred to as single-plane holograms.

3.2 Single plane fundamentals

Holographic lenses described so far are designed considering each pixel vibrates as a Fabry-Perot resonator, as described in section 2.2.1 (single-plane holograms). These lenses are designed so that at each pixel location, the height of the lens and surrounding medium introduces a phase in the wave that matches the recorded phase at the holographic surface, at a fixed distance (see Figure 3.1 (a)). The wavefront coming from the virtual sources distributed over the target area, P_S, is recorded in a single plane at a fixed distance d. The lens is designed so that at the distance d the equation

$$\arg\left[P_S^*\right] = \arg\left[P_L\right], \tag{3.1}$$

is met, where P_L is the field at the exit plane of the lens. This procedure is equivalent to that explained in section 2.2.1. Assuming one-dimensional propagation in a lens of homogeneous material and perfect impedance matching, the phase at the exit of the lens at height d is given by

$$\arg\left[P_L\right] = -k_L z - k_0(d - z), \tag{3.2}$$

where z is the axial coordinate and $k_0 = \omega/c_0$ and $k_L = \omega/c_L$ are the wavenumbers at frequency ω in the medium of sound speed c_0 and in the lens of sound speed c_L, respectively. From the equation 3.1, calling $\phi_s = \arg\left[P_S^*\right]$, and with the expression for the phase at the end of the lens,

$$\phi_s = -k_L z - k_0(d - z), \tag{3.3}$$

we arrive at a unique expression for the lens height

$$z = \frac{\phi_s}{\omega}\frac{1}{1/c_0 + 1/c_L} + \frac{d}{c_0}\frac{1}{1/c_0 + 1/c_L}, \tag{3.4}$$

which agrees with the expression derived by Maimbourg et al. in their work [61]. In the case of single-plane lenses, for each point of the holographic surface the lens height is unambiguously known. These lenses are ideal in the thin-lens approximation. Nevertheless, for ultrasound wavelengths and the properties of the materials available for 3D-printing, the refraction index is moderate and this approximation is not fulfilled. Also, this approach assumes that each pixel is going to produce a wave that only propagates in the axial direction, which is not true.

3.3 Field matching fundamentals

To take account of this effect, a new strategy is defined. In this case the wavefront coming from the virtual sources, $P_S(z)$, is recorded in a holographic volume, i.e. in successive planes from the transducer location up to a desired distance. The height of the lens in each pixel would be the one whose transmission coefficient phase calculated as in Eq. (2.3), $\arg(P_L(z))$, matches the recorded phase coming from the virtual sources (see Figure 3.1 (b)). To account for multiple phase jumps, the transmission coefficient is expressed as $\arg(P_L(z)) + 2\pi n$, where n is the entire number of 2π changes desired. For some pixels there would exist several points of height z that meet the equality condition. The height of each pixel would be evaluated as the z that fulfils the identity

$$\arg(P_S(z)) = \arg(P_L(z)) + 2\pi n, \tag{3.5}$$

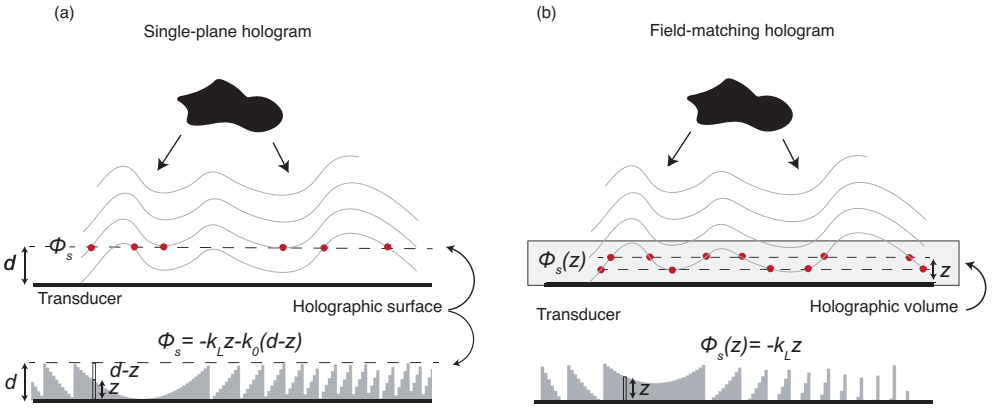

Figure 3.1: (a) Single-plane hologram. The wavefront coming from the virtual sources is recorded in a holographic surface located at a distance d from the transducer and the lens is designed to match that recorded field conjugated phase. (b) Field-matching hologram. The wavefront coming from the virtual sources is recorded in a holographic volume and the lens is designed so that its transmission coefficient phase matches locally the conjugated phase of the wavefront coming from the virtual sources. Red dots denote the regions where the phase of the conjugated field coming from the virtual sources matches the phase of the transmission coefficient.

with n the lower value for which the equality is satisfied. In this case the phase at the exit plane of the lens is not dependent of d, only of the height

$$\arg\left[P_L\right] = -k_L z. \tag{3.6}$$

In the volume of calculation, for each point in the x-y plane we must evaluate the equation

$$\phi_s(z) = -k_L z + 2\pi n. \tag{3.7}$$

In this case, there is no unique solution for the lens height as it depends on the distance z at which the phase of the wave coming from the virtual sources is equal to the phase introduced by the lens (see Figure 3.2 (a)). In fact, for some points in the volume of evaluation it can exist several z that meet the condition in Eq. (3.7), so their profile is not limited by their 2π phase change as the single-plane hologram, but it can grow provided there exists solutions. If the lens is desired to have a maximum length, there will exist some points where the solution (i.e. the point where the phase introduced by the lens equals the phase of the incoming wave) is not found (see Figure 3.2 (b)), even though it could exist for larger heights.

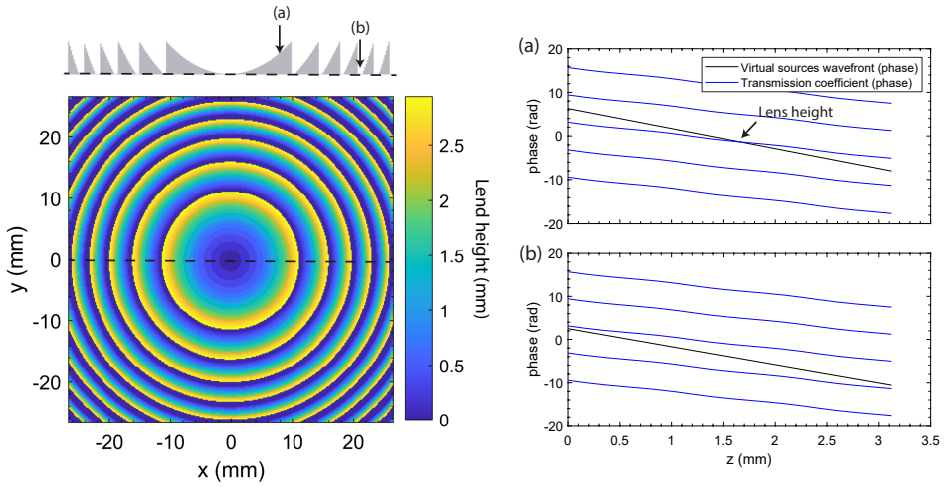

Figure 3.2: Lens height and profile for a field-matching hologram designed to focus at a distance of 50 mm from the transducer and on its axis. (a) Phase-matching principle for the pixel signalized in the lens profile. The point where the phase of the field generated by the virtual sources and the phase of the lens transmission coefficient (considering any possible 2π change) are equal denotes the lens height for that pixel. (b) Phase-matching principle for the pixel signalized in the lens profile, in which no solution for the lens height is found for a predefined maximum lens height.

3.4 Critical angle description

Despite all the commented before, for this hologram topology, there will exist some points for which there will not be any solution to the identity in Eq. (3.7) for any 2π change and any lens height (see Figure 3.3 (b)). These points meet the condition for which the axial component of the wavenumber in the lens material is equal to the one in the medium ($k_{zL} = k_{z0}$). This condition is accomplished when the waves coming from the virtual source come in a specific direction determined by the critical angle.

$$\varphi_c = \sin^{-1}(k_L/k_0). \tag{3.8}$$

To illustrate this, we can codify a plane wave coming to the transducer with an angle matching the critical one. The angular spectrum of this wave is a brilliant point with a radial component of the wavevector given by $k_c = k_0 \sin(\varphi_c)$. In this extreme case, the field matching algorithm is not able to find any solution as the wave is coming with the critical angle direction (see Figure 3.3 (a) and (b)). In this case both the phase of the virtual sources wavefront and the phase of the transmission coefficient of the lens grow parallel one to the other and no solution is possible. If the wave comes in a higher

angle, there always exist a solution providing the lens is allowed to have any length (Figure 3.3 (c)).

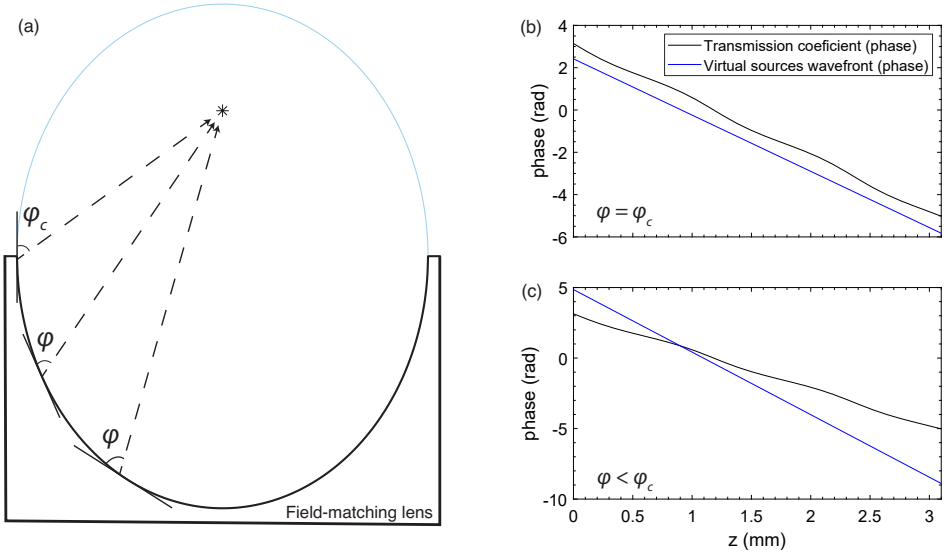

Figure 3.3: (a) Schematic of the situation when the critical angle limitation is fulfilled. It can be seen that any solution of the lens height for the wave direction φ from 0 to φ_c is possible, but angles above this are impossible to be encoded. (b) Field-matching calculation to encode a plane wave into a lens when the plane wave is travelling with the critical angle direction. No solution for the lens height is found as bot phases are parallel. (c) Field-matching calculation to encode a plane wave into a lens when the plane wave is travelling with an angle smaller than the critical. A solution for the lens height is found where the two phases' functions intersect.

This limitation can be surpassed by employing lenses whose material has a lower sound speed than the medium. For materials with this property, there will never exist a critical angle, i.e. there is no solution for Eq. 3.8, and thus a lens height will always be found. Nevertheless, in this case, even the solution is found for any angle, the performance of the lens is limited by the angle at which the total internal reflection is produced

$$\varphi_r = \sin^{-1}(k_0/k_L). \tag{3.9}$$

For the waves coming with this direction or at angles smaller than φ_r, a physical solution is found for the field-matching lens with $c_L < c_0$, but the wave is not going to propagate in that direction. The wave is going to be internally reflected for $\varphi < \varphi_r$ or is going to travel along the interface between both mediums for $\varphi = \varphi_r$.

3.5 Single focus

To understand how each of the methods perform, first we aim to focus on a point in the axis of the transducer and at different distances. The pressure field of a monopole propagating in a homogeneous medium, assuming a Fourier convention of $e^{i\omega t}$, is given by

$$P_S(R,z) = \frac{A_S}{R}\exp\left[-ik_0\sqrt{R^2+(z-F)^2}\right], \tag{3.10}$$

where A_S is the amplitude, R is the radial coordinate, z is the axial coordinate and $k_0 = \omega/c_0$ is the wavenumber at frequency ω in the medium of sound speed c_0.

3.5.1 Single-plane hologram design

In the case of the single-plane hologram, the match between the phase shift introduced by the lens and the phase of the propagating wave is done at the holographic plane, located at a fixed distance d (Eq. (3.3)). Assuming one-dimensional propagation in a lens of homogeneous material and perfect impedance matching, the field at the exit of the lens at height z is given by

$$P_L(R,z) = A_L\exp\left[-ik_Lz - ik_0(d-z)\right], \tag{3.11}$$

where A_L is the amplitude of the plane wave, z is the height of the lens and $k_L = \omega/c_L$ is the wavenumber at frequency ω in the lens of sound speed c_L.

In these holograms, the phase of the complex conjugate of the monopole field at a reference plane $z = d$ is matched with the phase of the plane wave at the reference plane,

$$\arg\left[P_S(R,z)^*\right] - \phi_0 = \arg\left[P_L(R,z)\right], \tag{3.12}$$

using $\phi_0 = k_0F$ as the reference phase at $r = 0$ and $z = 0$, we obtain

$$k_0\left(\sqrt{R^2+(d-F)^2} - F\right) = -k_Lz - k_0(d-z). \tag{3.13}$$

Simplifying

$$z = \frac{\sqrt{R^2+(d-F)^2} - F + d}{1-e}, \tag{3.14}$$

where we define $e = c_0/c_L$. We can write this expression as the implicit equation of a hyperbola

$$\frac{(z-a)^2}{a^2} - \frac{R^2}{b^2} = 1, \tag{3.15}$$

with semi-major and semi-minor axis of values

$$a = \frac{d-F}{e-1}, \quad b = d - F. \tag{3.16}$$

Therefore, lenses made to focus on a single point following the single-plane strategy present hyperbolic profiles, regardless of the value of e.

These expressions are adequate for an unwrapped lens, but if we aim to thin lenses, the phase profile would be wrapped from 0 to 2π. In this case, the profile of the lens can present multiple solutions. The expression of the profile of the n-th hyperbola would be

$$z = \frac{\sqrt{R^2 + (d-F)^2} - (F + 2\pi n/k_0) + d}{1-e}. \tag{3.17}$$

These profiles are shown in Figure 3.4 with light-red colour and the corresponding single-plane hologram in bright-red colour. For both $e < 1$ (Figure 3.4 (a) and (c)) and $e > 1$ (Figure 3.4 (b) and (d)) the profiles of the lenses are hyperbolas with their branches pointing upwards and downwards, respectively.

3.5.2 Field-matching hologram design

In the case of field-matching holograms, in each point of the lens we match the phase information of the wave coming from the virtual source with the phase produced by a specific height of lens material, whose field assuming one-dimensional propagation in a lens of homogeneous material and perfect impedance matching, is

$$P_L(z) = A_L \exp\left[-ik_L z\right]. \tag{3.18}$$

By performing the same match between both phases as in Eq. 3.12, we arrive to

$$z = \frac{\sqrt{R^2 + (z-F)^2}}{e}, \tag{3.19}$$

It can be derived that the previous expression corresponds to a conic section,

$$\frac{(z-a)^2}{a^2} + \frac{R^2}{b^2} = 1, \tag{3.20}$$

with semi-major and semi-minor axis with values

$$a = \frac{F}{1+e},\ b = F\sqrt{\frac{1-e}{1+e}}, \tag{3.21}$$

respectively. Therefore, field-matching holograms designed to focus in a single point present conic profiles with eccentricity value of $e = c_0/c_L$ [85]. Note that when $e < 1$ the profiles are elliptical whereas when $e > 1$ they are hyperbolic due to the change of sign of the parameter b of the conic, so depending on the relation between sound speeds in each material the conic would have a different profile. Note that for $e > 1$ these hyperbolic profiles do not have the same shape as the hyperbolic profiles produced by single-plane holograms, as can be seen in Figures 3.4 (b) and (d). Also, if we were in the case where $e < 1$ and wish to focus at the distance F with only one ellipsoidal profile, this lens would have a limited aperture of $2b = 2F\sqrt{(1-e)/(1+e)}$.

As in the description of single-plane holograms, these expressions are adequate for an unwrapped lens. If we aim to a wrapped lens, the geometrical parameters of the n-th conic can be obtained assuming a phase jump of $2\pi n$, leading to

$$a_n = \frac{F + x_n}{1+e}, \quad b_n = (F + x_n)\sqrt{\frac{1-e}{1+e}}, \tag{3.22}$$

where x_n is defined as

$$x_n = n\frac{\lambda_0}{1-e}, \tag{3.23}$$

and n is the order of the conic profile.

The diffraction codified by this kind of lenses agrees with the same diffraction produced by Fresnel lenses in the approximation of thin layer. Each transmitting ring of the Fresnel lens will appear at a distance from the center equal to [86]

$$r_n = \sqrt{\left(\sqrt{r_0^2 + F^2} + n\lambda_0\right)^2 - F^2}, \tag{3.24}$$

where r_n is the radius of the n-th ring, $n = 0, 1, 2, \ldots$, and r_0 an arbitrary number that defines the radius of the zero-order Fresnel ring. In this case, we can choose r_0 as the value of the radius when n = 1. This radius equals the position of each phase change in the field-matching hologram.

Note that this condition is fulfilled for both when the sound speed in the lens material is higher or lower than the sound speed in the medium. Location of each theoretical Fresnel ring is represented with a black dot in Figures 3.4 (c) and (d).

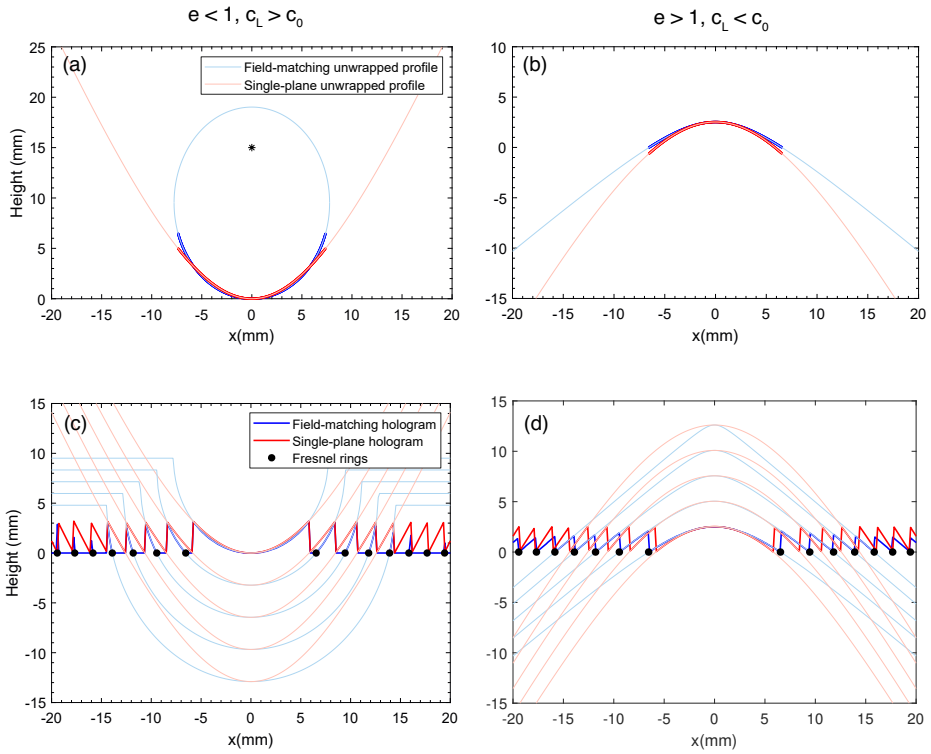

Figure 3.4: Profiles of the field-matching and single-plane holograms designed to focus at 20 mm, with the profiles of the corresponding elliptic and hyperbolic curves that they adjust to. Black dots indicate the radius of the corresponding Fresnel rings. (a) Profiles for a lens material whose sound speed is greater than the surrounding medium (c_L = 2599.3 m/s). (b) Profiles for a lens material whose sound speed is lower than surrounding medium (c_L = 973.6 m/s). The medium was considered as water (c_0 = 1400 m/s)

3.5.3 Critical angle

For the case when $e < 1$, the solution for angles smaller than the critical, given by Eq. 3.8, will be the ellipsoids described above. At the critical angle there won't exist any solution for the Eq. 3.5 for any n value in the corresponding ellipsoid and for angles greater than the critical the method will find solutions in the opposite ellipsoid, i.e. for the ellipsoid whose focus is the contrary and thus not physical to build a lens (see Figure 3.3 (a)). Angles equals or greater than the critical one are specially important when trying to focus near to the transducer, as most waves would come in this direction. It can be seen in Figure 3.4 (c), in the field-matching hologram profiles (blue solid line), that there are some points where it does not physically exist the lens. In the volume where the Eq. 3.5 was evaluated all the waves came in a direction matching the critical angle or greater than this, so no solution could be found. For angles greater than the critical, a solution is found in the opposite side of the ellipsoid, this being a solution with no physical meaning.

As pointed out before, by using lens materials with lower sound speed than the medium, the limitation of the critical angle is surpassed. In this case, the eccentricity is greater than one and field-matching lenses present hyperbolic profiles. Shape of both field-matching and single-plane holograms and their corresponding hyperbolic profiles are presented in Figures 3.4 (b) and (d).

3.5.4 Numerical calculations

Performance of both lenses has been firstly studied with numerical calculations using the Rayleigh-Sommerfeld diffraction integral [87]

$$p(\mathbf{x},\omega) = \frac{i\omega\rho_0}{2\pi}\int_S v_0(\mathbf{x}_0,\omega)\frac{e^{-ikR}}{R}dS,$$

with $R = |\mathbf{x} - \mathbf{x}_0|$ the distance between each source point $\mathbf{x}_0$ and the evaluation point $\mathbf{x}$, and S the radiating source surface which is moving with an amplitude v_0. In these calculations, each lens profile has been designed and each point of the lens is considered a source of pressure waves. The field of a focused transducer whose radius of curvature is set to that of the desired focus location has also been calculated. Note that the focus location of the transducer presents a shift (the focus always appears nearer to the transducer surface) that is given by

$$z_{shift} = F\left(1 - \frac{3G}{2G + \sqrt{G^2 + 72}}\right), \tag{3.25}$$

where $G = k_0 r^2/2F$ is the theoretical gain of the transducer, with k_0 the wavenumber in the surrounding medium and r half the aperture (diameter) of the transducer.

Figure 3.5 summarizes how each of these lenses focuses on the desired location, considering lenses with higher and lower sound speed than water. For lenses with lower sound speed, its material properties has been considered those of silicone material, with sound speed c_L = 974 m/s and density ρ_L = 1063 kg/m^3, as described in the bibliography [88]. The material with higher sound speed has been considered a photopolymer measured in our lab (Clear resin, Formlabs), with sound speed c_L = 2600 m/s and density ρ_L = 1186 kg/m^3. The surrounding medium was considered as water, with sound speed c_0 = 1500 m/s and density ρ_0 = 1000 kg/m^3.

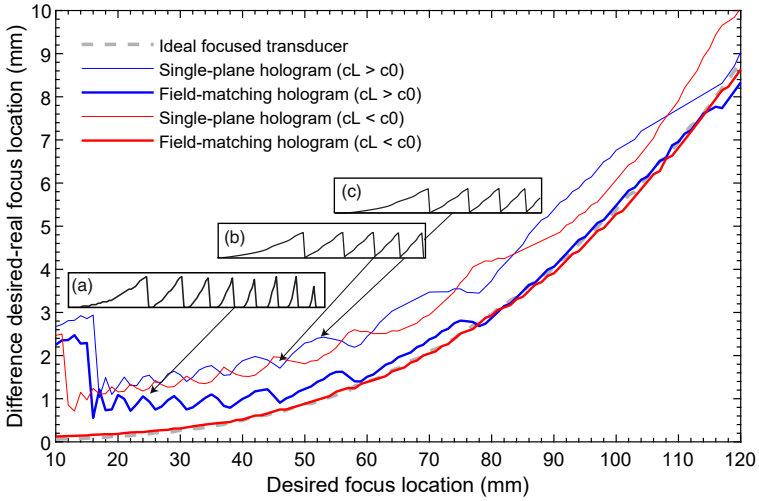

Figure 3.5: Theoretical curves of focus location for single-plane and field-matching holograms considering lens material with higher (blue lines) and lower (red lines) sound speed than water.

Field-matching holograms present their pressure maximum closer to the focus of the equivalent transducer than single-plane holograms. Nevertheless, when the sound speed of the lens material is higher than water, field-matching holograms can present holes, which worsen the quality of the focus as this information is lost, as is represented in inset (a) of Figure 3.5. These holes are the consequence of the critical angle, i.e., at these locations, wavefront direction is given by φ_c.

This is solved when the lens material has lower sound speed than water, and it can be seen that these lenses focus on the exact location of the equivalent transducer. Single-plane holograms for both lens materials present similar behaviour, with oscillations on

the focus location that are due to the diffraction on phase jumps, which represent a 2π phase change in the lens material (see Figure 3.5 insets (b) and (c)). This method when $c_L > c_0$ allows lenses to have pixels whose length is higher than the length needed to have a 2π phase change, which is the maximum length in the single-plane holograms. Note that in the limit where we aim to focus far from the transducer surface all lenses are almost identical on their profile and thus present similar behaviour. Indeed, in this limit wavefront curvature is low and the thin lens approximation is fulfilled.

To better model the real behaviour of these lenses, the same study has been performed with axisymmetric finite-difference time domain (FDTD) simulations. We have used FDTD in this case because axisymmetric boundary conditions can be more easily implemented than in pseudo-spectral methods, and since the axisymmetric calculations are 2D numerical grids, the computations can run efficiently on fine grids. For these simulations, absorption of the lens material has been set to 2.95 dB/cmMHz for both materials. Also, to better model the behaviour of a plane transducer to which the lens would be attached, where the ceramic is clamped to the housing at the edge, it has been considered to have a sigmoid pressure profile, with almost no emission at the edges. In the points where the field-matching lenses do not have a solution, we have considered that there was no radiating field. Results of the maximum pressure location are summarized in Figure 3.6 (a). In this study we can see that field-matching holograms (bold lines) focus more similar to the ideal focused transducer than single-plane holograms (thin lines) do, for both lens materials. Field-matching holograms with higher sound speed than the surrounding medium focus better than the corresponding unwrapped elliptic lens (black line) at distances closer to the transducer than its aperture, having a similar performance when focusing at larger distances. This is due to the fact that at distances less than the aperture of the transducer, the elliptic lens has a semi-minor axis smaller than the aperture, so it does not cover all the transducer. To model these cases, transducers with apertures corresponding to the semi-minor axis of each elliptic lens have been considered.

We can also study the pressure gain at the maximum of these lenses. Simulation results are summarized in Figure 3.6 (b). As shown in this image, for lenses with higher sound speed than water, field-matching holograms focus with better gain at closer distances to the transducer, while the gain gets equal to the single-plane holograms at further distances. For focusing distances below 30 mm field-matching lenses present an average 25% better gain than single-plane holograms. In the case of a lens material with lower sound speed than water, gain of both lenses is very similar at longer distances while at closer distances single-plane holograms get in average 18% higher gain. This is due to the existence of the total internal reflection for this contrast of mediums ($c_L < c_0$). If we calculate the critical angle for internal reflection in this case, we have that φ_r = 40.5°. The transducer has a radius of aperture of 25 mm, so, by trigonometry, when trying to

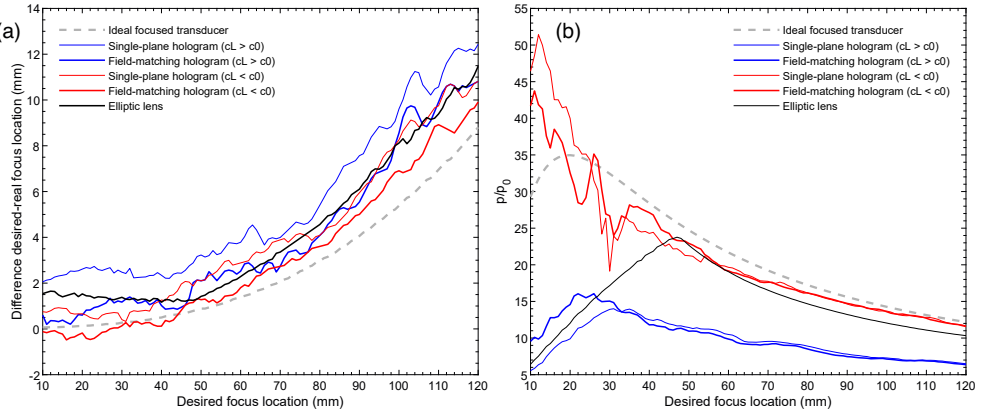

Figure 3.6: Simulation curves of (a) focus location and (b) focus gain for single-plane and field-matching holograms considering lens material with higher (blue lines) and lower (red lines) sound speed than water. Comparison with unwrapped elliptic lens (black line) and the ideal focused transducer (dashed line)

focus at distances less than 16 mm these lenses will lose performance, as can be seen in both red lines in Figure 3.6 (b).

What is most considerable in this study is the difference in gain due to the lens material. This higher gain at closer distances for the lens material with lower sound speed is due to the geometry of the lens, where all the lens material is contributing to bring the acoustic energy into the focus, and also to the better impedance matching of this material, whose density and sound speed are closer to water. Nevertheless, for the higher sound speed material, at closer distances it appears a lot of spectral components whose wavenumber is equal or greater than the critical wavenumber. This limitation applies for both field-matching and single-plane holograms. That is the reason why at distances very close to the transducer both lenses struggle to get the focus in place with enough energy. Watching at the lenses profiles (Figure 3.4 (c)) this lack of energy at the focus can also be produced because saw teeth of the lens will impede waves coming for the neighbouring saw tooth to arrive to the focus. For the unwrapped elliptic lens, its gain is similar to both single-plane and field-matching holograms at distances higher than the transducer aperture, when the full ellipsoid is retrieved, while its gain decreases at closer distances due to the decrease in the transducer aperture.

3.6 Holograms

3.6.1 Bessel beams

A tilted conical beam with topological charge has been designed for both field-matching and single-plane holograms with the following pressure distribution:

$$P_s(x_0, y_0, z_0, \theta) = \exp\left(-ik_0\left(\sin(\alpha)\sqrt{x_0^2 + y_0^2} + \sin(\beta)\, x_0\right)\right)\exp(-iM\theta)$$

where α is the Bessel beam conical angle, β is the tilt angle in the x direction, M is the topological charge of the Bessel beam and θ is the polar angle. For this beam, α has been set to 30°, β to 10° and the topological charge to 1. In this way, we try to design a tilted vortex beam. Note this beam has only pure phase information and thus no amplitude data is lost when designing the lens. Ideally, a conical wavefront should generate a Bessel beam of non-constant amplitude [89]. These fields have been calculated using a pseudo-spectral time-domain method, implemented in the software *k-Wave* [76], and retaining all the temporal information at the desired planes. To get the phase and amplitude information, a fast Fourier transform has been performed to the temporal signals and the information at the centre frequency of the transducer has been retained.

The ideal Bessel beam and its phase information at an axial plane at the middle of the beam (30 mm from the transducer surface) are shown in Figures 3.7 (a) and (b). For this beam, all its normalized angular spectrum lies within a circle of radius 0.5, as can be seen in Figure 3.7 (g). Also, all the angular information lies within the critical angle, represented by a white dashed circle in Figure 3.7.

The pressure field of the field-matching hologram and its phase information at the same axial plane are summarized in Figures 3.7 (c) and (d). Examining its angular information (Figure 3.7 (h)), it can be seen that there is a strong contribution of a plane wave coming from the transducer in the pure z direction, as depicted by the bright spot in the centre of the angular spectrum, but also the main information of the Bessel beam is retrieved, even though with less amplitude than in the ideal case. For the single-plane hologram, whose amplitude and phase information are shown in Figures 3.7 (e) and (f), also the Bessel vortex beam is retrieved. Looking at its angular spectrum information (Figure 3.7 (i)), again the contribution of the plane wave coming from the transducer in the z direction is very important, but it is more noticeable that the main information of the Bessel beam ($n = 1$ diffraction order) has lower amplitude than the corresponding $n = -1$ order diffraction grating replica.

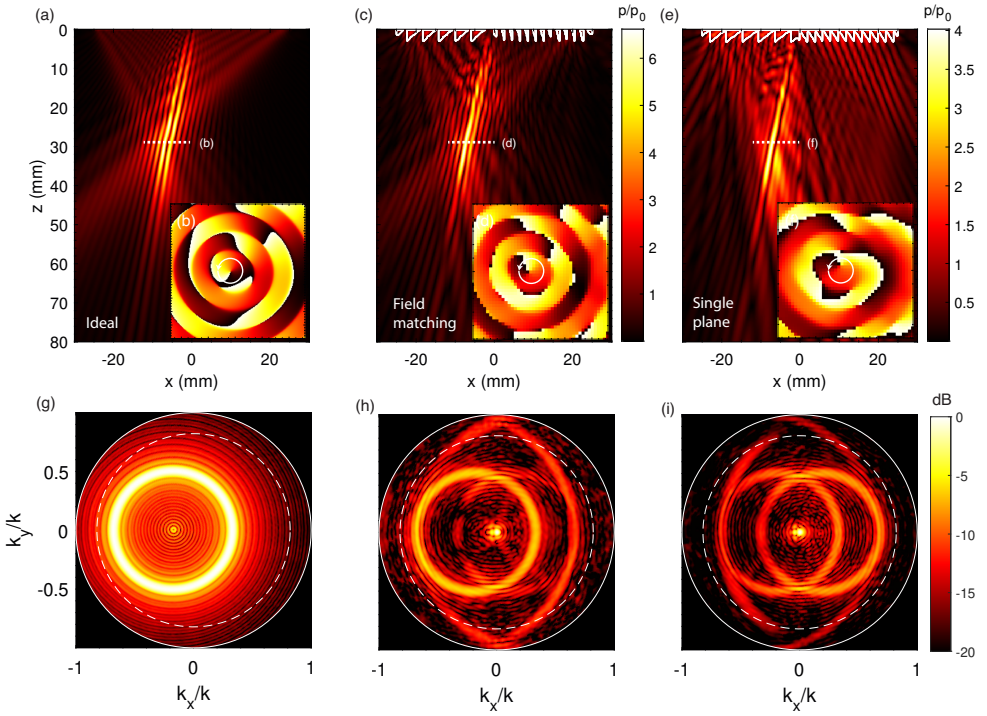

Figure 3.7: Bessel beam with α = 30°, β = 10° and M = 1, with $c_L > c_0$ (a) Ideal beam pressure field. (b) Phase of the ideal beam at 30 mm from the transducer at the beam region. (c) Simulated field-matching hologram pressure field. (d) Phase generated by the field-matching hologram at 30 mm from the transducer at the beam region. (e) Simulated single-plane hologram pressure field. (f) Phase generated by the single-plane hologram at 30 mm from the transducer at the beam region. (g) Angular spectrum of the ideal beam. (h) Angular spectrum of the field generated by the field-matching hologram. (i) Angular spectrum of the field generated by the single-plane hologram. White-dashed circle represents the critical wavenumber and white solid circle delimits the real wavenumbers.

A second Bessel beam has been designed for the same β value but for α = 40°. In this case, part of the angular information of the beam lies in the critical angle. In the ideal case (Figures 3.8 (a),(b)), a similar Bessel vortex beam is retrieved, shorter than in the previous case as expected by the higher value of the parameter α. The ring in the angular spectrum of the beam (Figure 3.8 (g)) is fully retrieved in the ideal case. The influence of the critical angle in the lens performance is clearly seen in Figures 3.8 (h) and (i), where the angular components belonging to the critical angle are missing. These directions cannot be codified by the field-matching hologram, as we expected, but neither can be codified by the single-plane hologram even though the lens does not present any

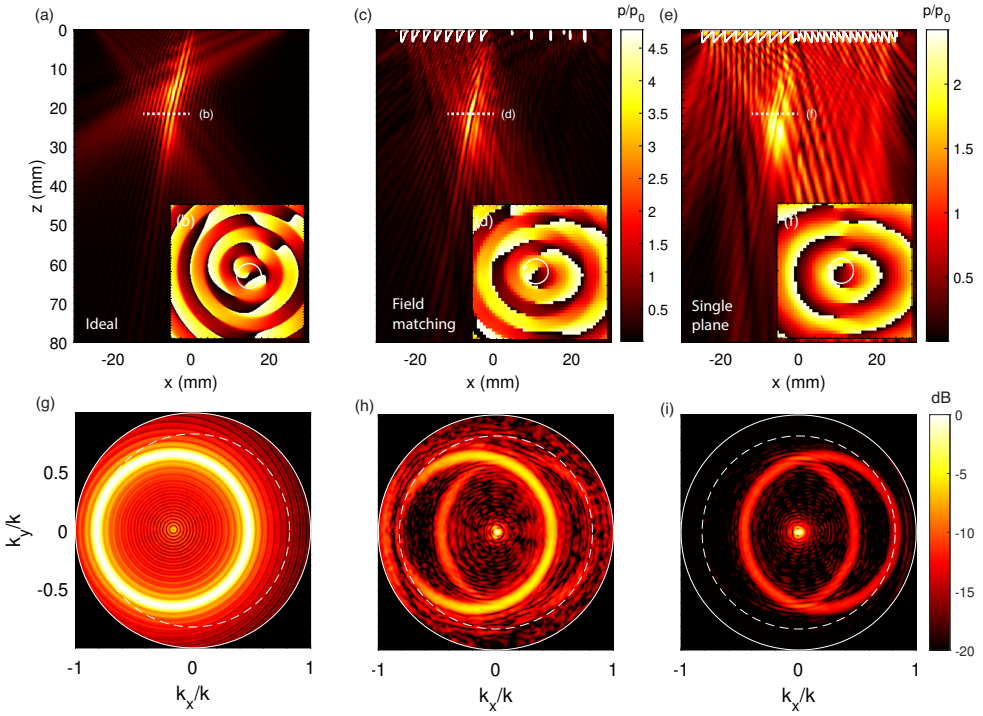

Figure 3.8: Bessel beam with α = 40°, β = 10° and M = 1, with $c_L > c_0$ (a) Ideal beam pressure field. (b) Phase of the ideal beam at 30 mm from the transducer at the beam region. (c) Simulated field-matching hologram pressure field. (d) Phase generated by the field-matching hologram at 30 mm from the transducer at the beam region. (e) Simulated single-plane hologram pressure field. (f) Phase generated by the single-plane hologram at 30 mm from the transducer at the beam region. (g) Angular spectrum of the ideal beam. (h) Angular spectrum of the field generated by the field-matching hologram. (i) Angular spectrum of the field generated by the single-plane hologram. White-dashed circle represents the critical wavenumber and white solid circle delimits the real wavenumbers.

hole. This lack of information is reflected in the generated beam. For the field matching lens, when the field is not coming out of the transducer in the parts where no solution is found as if air was trapped at these points and the ultrasound wave is not allowed to propagate, the remaining phase information is focusing where the beam was designed to be (Figure 3.8 (c)) and even the vortex is created in the desired area (Figure 3.8 (d)). For the single-plane hologram, all the lens is designed and is contributing to the formation of the acoustic field. Nevertheless, the created field is noisy, with an important contribution of waves coming in the opposite direction of the designed Bessel beam, as depicted by

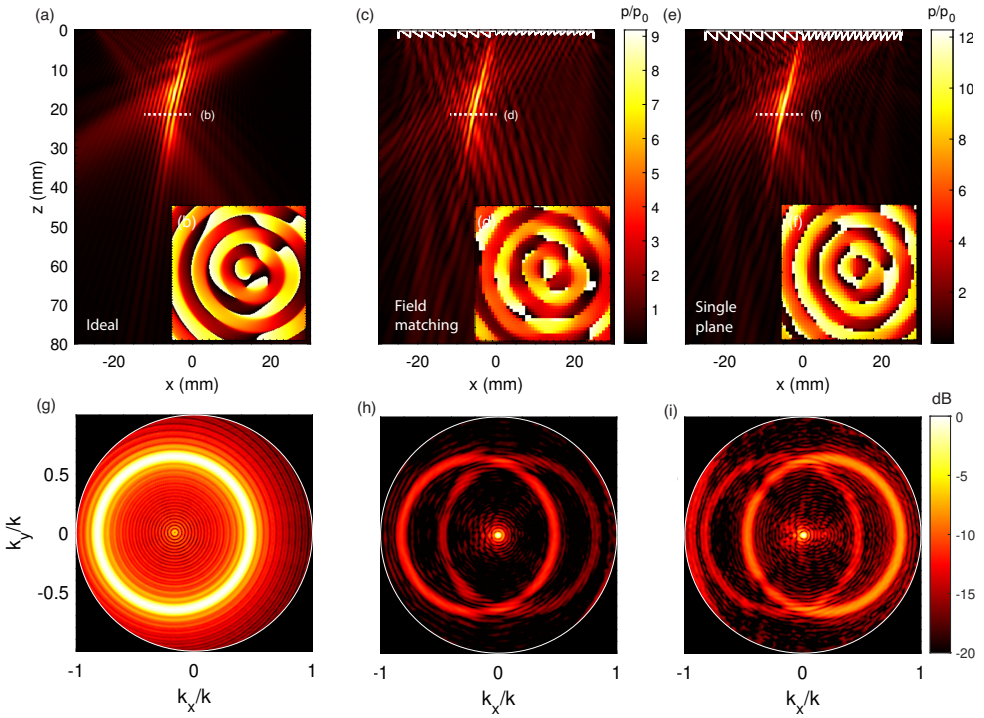

Figure 3.9: Bessel beam with $\alpha = 40°$, $\beta = 10°$ and M = 1, with $c_L < c_0$. (a) Ideal beam pressure field. (b) Phase of the ideal beam at 30 mm from the transducer at the beam region. (c) Simulated field-matching hologram pressure field. (d) Phase generated by the field-matching hologram at 30 mm from the transducer at the beam region. (e) Simulated single-plane hologram pressure field. (f) Phase generated by the single-plane hologram at 30 mm from the transducer at the beam region. (g) Angular spectrum of the ideal beam. (h) Angular spectrum of the field generated by the field-matching hologram. (i) Angular spectrum of the field generated by the single-plane hologram. White-dashed circle represents the critical wavenumber and white solid circle delimits the real wavenumbers.

its angular information (Figure 3.8 (e)). Also, this lens is not able to create the vortex with the same homogeneity as the field matching lens.

The problem of the critical angle is solved by using a lens material with lower sound speed than water. This same Bessel beam is codified by a field-matching and a single-plane holograms with this characteristic lower sound speed. Results are summarized in Figure 3.9. Note that in this case the full angular spectrum information is retrieved, as no critical angle exists now, and both lenses present a similar performance.

3.6.2 Transversal holograms

To better represent the performance of field matching lenses compared with single-plane holograms for both cases when there exists a critical angle and when there it does not, we have created transversal holograms representing all the numbers from one to nine extracted from the MNIST dataset [90]. We have studied their performance when focusing at different distances ranging from 10 to 70 mm in 5-mm steps. The Structural Similarity Index Method (SSIM) [91] has been employed to compare each generated hologram with the ideal field. In Figure 3.12 is summarized the mean value of the SSIM index among the ten different digits for each focusing distance. It can be seen that when focusing near to the transducer the field-matching lens has a significant better performance when the lens has a higher sound speed than the surrounding medium (Figure 3.12 (a)), presenting the same behaviour when focusing at distances greater than half the aperture of the transducer (25 mm). When the lens has a lower speed of sound, both lenses are able to create similar holograms, with the field-matching lens performing slightly better at closer distances (Figure 3.12 (b)). This behaviour is consistent with previous examples, seeing that the limiting factor for both field-matching and single-plane holograms is the existence of the critical angle when they are made of a material with higher sound speed than the surrounding medium, which are the most common materials in 3D printing.

Figure 3.10 represents the created MNIST numbers holograms at a distance of 15 mm from the transducer when the lens material has higher sound speed than the surrounding medium, whilst Figure 3.11 represent the same holograms at the same distance but for a lens material with lower sound speed.

3.7 Chapter conclusions

In this Chapter we have discussed a new method for designing holographic lenses, based on creating a match between the holographic field that we want to reconstruct and the transmission coefficient of the lens material. When focusing in a point in the centre of the transducer, these lenses present ellipsoidal profiles. It was shown that when the lens presents a higher sound speed than the surrounding medium, which is the case for most 3D-printing materials, there exist some wave directions that the lens is not able to codify. The condition met by these waves is the equality of the axial component of the wavenumber in the lens material and in the surrounding medium. Also, waves whose axial component of the wavevector is higher than that cannot be correctly codified. This is clearly seen for field-matching holograms, where there is no solution for those wave directions. To avoid this inconvenience, we can use materials with lower sound speed than water. For these materials the previous condition is never met and the lens capture all the information correctly and can be designed. Nevertheless, in this case the wave

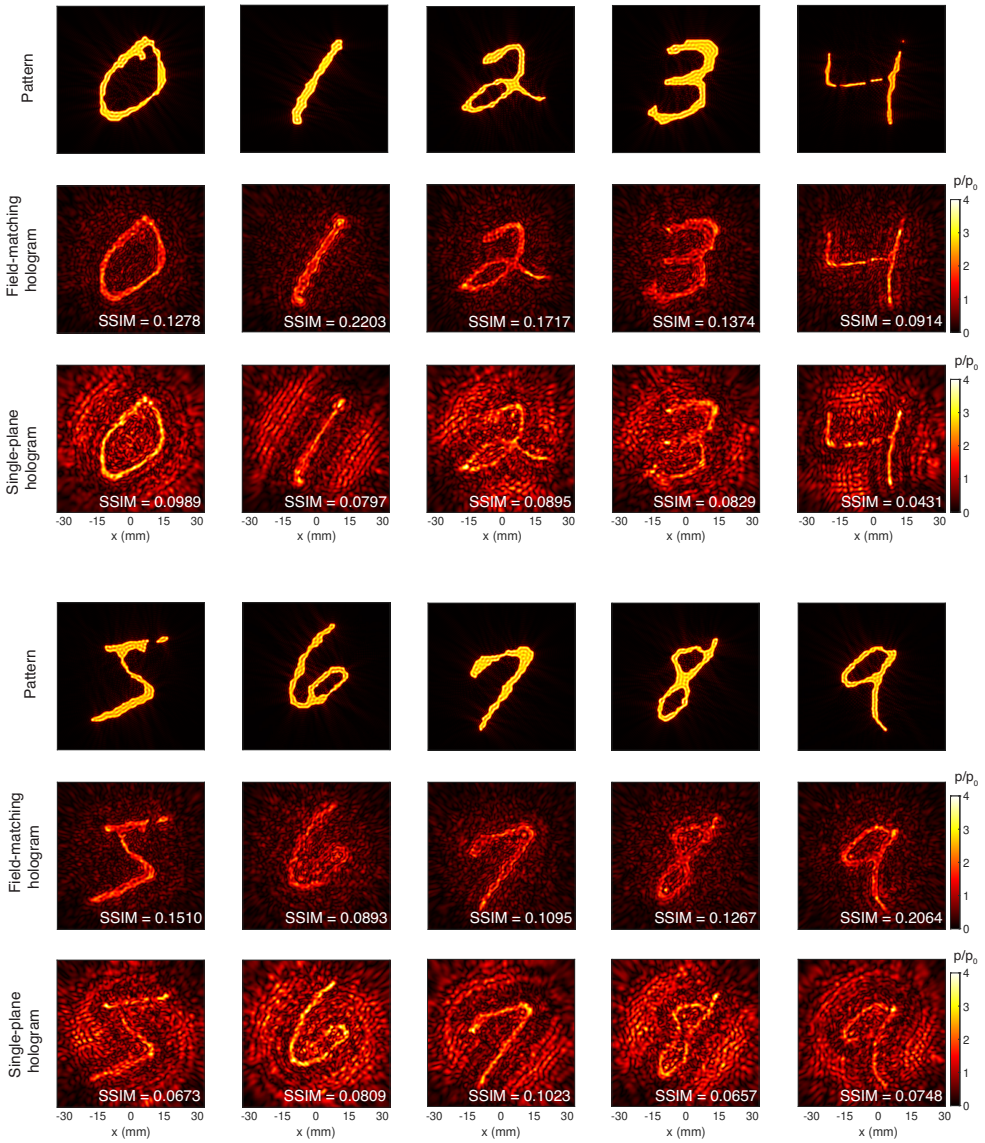

Figure 3.10: MNIST images - acoustic images obtained with both field-matching and single-plane holograms when $c_L > c_0$ focusing at 15 mm from the transducer's surface.

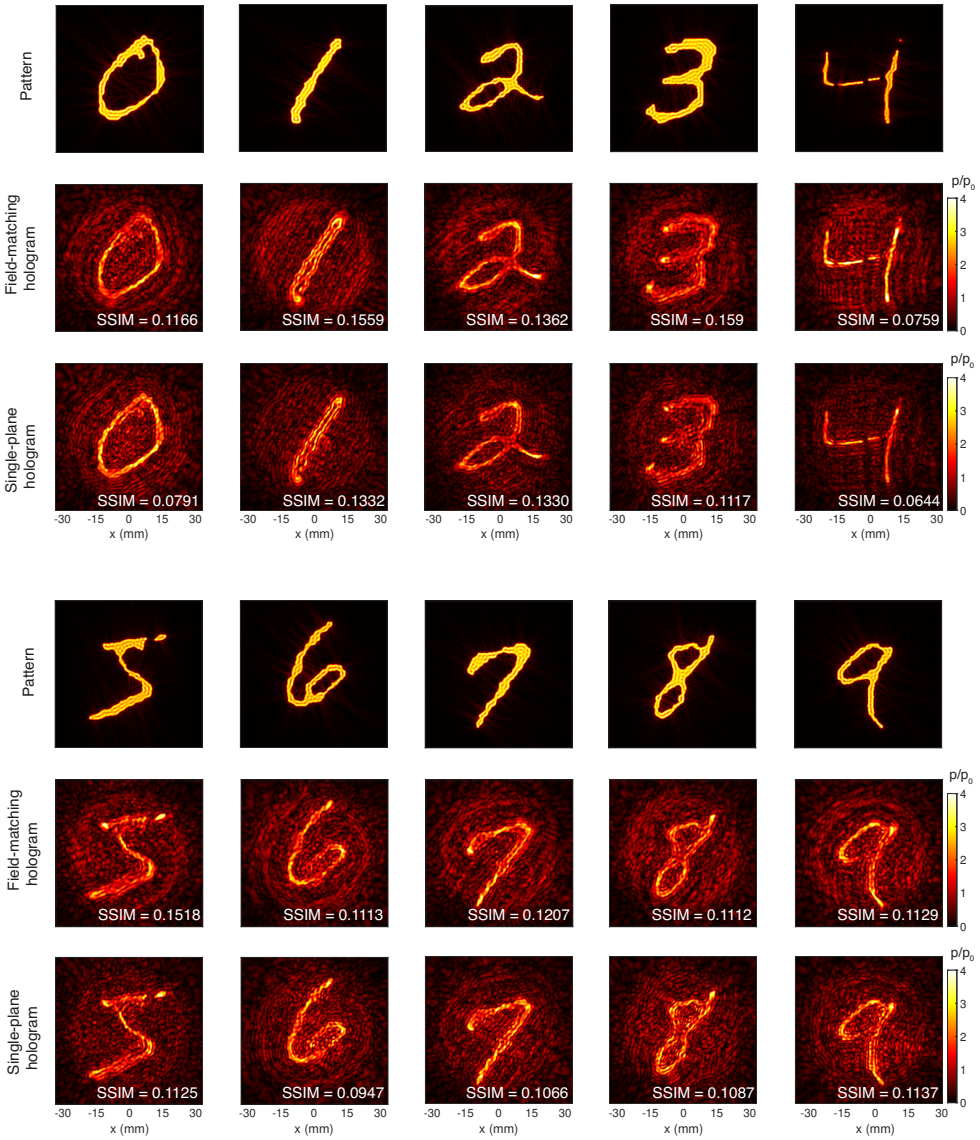

Figure 3.11: MNIST images - acoustic images obtained with both field-matching and single-plane holograms when $c_L < c_0$ (no critical angle) focusing at 15 mm from the transducer's surface.

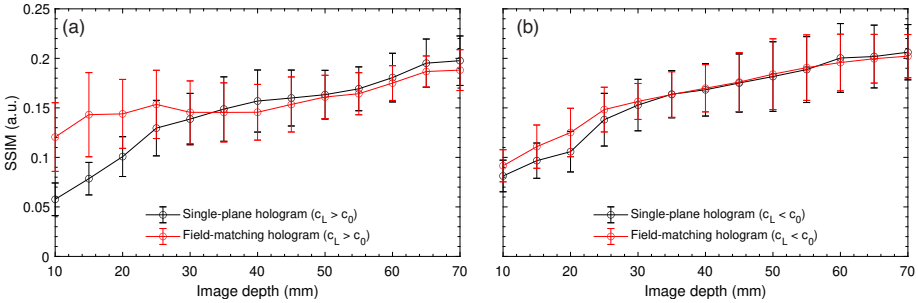

Figure 3.12: Structural Similarity Index for single-plane and field-matching holograms when (a) the sound speed of the lens material is higher than water ($c_L > c_0$) and (b) is lower than water ($c_L < c_0$).

transmitting from the lens to the medium can suffer from internal reflection, which is not captured by the method and affects the lens performance.

When creating complex holograms, for materials with higher sound speed than water, field-matching holograms perform better than single-plane holograms provided that the field is blocked, i.e. there is no transmission of the ultrasound, at the parts of the lens where there exists no solution. For materials with lower sound speed than the surrounding medium, both lenses present similar performance. For both materials, when aiming to focus in a point in the axis of the transducer at a fixed distance, the field-matching hologram is able to focus nearer to the desired location as it reproduces better the wave information. This is more critical when using materials with higher sound speed than water.

Further investigation needs to be done in these lenses' topology, as they have only been proposed and studied in a numerical way along this Chapter. Experimental measures with these 3D printed lenses are needed to confirm that this new technique can overcome the drawbacks presented by the current single-plane lenses. It's important to point out that along next Chapters of the thesis, single-plane lenses are going to be used.

Chapter 4

Holograms to produce thermal patterns

Holograms can shape wavefronts to produce arbitrary acoustic images. In this Chapter, we experimentally demonstrate how acoustic holograms can produce controlled thermal patterns in absorbing media at ultrasonic frequencies. Holographic MRI-compatible ultrasound lenses were designed using time-reversal methods and fabricated using 3D printing. Several thermal holographic patterns were measured using MRI thermometry and a thermographic camera in gelatin-milk phantoms and in an ex-vivo liver tissue. The results show that acoustic holograms enable spatially-controlled heating in arbitrary regions. Rising the temperature using low-cost and MRI-compatible holographic transducers might be of great interest for many biomedical applications, such as ultrasound hyperthermia, where the control of specific thermal patterns is needed. This Chapter is part of a collaboration with Jonathan Vappou at the Strasbourg University.

4.1 Introduction

Optical holograms can modulate light wavefronts to generate visible images [92]. In the same way, acoustic images can also be synthesized by holograms, shaping the areas where mechanical waves present a high amplitude, and areas where the matter is at rest. Holographic acoustic fields can be synthesized by ultrasound phased-array systems [93,

94], but the small number of active radiating elements, typically up to one thousand, limits its performance. In addition, the cost associated to these systems in terms of driving electronics and independent impedance matching makes them unaffordable for many applications. In recent years, acoustic holograms have been exhaustively studied [51], mainly triggered by the emergence of 3D printing technologies. Artificially-structured materials, such as complex phase plates [51, 95] (also known as kinoforms [53]), gratings [96, 73], or metamaterials [97, 98, 99, 100], have enabled accurate wavefront engineering for many applications such as particle trapping and manipulation [101, 102], scattering control and vortex generation [103], fast 3D-printing [104], volumetric displays [105] or 3D imaging [106].

Compared to light, acoustic waves can penetrate much deeper into biological media. Therefore, acoustic holograms are bursting onto current biomedical applications due to their capability to shape and focus ultrasound fields inside living tissues. Acoustic holograms can encode complex wavefronts compensating the phase aberrations produced by stiff layers of tissues, such as skull bones in transcranial propagation, enabling the creation of single focal spots [61], arbitrary therapeutic patterns in the brain [63, 107], or even vortex beams [64]. Other recent uses of acoustic holograms in biomedical applications include cell patterning [58], the control of cavitation patterns, that has been demonstrated in homogeneous tissue phantoms with embedded microbubbles [59] and in-vivo inside the head of small animals [65], or burst-wave lithotripsy [60].

Acoustic waves transport energy, and when propagating into biological media a fraction is irreversibly transformed into heat by viscoelastic and relaxation processes. In ultrasound imaging applications the temperature rise is negligible because the total energy of the wave is moderate [108]. However, at high ultrasound intensities heat deposition can be elevated and fast enough to create cell necrosis and tissue ablation [109]. Combined with sharp focusing, high intensity focused ultrasound is currently used in clinics for therapeutical purposes [110]. Recently, attention has been paid to intermediate regimes, when ultrasound is used to create a local and mild hyperthermia, which is defined as a rise in tissue temperature between 39° C and 45° C, typically with long exposure times [111, 112, 113]. HIFU-mediated hyperthermia is emerging as a highly promising therapeutic approach that has been shown to activate the immune system, and/or enhance drug delivery, in particular for chemotherapeutic drug administration [8, 114]. Usually in mild hyperthermia applications a wide region of tissue is covered sequentially by multiple focal spots, by using the electronic steering of the beam of a phased-array transducer, which is in fact an active research topic [50, 115, 116]. During treatment, the temperature inside the tissue is monitored using magnetic resonance imaging (MRI) thermometry, resulting in long treatment duration and expensive MRI-compatible devices.

In this Chapter, we demonstrate how acoustic holograms can create arbitrary thermal patterns in ex-vivo biological media and tissue-mimicking phantoms using a low-cost MRI compatible transducer, resulting in a portable, patient-specific and personalized therapeutical device. We illustrate the concept using two target holographic patterns. First, an arbitrary thermal image is produced (in this case we have chosen the shape of the number "2"), and, second, we enlarge the thermal pattern of an ultrasound device currently used for hyperthermia applications using a holographic lens. Furthermore, we study how non-linearities in the acoustic field can affect the produced thermal pattern at hyperthermia intensity powers.

4.2 Materials and methods

4.2.1 Lens design

Two transducers are used: for the first configuration we use a flat piezoelectric disc of aperture $2a = 50$ mm and central frequency $f_0 = 1.1$ MHz, mounted on a 3D-printed MRI-compatible custom-design housing, shown in Figure 4.4 (a). For the second configuration, we use a commercial spherically-focused ultrasound transducer of radius of curvature $F = 100$ mm, elliptical aperture of mayor axis $2a = 125$ mm and $b = 85$ mm, and central frequency of $f_0 = 1$ MHz (Imasonic, Voray sur l'Ognon, France), shown in Figure 4.7 (a).

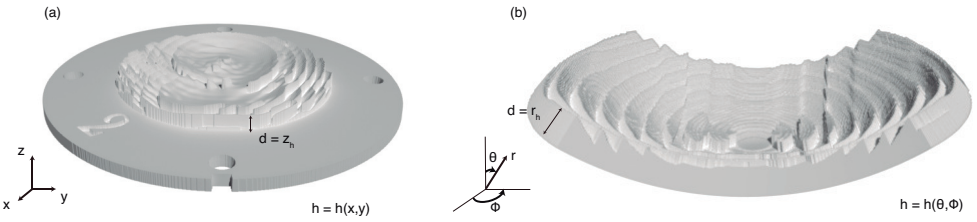

Figure 4.1: (a) Schematic image of the lens used with the flat transducer, corresponding to the '2'-shaped pressure profile. (b) Schematic image of the lens used with the focused transducer, corresponding to the ellipsoid-shaped pressure profile.

Acoustic holograms were designed using time reversal methods, following the procedure described by [63] using k-space numerical simulations implemented in the software *k-Wave* in Matlab [117]. First, 2993 virtual sources (distance between 2 sources = 0.22 mm) are distributed in the area corresponding to the shape of the target image,

e.g., the number "2", within a plane parallel to the transducer surface, at 20 mm distance. For the second configuration, we located five virtual sources at a depth of 65 mm from the transducer surface with the aim of obtaining a region of hyperthermia defined as an ellipse with 15-mm width and 10-mm height dimensions. Each source was set to emit a 100-cycles sinusoidal tone burst at the transducer working frequency, with the same amplitude. An additional relative phase term $\exp(ikz)$ was introduced for each virtual source to set the direction of the outgoing wavefront during backward simulations. The simulated medium was homogeneous with the acoustic and thermal properties matching those of a liver tissue. Density and sound speed values were set to $\rho_t = 1079$ kg/m^3 and $c_t = 1586$ m/s, respectively [118, 119]. Acoustic attenuation follows a frequency power-law given by $\alpha_t = \alpha_0 f^\gamma$, where f is the frequency, and for liver tissue $\gamma = 1.1$ and α_0 was set to obtain an attenuation of 0.59 dB/(cm·MHz$^\gamma$) [120]. The wavefront generated by the interference of the sound waves coming from each virtual source is captured in a surface parallel to the transducer surface, the holographic surface. This surface corresponds to a plane for the first configuration and to a curved surface for the second configuration regarding each transducer's geometry. For the flat circular hologram, the surface is divided into square pixels of side 0.25 mm, whereas for the spherical hologram, a uniform cartesian grid is designed and projected on the curved surface, as described in Chapter 2. In both cases, phase information is retained in this holographic surface and we use this data to design the lens height profile, assuming that each pixel vibrates longitudinally as an elastic Fabry-Perot resonator (Eq. 2.3). By tuning the height of each column the transmission coefficient can be spatially-modulated. In this way, the transmitted field was set to mimic a phased-conjugated version of the recorded wavefront [63]. The physical design of both flat and curved lenses was performed as decribed in Chapter 2.

We fix a minimal lens thickness of 2.5 mm, which corresponds to $7\lambda/4$ in liver medium, for mechanical robustness when 3D-printing. Maximum lens height is 5.45 mm, so the resulting lens was approximately a flat disc with a roughness of about 3 mm, see Figure 4.4 (a). Lenses were 3D printed using stereolithographic methods on a photosensitive resin (Clear resin, Formlabs, USA), printed on a 25 μm resolution printer (Form 2, Formlabs, USA). The density and sound-speed values of the lens were experimentally obtained as $\rho_L = 1171$ kg/m^3, $c_L = 2580$ m/s, respectively. Attenuation was set to 2.72 dB/(cm·MHz$^\gamma$), according to previously reported values for similar photopolymers [51]. A schematic of both lenses can be seen in Figure 4.1 (a,b)

4.2.2 Non-linearities

Acoustic attenuation in soft-tissue media was considered to follow a power-law frequency dependence as $\alpha_t = \alpha_0 \cdot f^\gamma$ where f is the ultrasound frequency, α_0 is the attenuation constant and $\gamma = 1.1$ is the power law exponent. As α_0 is frequency dependent, its value was 0.59 dB/(cm·MHz$^\gamma$), 1.32 dB/(cm·MHz$^\gamma$) and 1.98 dB/(cm·MHz$^\gamma$), for the first, second and third harmonic, respectively [119]. The parameter of nonlinearity in the medium was set to $B/A = 7.7$, according to existing literature [121]. Regarding the simulated domain size, the propagation path length was set to 50 mm (37 wavelengths at the central frequency) and the domain width to 110 mm (82 wavelengths). A discretization of 6 points per wavelength for the third harmonic (f = 3.3 MHz) was used, and the Courant-Friedrichs-Lewy number was set to 0.2. Different acoustic pressures p_0 (0.35 MPa, 1.55 MPa and 4.5 MPa) at the transducer surface were modelled to study the power-dependence of the harmonic generation. Gol'dberg number was obtained to determine the propagation regime in each case, calculated as follows [122]:

$$\Gamma = \frac{\beta \omega p_0}{\alpha_t \rho_t c_t^3}, \tag{4.1}$$

Where β is the coefficient of nonlinearity ($\beta = 1 + B/2A$) and $\omega = 2\pi f_0$ is the angular frequency. Once the acoustic field is calculated, for both linear and nonlinear propagation, we obtained the resulting thermal pattern in liver tissue. Heat distribution was calculated with the Penne's bio-heat equation [123], given by

$$\rho_t C_t \frac{\partial T}{\partial t} = \nabla(\kappa \nabla T) - W_b C_b \left(T - T_b\right) + Q, \tag{4.2}$$

where ρ_t, T, κ and C_t are the tissue density, temperature, thermal conductivity and specific heat capacity, W_b, T_b and C_b the blood perfusion rate, temperature and specific heat capacity, and Q the volume rate of heat deposition, defined as

$$Q = \sum_i 2\alpha_i I_i, \tag{4.3}$$

where the subindex $i = 1, 2, 3$ represents the harmonic number, α_i is the medium absorption coefficient at each harmonic and the intensity I_i is given by

$$I_i = \frac{p_i^2}{2\rho_t c_t}, \tag{4.4}$$

where p_i is the peak acoustic pressure at stationary state for each harmonic. In the case of linear propagation, peak pressure is calculated as the maximum pressure in steady state so no harmonic contributions appear. Blood perfusion was set to zero as experiments

were done with ex-vivo tissues. Specific heat capacity and thermal conductivity were set to $C_t = 3540$ J/(kg·K) and $k = 0.52$ W/(m·K), according to values in the literature [118].

4.2.3 Acoustic validation

The resulting pressure fields were validated by simulations using a pseudo-spectral time-domain method [76], and, for the "2"-shaped hologram, also by experimental measurements of the acoustic field, the latter performed in a degassed water tank at 23° C maintained by a water conditioning unit (WCU-Series, Sonic Concepts, USA). The flat holographic lens was directly coupled to the custom-made MRI-compatible piezoelectric transducer as shown in Figure 4.4 (a). Acoustic field measurements were performed using a piezoelectric hydrophone (-225.5 dB re 1 V/μPa at 1 MHz, Model Y-104, Sonic Concepts, USA), calibrated from 40 kHz to 2 MHz, attached to a 3D positioning system (5 μm precision, PI Micos GmbH, Germany) in a degassed water tank at 23° C maintained by a water conditioning unit (WCU-Series, Sonic Concepts, USA). The transducer was driven by a 20-cycles sinusoidal pulse burst at a frequency of $f = 1.1$ MHz using a signal generator (14 bits, 100 MS/s, model PXI5412, National Instruments, USA) and amplified by a linear RF amplifier (ENI 1040L, 400 W, 55 dB, ENI, Rochester, NY, USA). The acoustic signals were recorded scanning a plane at $z = 20$ mm, from -22 mm $< x <$ 22 mm and -22 mm $< y <$ 22 mm, using steps of 1 mm. Signals were averaged 20 times at each location to reduce random noise. An schematic of the experimental setup for acoustic validation is shown if Figure 4.2 (a)

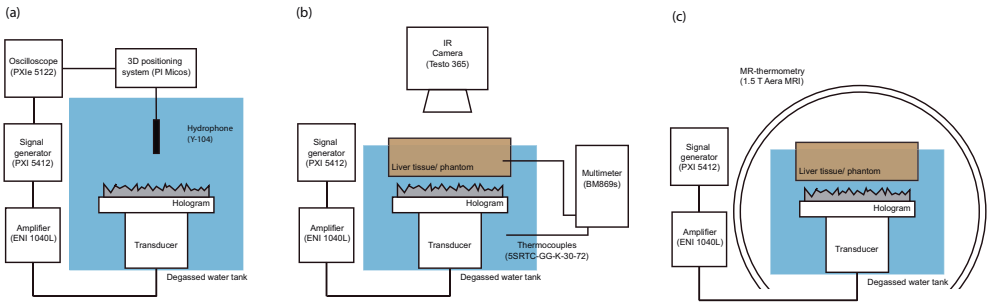

Figure 4.2: (a) Schematic diagram of the experimental setup for acoustic measurements. (b) Schematic diagram of the experimental setup for thermal measurements with infra-red camera. (c) Schematic diagram of the experimental setup for thermal measurements with MR-thermometry.

4.2.4 Thermal validation

Thermal simulation and experiments were carried out by driving the source with a continuous sinusoidal signal at its centre frequency (f_0 = 1.1 MHz). Experimental validation was performed using two systems. On the one hand, temperature was measured with an infrared thermal camera (Testo 365, Testo, Germany) at the surface of a 20-mm slice of degassed cow liver tissue, taking images at a rate of 15 frames per minute. Temperature at the water tank and at the lateral boundary of the tissue was monitored with two thermocouples (5SRTC-GG-K-30-72, Omega Engineering, Norwalk, Connecticut) connected to a multimeter (MS869s, Brymen, Taiwan) (see Figure 4.2 (b) and Figure 4.4 (b)). On the other hand, temperature was measured by proton-resonance frequency-shift (PRFS) MR-thermometry using a 1.5 T Aera MRI (Siemens, Erlangen, Germany). A single-slice using a 2D gradient-echo (GRE) sequence was used for MR-PRFS thermometry, obtaining one thermal image every 1.2 seconds [1] (see Figure 4.2 (c)).

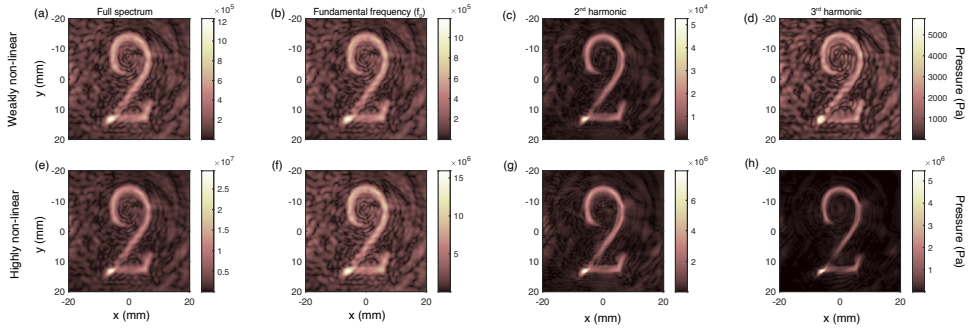

Figure 4.3: (a-d) Peak pressure considering the full spectrum and spectral decomposition for 0.3 MPa at the transducer surface. (e-h) Full spectrum and spectral decomposition for 4.5 MPa at the transducer surface. Note each figure has its own colour scale.

4.3 Results

4.3.1 Number 2

For the number '2' image, the acoustic hologram was first simulated in linear and non-linear regime to study the possible nonlinear effects at high pressure amplitudes needed for ultrasound hyperthermia. Three different pressure amplitudes at the surface of the transducer were considered: 0.3, 1.5 and 4.5 MPa, resulting in peak pressures of 1.2, 7.1

[1] The parameters for the MRI acquisition were TR/TE = 55/10 ms, 25-deg flip angle, 300 mm × 300 mm × 4 mm volume, 128 × 128 acquisition matrix using an in-plane pixel size of 2.3 mm, 6/8 Fourier reconstruction and 260-Hz/px bandwidth.

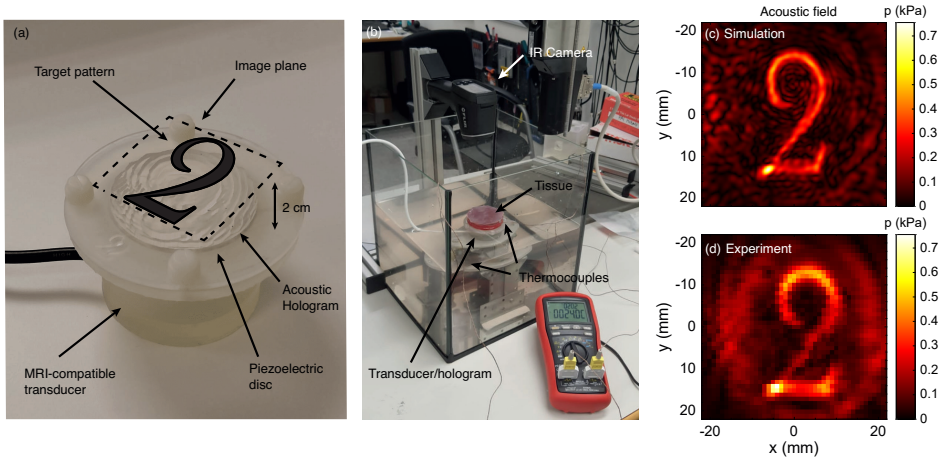

Figure 4.4: (a) MRI-compatible transducer and holographic lens. (b) Experimental setup for thermal measurements (schematic figures of experimental setups can be found in Supplementary Material S2). (c) Simulated acoustic pressure field. (d) Acoustic pressure field measured in degassed water.

and 29 MPa at the acoustic holographic image plane, which corresponds to mechanical indexes of 1.1, 4.9 and 12.6, respectively. Gol'dberg number of these three different regimes was 3.6, 17.9 and 53.7, respectively. As expected, contribution of harmonics to the acoustic field was significant at higher pressures: for 0.3 MPa source amplitude, only 4% of the total energy is carried by the second harmonic and 0.25% by the third harmonic, while for the 1.5 MPa case percentages of the total energy carried by the second and third harmonic were 15.5% and 3%, or for the 4.5 MPa case these same proportions were of 27% and 18%. Also, higher harmonics contribute to generate a sharper image, with more resolution, as shown in Figure 4.3.

Experimental evaluation of the acoustic field was done with the system described in the *Materials and Methods* section. Peak pressure values in steady state at the image plane measured by the needle hydrophone are represented in Figure 4.4 (d). Both experimental and acoustic field corresponding to the full-spectrum weakly nonlinear regime (Figure 4.4 (c)) were compared. In the region of the target image, relative error between both experimental and simulated fields is much lower than in the outer region, where random noise increases the error. Relative error was calculated as

$$\epsilon(\%) = \frac{p_{\mathrm{exp}}/\max(p_{\mathrm{exp}}) - p_{\mathrm{sim}}/\max(p_{\mathrm{sim}})}{p_{\mathrm{sim}}/\max(p_{\mathrm{sim}})} \times 100, \tag{4.5}$$

where p_{exp} and p_{sim} are the measured and simulated pressure fields respectively. Average relative error in the region of interest (without considering random noise) is 31%.

Discrepancies between the two pressure fields might be related to the fact that the holographic lens was designed for a liver-like medium but measured in water, which exhibits slightly different properties in terms of acoustic impedance and sound speed.

Thermal holographic pattern generated by the acoustic hologram would also depend on the contribution of each harmonic with its peak pressure, as the heating source term depends on the quadratic pressure of each harmonic and also on the attenuation, which increases with the harmonic order. Calculations show that for the higher pressure studied, nonlinear effects makes a slight difference with the linear pattern, which becomes more important in the regions of high pressure. The highest difference between linear and nonlinear thermal pattern is of 18% (relative to the nonlinear field) while average difference at the region of interest is 8.2%. Nevertheless, for hyperthermia applications, where maximum desired temperatures are of 45° C, pressure fields are in the weakly nonlinear regime, where no difference in the thermal pattern is found between linear and nonlinear propagation (Figure 4.5 (b)). Also, thermal patterns are dominated by heating diffusion, so the image blurs with time and is not as sharp and stable as the acoustic hologram.

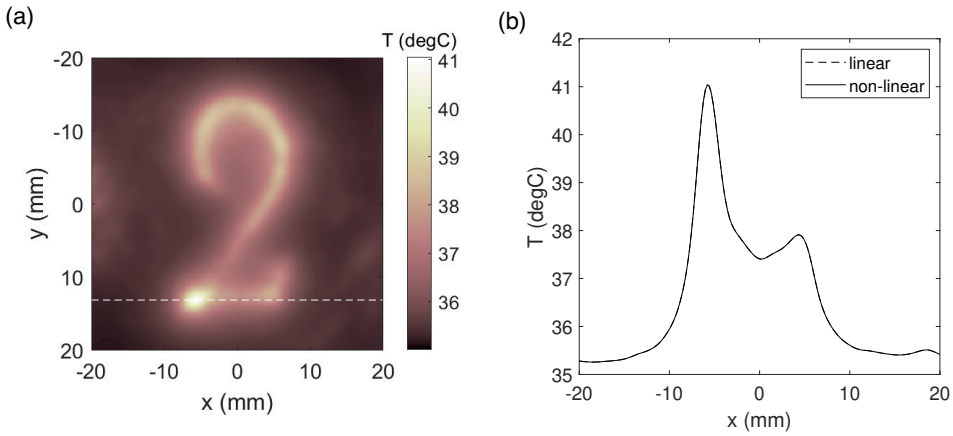

Figure 4.5: (a) Simulated thermal pattern for 0.3 MPa at the transducer surface (white dashed line represents location of lineal cuts). (b) Lineal cut for linear (dashed line) and nonlinear (solid line) propagation at 0.3 MPa.

Because IR radiation is strongly absorbed by water, IR-camera measurements were performed at the tissue surface, with the image plane located at the boundary between the soft-tissue and the air. Note that when using this setup ultrasound waves are strongly reflected at the boundary, because the impedance mismatch produces a nearly-perfect Neumann boundary condition for the pressure at the image plane. Even in these condi-

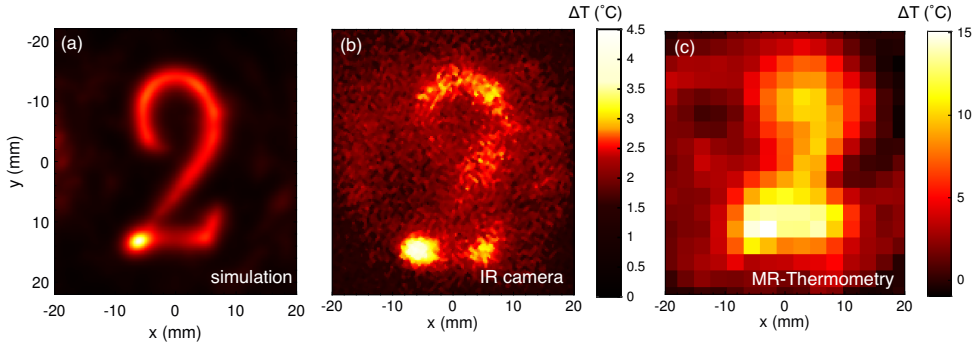

Figure 4.6: (a) Simulated thermal pattern in liver tissue after 12 seconds heating. (b) Thermal pattern measured with an infrared camera in liver tissue after 12 seconds heating and (c) measured with MR-thermometry after 40 seconds heating. The central vertical colour scale applies to (a) and (b).

tions, the target thermal pattern is observed, as Figure 4.6 (b) shows. The pattern matches the simulated one (Figure 4.6 (a)), with a peak temperature rise of $\Delta T = 4.5^{\circ}$ C after 12 seconds heating at 20 W. The temperature was measured locally by two thermocouples located in the water tank and at the lateral boundary of the tissue (see Figure 4.4 (b)), indicating that diffusion transports heat towards the boundary of the tissue in the long term, and the pattern becomes blurred. The concept was also validated in the bulk of a liver-mimicking gelatin-milk phantom using MRI-thermometry to minimize the influence of the previously-mentioned boundary condition. The measured thermal pattern using MRI at the image plane is presented in Figure 4.6 (c). HIFU heating was performed at 40 W acoustic power, leading to a temperature rise of $\Delta T = 15^{\circ}$ C after 40 seconds of heating. Both experiments demonstrate that the desired thermal pattern can be generated using holograms, showing the robustness of acoustic holograms to generate thermal patterns inside absorbing media. In both cases the thermal pattern is well defined until heat diffusion dominates and the central part of the hologram is almost uniformly heated, as it also occurs in simulations.

4.3.2 Wide hologram

For the wide target configuration, acoustic and thermal patterns were computed with k-space numerical simulations. Experimentally, temperature was measured using MR-thermometry in a liver-mimicking phantom, driving the source with a 1-MHz continuous signal at 80 W acoustic power without the lens and 200 W with the holographic lens [2].

[2]The parameters of the MRI acquisition were TR/TE = 42/10 ms, 300 mm × 300 mm × 6 mm, 128 × 128 acquisition matrix (using a 2.3-mm in-plane pixel size), 25-deg flip angle, 6/8 partial Fourier acquisition and a 260-Hz/px bandwidth.

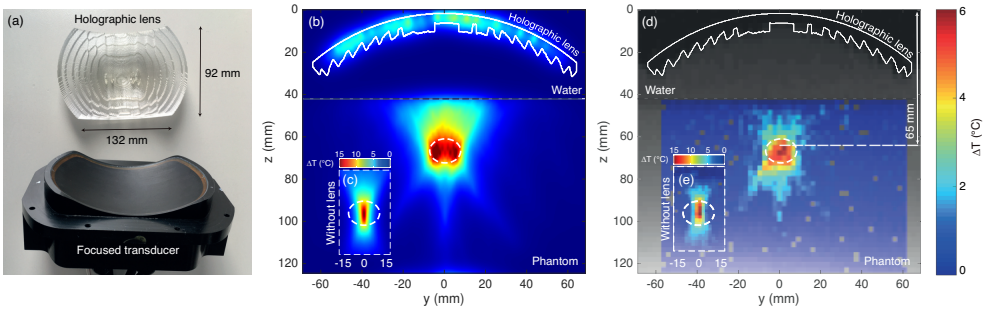

Figure 4.7: (a) Acoustic hologram and focused transducer for the second experimental setup. (b) Thermal simulation for a 1-cm wide target located at 65 mm from the focused transducer surface and (c) for the focused transducer without the lens. (d) MRI-thermometry measurement using the hologram and (e) for the focused transducer without the lens. The big vertical colour scale applies to (b) and (d).

The resulting patterns are shown in Figures 4.7 (b-e). A temperature rise of $\Delta T = 6^{\circ}$ C was observed in both simulation and MRI measurement of the system with lens after 30 seconds heating, while for the transducer-only setup the temperature rise was of $\Delta T = 15^{\circ}$ C in the same time.

A good agreement is found between simulations [Figures 4.7 (b, c)] and measurements [Figures 4.7 (d, e)]. In the absence of the lens, a narrow focal spot of 1.5 mm wide is found, located at a depth corresponding to the centre of curvature of the source (100 mm). However, using the holographic lens the focal spot widens and shifts axially 35 mm closer to the transducer surface, according to the planned design. Excellent agreement was found between thermal simulations and temperature maps measured by MR-thermometry. ROIs inside which experimental temperature elevation was greater than 4 degrees were 7 mm $\times$ 25 mm and 17 mm $\times$ 16 mm without and with the holographic lens, respectively, while these same regions have 7 mm $\times$ 30 mm and 11 mm $\times$ 16 mm sizes in the experiment. In addition, note that standard deviation inside these regions were equal to 40% of the maximum temperature without the lens, but only 12% using the hologram. A detail of the thermal pattern cross-section in the lateral direction at the focal distance is shown in Figures 4.8 (a, b). Data shows that a wider and more uniform heating region can be achieved using the holographic lens.Note this technology allows not only to enlarge focus size but also to change its position and length. The resulting holographic thermal pattern was widened about 2.5 times the original beam width, with a more uniform temperature distribution, and the focal distance was reduced to about half of its original axial location.

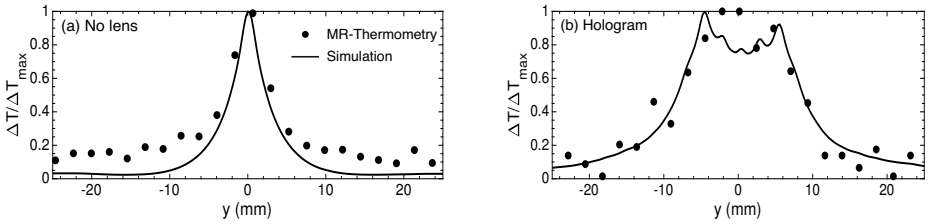

Figure 4.8: Thermal pattern cross-section at the focal distance (a) in the absence of the lens and (b) including the acoustic hologram.

4.4 Chapter conclusions

In this Chapter, we have demonstrated the potential of acoustic holograms to produce thermal holographic patterns inside soft tissues and tissue-mimicking phantoms. The temperature distributions were experimentally validated using an infrared camera at the surface of a cow liver, and MR thermometry in the bulk of a liver-mimicking phantom. The results show that using an acoustic hologram, the heat deposition can be spatially-modulated by shaping the acoustic field. This procedure results in devices that can be easily manufactured by rapid prototyping. A complete low-cost, MR-compatible device can be achieved by combining these holographic lenses with single-element piezoelectric transducers such as the one presented in the first part of this study. In this way, patient-specific thermal patterns with tuned and uniform focal spots can be generated, using a low-cost device without the need of expensive MRI-compatible phased-array transducers. Moreover, previous works [63] have also demonstrated that acoustic holograms can also encode phase-conjugated wavefronts to mitigate the phase aberrations of layered tissues, such as bones. Therefore, thermal holographic patterns could also be applied in transcranial therapy, or in any situation where aberrating layers distort the wavefront. In this way, holographic thermal patterns show a great potential for ultrasound hyperthermia treatments or physical therapy. They allow adapting the heating region to target therapeutical focal spots of arbitrary shape and location.

Publications

The contents of this Chapter have been presented in the following publications:

Journal papers

Andrés, D., Vappou, J., Jiménez, N., & Camarena, F. (2022). Thermal holographic patterns for ultrasound hyperthermia. Applied Physics Letters, 120(8).

Conference papers

Andrés, D., Vappou, J., Jiménez, N., & Camarena, F. 3D-printed acoustic holograms to generate thermal holographic patterns. *22nd International Symposium on Nonlinear Acoustics (ISNA22)*. Oxford, United Kingdom. July 4-8, 2022. Published in *Proceedings of Meetings on Acoustics (Vol. 48, No. 1). AIP Publishing*.

Andrés, D., Vappou, J., Jiménez, N., & Camarena, F. Thermal patterns generated by acoustic holographic lenses. *EUROMECH Colloquium 610: Emerging topics in acoustic and mechanical metamaterials*. Castellón de la Plana, Spain. April 25-27, 2022.

Andrés, D., Vappou, J., Jiménez, N., & Camarena, F. Thermal patterns generated by ultrasound holograms. *XXXVIII Reunión Bienal de la Real Sociedad Española de Física*. Murcia, Spain. July 11-15, 2022. **Award: Best Paper and Presentation Award for Young Researchers**.

Andrés, D., Vappou, J., Jiménez, N., & Camarena, F. Thermal patterns generated by ultrasound holograms. *European Congress and Exposition on Noise Control Engineering (EuroNoise 2021)*. Online. October 25-27, 2021. **Award: Winner of the Young Researchers' Competition**.

Andrés, D., Vappou, J., Jiménez, N., & Camarena, F. Ultrasonic Holograms to Enhance Hyperthermia Volumes. *2021 IEEE International Ultrasonics Symposium (IUS)*. Online. September 11-16, 2021. Published in *2021 IEEE International Ultrasonics Symposium (IUS) (ISBN: 978-0-7381-1209-1). IEEE*.

Chapter 5

Uniform thermal dose using tailored holograms

Ultrasound hyperthermia is currently used to treat cancer due to its ability to radio- and chemo-sensitize, and to stimulate the immune response, in a non-ionizing and non-invasive way. Nevertheless, achieving uniform and volumetric hyperthermia is challenging. In this Chapter, a novel focused ultrasound hyperthermia system based on 3D-printed acoustic holograms combined with a high intensity focused ultrasound (HIFU) transducer to produce a uniform iso-thermal dose in multiple targets is presented. The system is designed to treat several 3D cell aggregates contained in a tissue mimicking phantom with multiple wells, each holding a single tumour spheroid, with real-time temperature and thermal dose monitoring. System performance was validated using acoustic and thermal methods, ultimately yielding thermal doses in 3 wells which differed by less than 4%. This Chapter was born as part of a collaboration and research stay at the Institute for Cancer Reserach (ICR) in London.

5.1 Introduction

Hyperthermia, commonly defined as an increase in tissue temperature to between 39 and 45 °C, is a well-established form of cancer treatment with proven efficacy as a radio- or chemo-sensitizer [124]. When applied to the whole body, it has been observed that there is an enhanced immune response [125]. Various clinical techniques for delivering hyperthermia exist. These include electro-magnetic, ultrasonic, conductive (via hysteresis of magnetic nanoparticles inside the body) heating and hyperthermic perfusion [126]. Among these, ultrasound is the only non-invasive method capable of inducing highly localized hyperthermia inside the body without using endogenous contrast. By using focused ultrasound, the mechanical energy of an acoustic wavefront can be concentrated on the focal volume of the system, and tissue is heated locally mainly through the activation of thermoviscous processes [127]. 3D cell aggregates known as spheroids mimic the in vivo response of tumours to treatments better than do 2D monolayers [128]. Cancer cell response to hyperthermia delivered with good temperature accuracy using a polymerase chain reaction (PCR) thermal cycler has been studied in single-cell suspensions and 3D tumour models, showing significant differences between the two models [129, 130, 131]. However, such studies are potentially limited because they lack the non-thermal mechanisms by which ultrasound may affect cell growth. Experiments with ultrasound on tumour spheroids in vitro have been performed to study drug delivery [132, 133], and more recently to study spheroid response to heating using different ultrasound parameters in a non-absorbing fluid medium [134].

Ultrasound-induced hyperthermia is commonly delivered using a focused ultrasound (FUS) transducer, which concentrates the mechanical energy into a focal spot. Therefore, in practice, achieving adequate uniform heating throughout targets larger than the focus requires multiple, repeated sonications in different positions [50, 46] and/or sophisticated and expensive phased-array technology to steer the focus rapidly [135, 136]. 3D-printed acoustic lenses can be used to overcome this difficulty. In Chapter 4 it has been proven that holographic lenses can generate thermal patterns. However, using this approach, the temperature rise is not uniform throughout the whole target.

The aim of this Chapter is to create a novel ultrasound hyperthermia system based on acoustic holograms capable of delivering a uniform thermal iso-effective dose (TID) over complex targets and to use it initially to study how ultrasound hyperthermia affects tumour spheroids in vitro. Using this approach, several spheroids were treated simultaneously in order to provide repeatable exposure conditions over several experimental samples. A holder in which spheroids could be heated to a target TID with ultrasound while temperature is being monitored in real-time was developed. The novel system, based on an ultrasound absorbing (tissue mimicking) gel phantom with three miniature wells with ultra-fine wire thermocouples below each, was initially designed to characterize

the hyperthermia-lens system thermally, and subsequently to expose tumour spheroids to predefined, well controlled TIDs. Two holographic lenses which split the transducer's geometric focus into several foci were compared. The first lens was designed to provide acoustically similar foci that could be targeted on each spheroid containing well of the phantom. The second hologram was tailored to produce similar heating rates at each spheroid. The acoustic and thermal performances of the lenses were measured and compared with modelling predictions. The ability to deliver a uniform TID to multiple U87-MG cell spheroids was investigated. Their growth response and viability were compared to that of thermocycler heated spheroids.

While this system has only been tested here on spheroids, a long-term goal is to provide a hyperthermia system capable of providing uniform thermal dose over the entire volume of a pre-clinical in vivo tumour. However, an in vitro method capable of simultaneously heating a number of 3D tumour mimics (spheroids) placed in a phantom that represents the heating seen in soft tissues in vivo (using the IEC ultrasound tissue mimic), will allow more clinically relevant in vitro experiments to be undertaken, thus reducing the number of animals needed to establish appropriate treatment regimens.

5.2 Materials and Methods

5.2.1 Holographic ultrasound system design

The ultrasound hyperthermia system consisted of a focused ultrasound transducer coupled to a holographically-designed, 3D-printed acoustic lens. The lenses were created using time-reversal methods with virtual sources and performing pseudo-spectral time-domain simulations as described in Chapter 2. In addition, in this Chapter we characterized the inhomogeneous transducer vibration along its surface and included this information in the time-reversal simulations for the lens tuning and evaluation.

Two design strategies were investigated, each of which aimed to produce an acoustic focus in individual spheroid-containing wells of the holder described below. Figure 5.1 summarizes both strategies. The first, acoustic (iso-pressure) strategy, aimed to achieve equal acoustic peak pressures at each of the spheroid locations (i.e., at each focus). However, due to heat diffusion, this very simple strategy may not yield a uniform thermal dose delivery to each spheroid. Therefore, a second, more complex approach of producing a uniform thermal distribution was investigated, the iso-thermal strategy. In order to produce a more uniform TID at each focal peak (spheroid) position, lower amplitude acoustic pressures were used more centrally, where the rate of cooling is lower, and higher amplitudes were used more laterally where cooling was highest. For the iso-thermal ap-

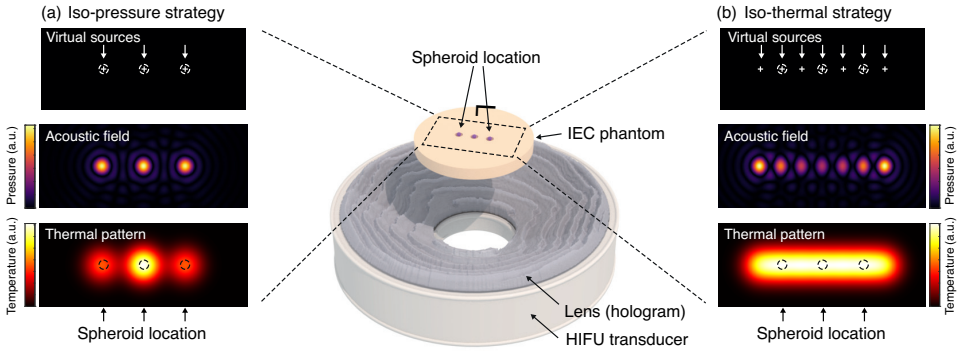

Figure 5.1: The two acoustic hologram design strategies. (a) Iso-pressure strategy, where the hologram is designed by setting a virtual source at each target location, resulting in a uniform acoustic pressure field at each target. (b) Iso-thermal strategy, where the lens is designed by locating a set of virtual sources, of tuned amplitude and phase, covering the target locations, resulting in an uneven acoustic field but uniform thermal pattern.

proach a first guess at a distribution of focal peak pressures was used, the acoustic field was modelled and, from this, thermal simulation was performed until the medium arrived at equilibrium (a steady state temperature). This process was repeated iteratively, lowering the pressure in the areas where the temperature was still too high, so as to approach a solution in which the thermal dose at each focal peak was the same.

For the iso-pressure design strategy, as shown in Figure 5.1 (a), a 3-focus hologram with 2 mm focal separation was produced in order to obtain a similar acoustic field in each of the three spheroid wells. Three virtual sources were placed at a distance of z = 40 mm from the transducer surface, at the centre on the x-axis (up, down), and at the well locations -2, 0 and 2 mm on the y-axis. During the iso-pressure design simulations, all virtual sources within the target region(s) emitted sinusoidal signals with the same amplitude and phase since the aim was to produce three foci with similar acoustic pressure.

For the iso-thermal strategy, as shown in Figure 5.1 (b), a 7-focus hologram with a separation of 1 mm between maxima was designed. Seven virtual sources were placed 40 mm (z) from the transducer surface at the centre of the x-axis and at locations -3, -2, -1, 0, 1, 2 and 3 mm on the y-axis. Each of these emitted continuous sinusoidal signals with different amplitudes and opposed phases two-by-two. In this case, the whole backward and forward modelling process was repeated iteratively, thus tuning the virtual-source amplitudes to obtain a uniform thermal field by setting lower amplitudes for the central virtual sources accounting for thermal conduction from the lateral foci. Due to the long temporal duration of each iteration (each acoustic simulation lasted 600 minutes and each

thermal simulation lasted 300 minutes on an Intel ® Xeon CPU e5-2608 v2 workstation), no optimization algorithm was applied, and source weights were tuned manually. Progressively reducing the amplitude of the central virtual source resulted in a uniform TID in the targets due to the compensation between the heating rate and heat transport mechanisms in different areas.

Holographic lenses corresponding to these two strategies were designed for a focused transducer as described in Chapter 2, leading to two different curvilinear holograms. Once the lenses were designed, they were manufactured and attached to the transducer, as shown in Figure 5.2 (a). PolyJet technology was used to 3D print the lenses using VeroClear resin (Objet30 printer (Stratasys, Israel)). An image of a lens used in this study is shown in the inset of Figure 5.2 (b) .

5.2.2 Acoustic field validation

The acoustic field produced by the holographic lenses was measured using a hydrophone in a water tank filled with degassed (<3 mg/L dissolved oxygen), deionized water at room temperature (21 °C). The hydrophone (HNA-0400, ONDA Corp, CA, USA) was mounted on an automated 3D positioning system (UMS, Precision Acoustics, Dorset, UK). The 1.66MHz source was a H148-MR piezo-ceramic transducer (Sonic Concepts Inc, WA, USA), with a 63.2- mm radius of curvature, 64- mm outer diameter and 23- mm inner hole diameter, mounted in a fixed position and driven with sinusoidal pulsed-burst signals (40 cycles, PRF = 200 Hz, 40 mVpp) from a signal generator (33250A, Agilent, CA, USA), after 55 dB amplification (A300, E & I, NY, USA). Signals were recorded using a digital oscilloscope (64Xi, LeCroy, NY, USA), using a time window of 20 μs after reaching steady state, to avoid the ramp up period. A total of 20 waveforms per measurement point were averaged.

The uniformity of source vibration across the transducer surface, in the absence of the lens, was measured and used as input for the lens design and numerical evaluation. A 2D measurement in a plane parallel to the transducer face, and 15 mm closer to the transducer than the focal peak, was performed. The scan, designed to cover the active beam, was carried out from -12 mm to 12 mm in both x and y directions, with a spatial resolution of 0.3 mm, and a signal generator setting of 50.2 mVpp. The measured field was back-projected to the transducer surface using the Rayleigh-Sommerfeld integration, as described by Sapozhnikov et al. [137].

To evaluate the acoustic field generated by the holographic lenses, software-controlled 2D scans were made through the central focal peak, in a plane parallel to the transducer face, using a grid of 81 $\times$ 21 points and with spatial resolution of 0.1 mm.

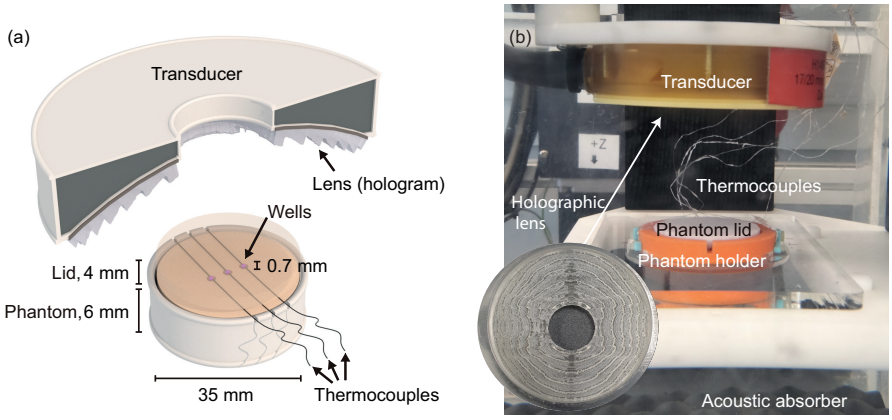

Figure 5.2: (a) Schematic of the spheroid exposure system with its dimensions. (b) Experimental setup to expose the spheroids to ultrasound hyperthermia. The inset shows the 3D-printed lens for the iso-thermal strategy.

5.2.3 Thermal exposure system

In order to evaluate the thermal profile produced with the holographic lenses, and to subject (500 to 800 μm diameter) spheroids to a precisely controlled iso-thermal dose, a new exposure system was designed. The system needed to absorb ultrasound in a similar way to tissue, and to heat spheroids, and be instrumented so that temperature and TID could be accurately monitored. In order that several spheroids could be exposed simultaneously to the same TID, one spheroid was held in each of 3 separate miniature wells (0.7 mm deep and 1 mm diameter) spaced 2 mm apart, as shown in Figure 5.3 (a) and Figure 5.3 (d). Thermocouples (detailed below) were manually placed in the mould, aligned with the middle of each well but 0.5 mm below its bottom so they would be embedded in the gel. These provided an estimate of the temperature achieved in each well, see Figure 5.2 (a). Although 3 wells were chosen for this holder, the technique should also be applicable to a larger number.

Once the thermocouples were in place, the moulds were filled with the acoustically absorbing IEC tissue mimic (IEC 60601-2-5:2015) [138]. Phenol red (3%) was added during gel manufacture to improve the ability to visualize the spheroids in the well, and to aid their removal after exposure. The dye had negligible impact on gel acoustic properties as measured with an in house system [139]. Spheroid holder bases were 4 mm thick, and separate gel lids were made that were also 4 mm thick, so that the bottom of the spheroid containing well lay 5 mm beneath the top surface of the holder.

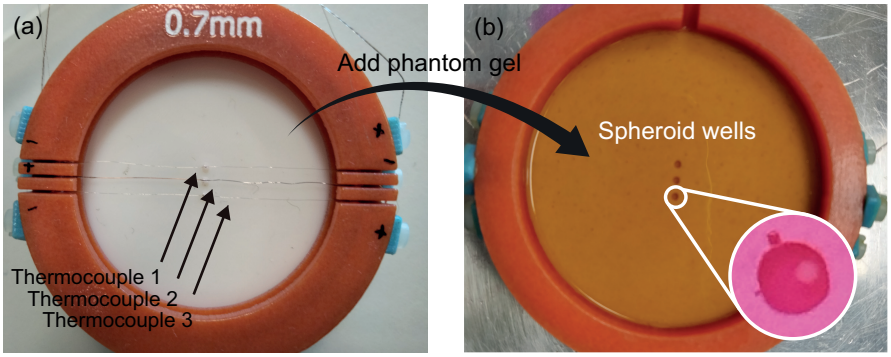

Figure 5.3: (a) The mould used to form the absorbing gel phantom with the three thermocouples located 0.5 mm above the protrusion used to form each well. (b) The mould filled with IEC tissue mimicking gel, with 3 miniature wells into which a spheroid could be placed (inset).

Thermal measurements were made with the spheroid holder in a fixed location, immersed in degassed water at constant 38 °C, obtained using a recirculation circuit consisting of a water chiller (HC-100A, Hailea, Guangdong, China) and a degasser (2.5 × 8 Liqui-Cel Membrane Contactor, 3M, NC, USA), connected to a vacuum line (27 in. Hg) plus a water heater (GD 100, Grant scientific, Cambridgeshire, UK) placed in the exposure tank (Figure 5.2 (b)).

During exposures, temperature was recorded using the three embedded 75- μm diameter T-type thermocouples (COCO-003, Omega, Manchester, UK) connected to a high-density thermocouple module (NI-9213, National Instruments, Tx, USA) used in high resolution mode to obtain 1 measurement per second. The transducer was mounted on a 3D positioning system with 60-micron movement resolution. The temperature resolution was of $\pm$ 0.1 °C. No attempt was made to compensate for potential thermocouple measurement artefacts, as viscous heating should be $<$ 25% of the measured values [140].

Firstly, the transducer's natural geometric acoustic focus was localized on the central thermocouple, using a grid of one second sonications followed by nine seconds cooling time during which the transducer was moved to the next position. The three cartesian axes were interrogated separately using spatial steps down to 0.25 mm. The same protocol was followed to locate the other two thermocouples relative to the central one.

Secondly, the lens was mounted on the transducer and the axial distance altered to reflect the expected difference in focal position (10 mm). The central thermocouple was re-localised as described. Four to five minute exposures with continuous signal from -1 mm to 1 mm with a spatial step of 0.25 mm along the y-axis were then performed, aiming to

achieve an equilibrium state in temperature, to evaluate the TID received by the spheroids in each well.

The thermometry system captured the temperature on the thermocouples as a function of time. TID was calculated as [141]

$$TID = \sum_{i=1}^{n} t_i \cdot R^{43-T_i} \tag{5.1}$$

Where TID is the thermal dose in units of cumulative equivalent minutes at 43 °C (CEM_{43}), t_i is the i-th time interval, T_i is the average temperature during time interval t_i and R is related to the temperature dependence of the rate of cell death, defined as $R(T$ < 43 °C) = 1/4, $R(T > 43$ °C) = 1/2.

The in-house software used to measure and record temperature also displayed accumulated TID, thus enabling exposures to be halted once a pre-determined dose had been accumulated. Experiments in the absence of spheroids showed that a predictable, and repeatable, TID accumulated once exposures were halted. This was used to manually achieve TID delivery to spheroids. Spheroid exposures ended once one of the three thermocouples reached a TID of 120 CEM_{43} for the 3-focus lens, and 60 CEM_{43} TID for the 7-focus lens.

5.2.4 Acoustic and thermal simulations

To evaluate the performance of the holographic lenses, acoustic and thermal numerical simulations were performed using k-Wave software [117]. All simulations used a 492 × 492 × 492-point grid, with a Perfect Matching Layer (PML) of 10 grid points each side, and with homogeneous spatial resolution of λ/6, where λ is the wavelength in water (λ = 0.91 mm). The transducer was modelled as a spherical cap with a central hole, each point emitting a continuous sinusoidal signal of amplitude and phase given by the measured ceramic vibration. The medium was considered to be homogeneous, with water properties of: temperature = 38 °C, density ρ_0 = 1000 kg/m^3, sound speed c_0 = 1520 m/s and attenuation coefficient α_0 = 0.0023 dB/(cm MHz^2). Water temperature was set to match that used in the experiments, and water density, sound speed and attenuation were calculated according to references [142, 143, 78], respectively. The lens was 3D printed using VeroClear resin properties measured in the laboratory with pulse-echo, finite amplitude insertion-loss techniques: ρ_L = 1181 kg/m^3 and c_L = 2525 m/s, and with acoustic absorption set to α_L = 1.65 dB/(cm MHz$^\gamma$), with γ = 1.1 the attenuation power-law frequency exponent, as reported in [51]. A total simulation time of 50 μs was used, with a 20 ns time step, and the maximum peak pressure amplitude in the last three

cycles in steady state was recorded at all grid points to give a steady state pressure map for comparison with experiment.

Thermal simulations were based on a pseudo-spectral time-domain numerical solution of Penne's bio-heat equation [123]. For the in vitro system, phantom dimensions and characteristics were used, and it was assumed to be surrounded by water. Its acoustic properties were set to ρ_p = 1050 kg/m^3, c_p = 1540 m/s, values reported by the IEC standard (IEC 60601-2-37:2007). Phantom specific heat capacity and thermal conductivity were set to C_p = 3550 J/(kg $\cdot$ K) and k_p = 0.52 W/(m $\cdot$ K), respectively, while for the water these parameters were C_0 = 4185 J/(kg $\cdot$ K) and k_0 = 0.62 W/(m $\cdot$ K). Cooling due to perfusion was not relevant. After studying the convergence of the simulation, heating times up to 10 minutes were simulated, with time steps of 0.5 s. The initial temperature was set to 38 °C in all media. At each time step, the water temperature was set to this initial value to replicate experimental conditions in which the water was maintained at a constant temperature. Pressure at each point was set to that measured with the hydrophone in water to match experimental conditions. The volume rate of heat deposition in the medium was defined as $Q = \alpha_p p^2/\rho_p c_p$. The relationship between the temperature (T) difference from baseline (T_0), pressure (p) and the volume rate of heat deposition (Q) was found to be $T = 2 \cdot 10^7 Q/p^2 + T_0$, and the attenuation value of the phantom that best matched simulation with experiment was α_p = 0.67 dB/(cm-MHz$^\gamma$). This was used in the thermal simulations for both lenses.

5.2.5 Tumour spheroid exposure

U87-MG cells (ATCC, London, UK) were maintained as a sub-confluent monolayer at 37 °C in 75 cm^2 flasks in a humidified atmosphere containing 5% CO_2. They were propagated using Dulbecco's modified Eagle medium (DMEM) supplemented with 10% hybridoma cell culture grade fetal bovine serum (SIGMA, Poole, UK), 2mM L-glutamine, 50 U/ml penicillin, 50 mg/ml streptomycin B, 0.25 lg/ml amphotericin B and sub-cultured using Accutase (SIGMA, Poole, UK). Screening for mycoplasma contamination was carried out on a monthly basis. Spheroids were created by plating 20.000 U87-MG cells in the wells of an ultra-low attachment (ULA) U-shaped well plates (96-well 7007, Corning, NY, USA). Cells were allowed to aggregate for 48 hours to form spheroids. For ultrasound exposure, spheroids were transferred from the U-shaped well plates to the empty phantom's wells using wide bore pipette tips (Alpha Laboratories, Eastleigh, UK). Work was carried out aseptically where possible and antibiotics, as described above, were used to minimise the risk of contamination. To maintain spheroids in a fixed location inside the phantom wells they were sealed using 4 μL of matrigel. The matrigel (and spheroids) were allowed to set for 10 minutes, and then the lid was placed on the phantom. The spheroids were then exposed to ultrasound hyperthermia. Two sets of three

tumour spheroids (six in total) were exposed to TIDs of 7.5, 30, 60 or 120 CEM_{43}. Eight spheroids were placed in the wells, and placed in the exposure tank, but not exposed to ultrasound (sham exposures). Spheroid sizes ranged between 0.5 and 0.8 mm at the time of exposure. TID was controlled by monitoring temperature (and TID) in all 3 wells in real time. As the central well approached the intended TID, the exposure was halted manually, to take into account the probable dose accumulation during cooling, determined during measurements made in the absence of spheroids. The cooling phase contributed $< 2.4 \pm 0.2$ % of the total dose. At the end of the cooling phase, the phantom was dismantled, and spheroids were pipetted back into the ULA plates. These plates were then incubated in a humidified incubator at 37 °C, 5 % CO_2. For thermocycler heating, a calibrated PCR thermal cycler (C100 Touch Thermal Cycler, Bio-rad, CA, USA) utilising a Peltier thermoelectric system to transfer thermal energy was used to expose U87-MG spheroids to TIDs of 0, 30, 60 and 120 CEM_{43} using temperatures of 37, 44, 45 and 46 °C, respectively for 15 minutes as described in previous publications [128, 129, 130]. A TID of 7.5 CEM_{43}, was achieved by heating spheroids to 43 °C for 7.5 minutes. Spheroids were then incubated in ULA plates in the same way as for ultrasound-heated spheroids.

5.2.6 Size and adenosine triphosphate measurements

For size measurements, the mean diameter of each spheroid was measured with a high-throughput digital microscope (Celigo Image Cytometer, Nexcelom, MA, USA) using high accuracy filters, automated high brightness focus, only 1 spheroid per well, and pixel intensity of 0-120. Spheroid pictures were also collected using the Celigo. The Cell Titer Glo 3D assay (Promega, WI, USA) was used as described in the supplier's handbook, to provide a relative measure of the intracellular ATP (adenosine triphosphate) present in the spheroids, and thus indicate their viability via this measure of metabolic activity. Briefly, spheroids in 100 μL media were transferred to white 96-well flat bottom plates and incubated with 25 μL of Cell Titer Glo for 30 minutes at room temperature with gentle agitation. Signal from each bubble-free well was immediately detected using a luminescent microplate reader (FLUOstar Optima, BMG Labtech, Ortenberg, Germany). Data were then processed in Excel.

5.2.7 Statistical analysis

Microscopy size results are presented as mean ± standard deviation (SD) of n = 3 spheroids for thermocycler heating experiments, and for ultrasound-heating experiments, n = 8 for sham exposed spheroids, n = 5 for 7.5, 30 and 60 CEM_{43} exposed spheroids and n = 3 for 120 CEM_{43} exposed spheroids. Statistical significance was calculated using a 2-way unpaired Student's t-test assuming unequal variance. P values < 0.05 were considered statistically significant.

5.3 Results

5.3.1 Transducer Vibration Evaluation

In order to gain an understanding of how the transducer ceramic was vibrating in practice, needed for improved acoustic simulation of the transducer-lens system compared to an assumption of uniformity across the entire surface, holographic measurements of the acoustic pressure were made at the transducer surface as described in the section 5.2.2. The measured field was projected back to the transducer surface using the Rayleigh-Sommerfeld integration as described by Sapozhnikov et al. [137]. This projection is shown in Figure 5.4 (a). Using this data, a forward simulation was performed to evaluate the focus shape and amplitude, resulting in the field shown in Figure 5.4 (b). Results of this calculation were compared with those obtained for homogeneous vibration of the whole transducer (Figure 5.4 (d)), and with direct experimental measurements at the peak-pressure position (Figure 5.4 (e)). The maximum peak acoustic pressure measured with the hydrophone at the focus was 0.21 MPa, and the same value modelled using the real back-projected amplitude of the transducer was 0.2 MPa. Discrepancies between these values may be due to the uncertainty in the geometry of the ceramic, which was modelled to have the diameter and radius of curvature given by the manufacturer. Full width at half maximum (FWHM) values for the homogeneous vibration simulation, real vibration simulation and measured data, respectively, were 1.2 ± 0.1, 1.2 ± 0.1 and 1.3 ± 0.1 (x direction), 1.2 ± 0.1, 1.3 ± 0.1 and 1.2 ± 0.1 (y direction), and 9.1 ± 0.1, 11.6 ± 0.1 and 11.7 ± 0.1 (z-direction). Figures 5.4 (c) and Figure 5.4 (f) show transversal and axial cuts of the three field, where it can be seen that the inhomogeneous vibration of the transducer affects the measured acoustic field.

The results show that ceramic vibration affects the resulting acoustic hologram and so it is important that it is well characterized in order to achieve a better match between simulation and experiment. This asymmetric vibration was considered in all the simulations along the Chapter.

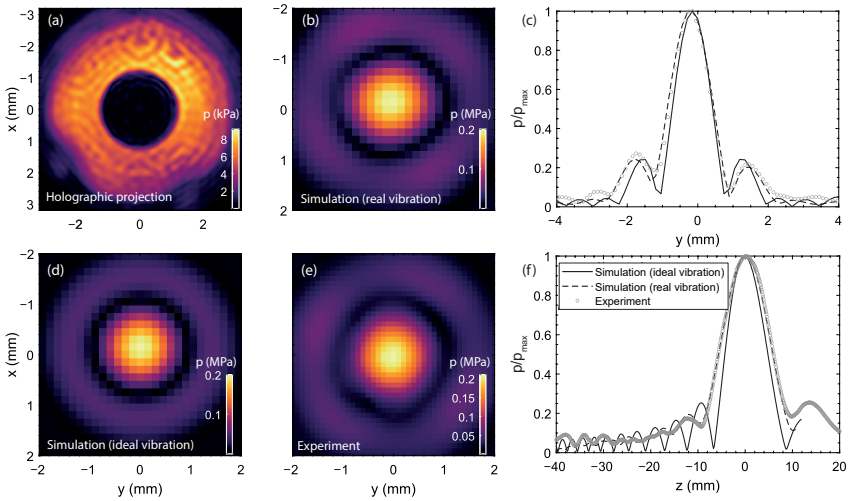

Figure 5.4: (a) Back projection of the measured acoustic pressure onto the transducer surface, showing the pressure distribution over the transducer surface. (b) Simulation of the focal acoustic pressure using the ceramic's actual vibration. (c) x-cut through the focal peak (simulations and experiment). (d) Simulation of the focal acoustic pressure assuming homogeneous surface vibration. (e) Experimental measurement. (f) z-cut through the acoustic maximum (simulations and experiment).

5.3.2 Lens for iso-pressure focal peaks (3-focus)

Figure 5.5 (a) shows a transverse 2D plot through the central acoustic focal peak of the 3-focus (acoustic iso-pressure strategy) lens modelled in water. The comparable measured acoustic field at 40 mVpp driving voltage is shown in Figure 5.5 (b). Peak positive pressures measured at each focus (left to right in figure) were 0.84 ± 0.05, 0.7 ± 0.05, and 0.8 ± 0.02 MPa and matched well with the simulation. Errors were obtained as the standard deviation between the maximum peak pressure over the 20-cycle signals at the focus. A normalized linear plot through the central focal peak is shown in Figure 5.5 (c). The three foci have FWHM values of 0.85 ± 0.05, 0.89 ± 0.05 and 0.91 ± 0.05 mm, and were deviated +0.1, -0.1 and -0.2 mm relative to their simulated locations on the y axis. The two lateral foci had the highest pressure, with the central focus being 15% lower amplitude. For thermal exposures, where 85 mVpp driving voltage was used, the peak positive pressures at each focus were 1.34 ± 0.08, 1.12 ± 0.08, 1.28 ± 0.03 MPa.

As described earlier, each thermocouple in the phantom holder was localised using the transducer's geometric focus. Their positions, relative to the central one (on the z axis), were (0, -2, 0) $\pm$ 0.25 mm and (0, 2, 0) $\pm$ 0.25 mm. Using the 3-focus holographic lens and continuous exposures at 85 mVpp, sonications were performed moving the trans-

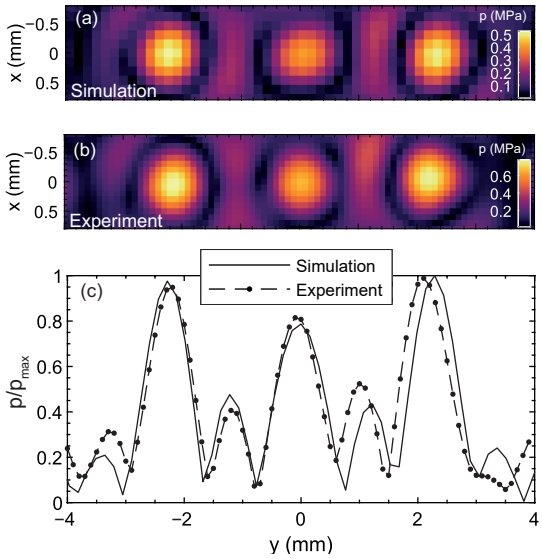

Figure 5.5: Acoustic pressure field for the three-focus hologram in the x-y plane at z = 40 mm: (a) simulation (b) experimental hydrophone measurement. (c) normalized hydrophone measured y-axis plot through the pressure maxima.

ducer from -1 mm to 1 mm around the central location, with spatial steps of 0.25 mm and exposure times of around 5 minutes, until the central thermocouple reached a TID of approximately 120 CEM_{43}. Thermal profiles recorded at each localised thermocouple are shown in Figure 5.6. Maximum focal peak temperatures were 48.0 $\pm$ 0.1, 48.7 $\pm$ 0.1 and 47.2 $\pm$ 0.1 °C, from left to right, respectively. These values correspond to TIDs of 72.8 $\pm$ 6, 114.3 $\pm$ 9 and 41 $\pm$ 3 CEM_{43} after 5 minutes of continuous heating. Mean TID in each well was calculated as the mean TID in measurements made between -0.5 and 0.5 mm around the central location for each thermocouple, as this is the uncertainty in the spheroid location, and the error in this value is obtained as the standard deviation of these measurements. With this calculation, mean TIDs at each well were 73 $\pm$ 13, 103 $\pm$ 14 and 38 $\pm$ 6 CEM_{43}, from left to right. Comparing the mean TID in the central well with the others, gives a relative error of 29.1% for the one located at its left, and 63.1% at its right, while the difference between the left and the right wells was 47.9%.

Note that even the acoustic field is balanced for the +2 mm and -2 mm foci, the thermal field is not. This difference might be caused for a slight misalignment in the thermocouple location relative to the location of the focus. As this thermal field is very inhomogeneous in the target region, small misalignments in location might result in a much lower recorded thermal field.

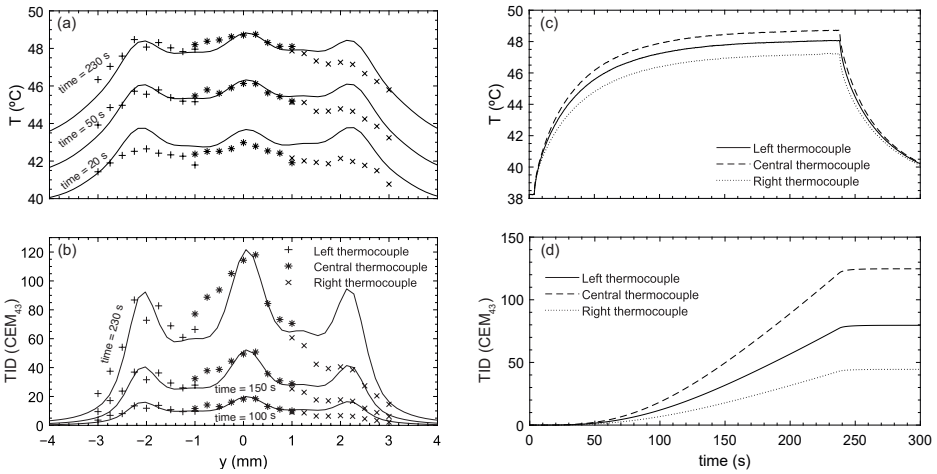

Figure 5.6: Lens for iso-pressure focal peaks. (a) Temperature profile at different time points simulated (solid line) and measured experimentally with each thermocouple. (b) TID profile at different time points simulated (solid line) and measured experimentally with each thermocouple. (c) Experimental temperature profile over time at the central position measured by each thermocouple. (d) Experimental TID profile over time at the central position measured by each thermocouple.

5.3.3 Lens for iso-thermal dose (7-focus)

Figure 5.7 (a) shows a simulated transverse 2D plot through the focal peak of the central focus of the 7-focus lens and the measured acoustic field at 40 mVpp driving voltage, (see Figure 5.7 (b). Peak positive pressures at each focus were (left to right): 0.65 $\pm$ 0.06, 0.50 $\pm$ 0.05, 0.49 $\pm$ 0.05, 0.41 $\pm$ 0.05, 0.54 $\pm$ 0.03, 0.55 $\pm$ 0.04, 0.68 $\pm$ 0.03 MPa. These matched well with the simulation. A normalized linear cut through the acoustic maximum is shown in Figure 5.7 (c). Seven focal spots separated by 1.0 $\pm$ 0.1 mm appeared in the same locations as in the simulation. There is a difference in maximum acoustic pressures of up to 40% between the seven foci. For thermal exposures, where 85 mVpp driving voltage was used, the peak positive pressures at each focus were 1.04 $\pm$ 0.09, 0.80 $\pm$ 0.08, 0.78 $\pm$ 0.08, 0.66 $\pm$ 0.08, 0.86 $\pm$ 0.05, 0.88 $\pm$ 0.06 and 1.09 $\pm$ 0.05 MPa, from left to right.

The same protocol as with the 3-focus lens was followed. With the 7-focus lens-focused transducer system, continuous exposures at a drive of 85 mVpp, designed to achieve 60 CEM_{43} TID at the central thermocouple, were used. These sonications were performed as described above., using exposure times of 7.5 minutes. The temperature-time profile recorded at each thermocouple is shown in Figure 5.8. The maximum steady-state temperatures registered by each thermocouple were 46.4 $\pm$ 0.1, 46.4 $\pm$ 0.1 and 46.3 $\pm$

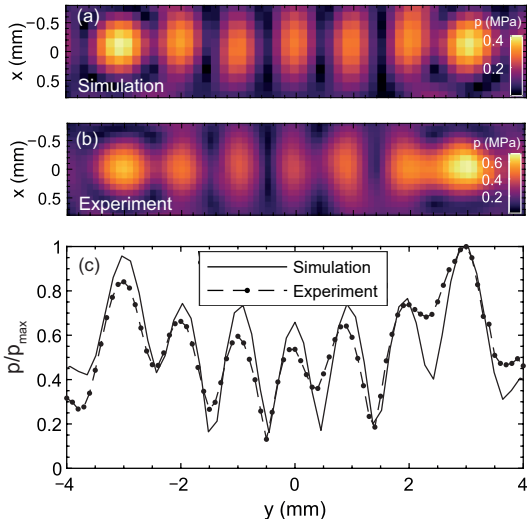

Figure 5.7: Acoustic pressure field for the seven-focus hologram in the x-y plane at z = 40 mm: (A) simulation (B) experimental hydrophone measurements. (C) normalized hydrophone measured y-axis plot over the pressure maxima.

0.1 °C, from left to right. These values correspond to measured TIDs of 60 ± 5, 58 ± 5 and 57 ± 5 CEM_{43}. Mean TIDs (calculated as described for the 3-focus lens) for each well were 56 ± 5, 54 ± 4 and 54 ± 3 CEM_{43}, from left to right. Comparison of the mean TID in the central well with the others, gives a relative difference of 3.7% for the one located to its left, and 0.03 % to its right.

5.3.4 Spheroid study

U87-MG tumour spheroids were exposed to ultrasound heating using TIDs of 7.5, 30, 60 and 120 CEM_{43} (six for each condition). Due to early inexperience with the use of pipettes for removing spheroids from the wells, five were retrieved for each condition, except for those exposed to 120 CEM_{43} for which three were retrieved. Eight spheroids were sham-exposed. Figure 5.9 (a) and Figure 5.9 (b) show the evolution over 10 days of a sham-exposed spheroid (growth) and an ultrasound-induced 120 CEM_{43} exposed spheroid (shrinkage), respectively. Figure 5.9 (c) shows growth curves for ultrasound- and thermocycler-heated spheroids over a 10-day period. Sham- and 7.5 CEM_{43} ultrasound-exposed spheroids continued to grow, increasing their size by approximately 40 ± 4% in 10 days. Shrinkage of spheroids by approximately 15 ± 6% was seen when they were ultrasound-treated to a TID of 120 CEM_{43}, whereas no shrinkage or growth was seen at 30 or 60 CEM_{43}. No shrinkage was seen in the thermocycler-heated spheroids

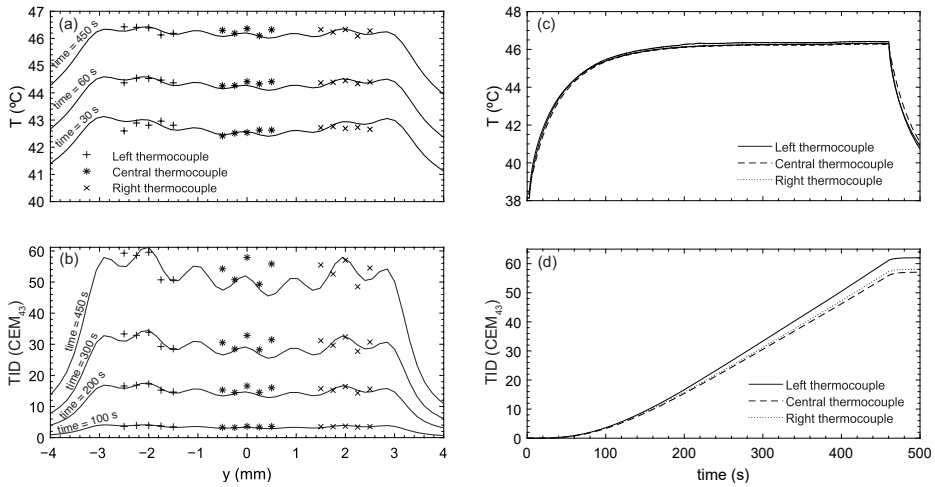

Figure 5.8: Lens for iso-thermal dose distribution. (a) Temperature profile at different time points simulated (solid line) and measured experimentally for each thermocouple. (b) TID profile at different time points simulated (solid line) and measured experimentally for each thermocouple. (c) Experimental temperature profile over time at the central position measured by each thermocouple. (d) Experimental TID profile over time at the central position measured by each thermocouple.

exposed to TIDs of 0, 7.5, 30, 60 or 120 CEM_{43} Ten days after treatment U87-MG spheroids exposed to ultrasound showed greater reduction in growth than those heated using a thermocycler (Figure 5.10 (a)). For example, the size of spheroids exposed to ultrasound at TID of 120 CEM_{43} was $33 \pm 5\%$ smaller than that of sham ultrasound-treated spheroids 10 days after treatment. When the same TID was delivered to the spheroids using thermocycler-heating their size did not present a significant reduction compared to sham-exposed spheroids at this time point (Figure 5.10 (a)). Differences in size between HIFU and thermocycler heated spheroids are statistically significant for all TIDs.

The metabolic activity of spheroids, indicative of their viability, was also assessed 10 days after heat treatment. Figure 5.10 (b) shows a statistically significant reduction in spheroid viability when exposed to ultrasound-heating with TIDs of 30, 60 and 120 CEM_{43} (with relative viability of $27 \pm 42\%$, $4 \pm 2\%$ and $5 \pm 10\%$, respectively compared to sham-exposed spheroids). Non statistically significant differences in viability were seen when spheroids were exposed to US -heating TIDs of 7.5 CEM_{43} ($97 \pm 4\%$) compared to sham exposed spheroids. Thermocycler-heated spheroids showed no significant changes in their viability when exposed to TIDs in the range 0-120 CEM_{43}. Significant differences ($p < 0.05$) are seen when comparing the viability of HIFU-exposed spheroids with thermocycler-heating for TIDs of 30, 60 and 120 CEM_{43} (Figure 5.10 (b)).

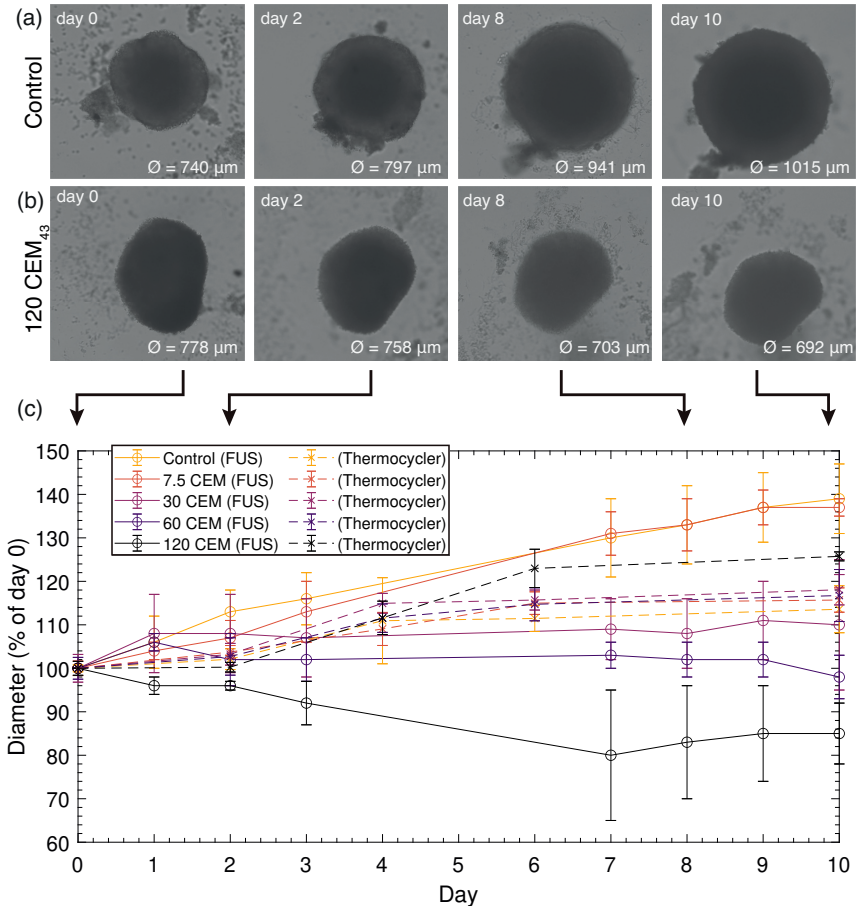

Figure 5.9: Images of a control spheroid (a) and a 120 CEM_{43} treated spheroid (b) on days 0 (day of treatment), 2, 8 and 10. (c) Growth curves for the control spheroids and those treated with ultrasound or thermocycler heating, as a % of their diameter on day 0. Results are presented as mean $\pm$ SD, and statistical significances (p-values) have been omitted for clarity

5.4 Discussion

Two different lens design strategies for achieving simultaneous iso-thermal ultrasound hyperthermia treatments of tumour spheroids in vitro have been compared. An acoustic (iso-pressure) strategy with a 3-focus holographic lens and an iso-thermal strategy with a 7-focus one. The 3-focus lens produced acoustic pressure peaks at the desired location, with similar peak pressures (differences less than 15%), which led to peak temperatures of 47.9 $\pm$ 0.8 °C, in the phantom material. Since differences in temperature greater

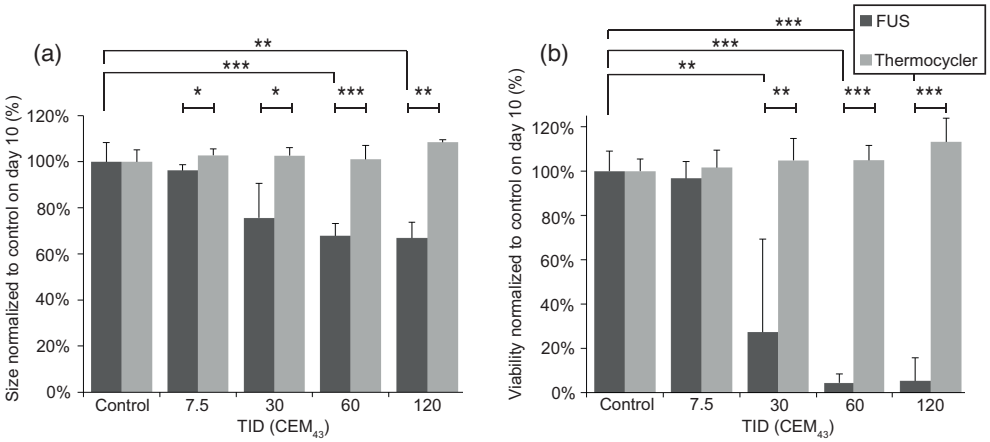

Figure 5.10: (a) Size and (b) viability study on day 10 after treatment for FUS and thermocycler- treated spheroids. Results are presented as mean ± SD and statistical significance is denoted with asterisk: (*) $p \leq 0.05$, (**), $p \leq 0.01$, (***), $p \leq 0.001$.

than ± 0.3 °C yield differences in TID of ± 20% [129, 130] it turned out not to be possible to design an appropriate lens with 3 foci based solely on acoustic modelling. In fact, readings over the three thermocouples showed that, after five minutes of exposure, each had received significantly different TIDs: 72.8, 114.3 and 40.5 CEM_{43}. Whilst this allowed simultaneous exposure of 3 spheroids, they did not receive similar TIDs.

Using the 7-focus lens, the acoustic profile was tuned to be more inhomogeneous than the iso-pressure case, with lower pressure in the central peaks than in the lateral ones (40% difference between the central peak and the external ones). However, this tuned acoustic field produced a more uniform TID in the targets. The thermal field from the 7-focus lens achieved a temperature of 46.37 ± 0.17 °C over the three thermocouples, with a TID of 58.2 ± 1.3 CEM_{43}, which represents a great improvement relative to the iso-pressure strategy where differences on TID received by the spheroids were of ± 37 CEM_{43}. This was successful because the central region cooled more slowly due to thermal conduction from the lateral foci, and therefore required a lower rate of energy deposition, as accounted for in the lens design. Unlike the iso-pressure lens, where the same pressure was set for the three foci resulting in a higher steady-state temperature at the central focus than in the other two.

Exposure of the tumour spheroids and evaluation of the TID they were receiving in real time, and ultimately stopping treatment when an intended dose was achieved worked well with the 7-focus lens. The newly designed spheroid holder which used an ultrasound absorbing (IEC) tissue mimicking gel with three wells and a separate lid which was tested

here, generally worked well. This system allowed the location of the spheroids within the wells to be known to better than $\pm$ 0.25 mm, relative to the thermocouple locations. The phantom with the lid maintained the heat and prevented spheroids exiting the well. Using this system it was possible to expose 3 spheroids simultaneously to ultrasound heating with the accuracy of temperature and thus TID monitoring demonstrated here. It was shown that ultrasound heating of the spheroids using TIDs of 30 to 120 CEM_{43} resulted in reduced spheroid growth, associated with lower metabolic activity (viability), compared to either sham exposed controls or thermocycler-heated spheroids. These results show that ultrasound heating improves tumour spheroid growth control compared to thermocycler heating and is suggestive of the contribution of non-thermal mechanisms to the anti-cancer effect of heat, such as cavitation, which locally enhances the heating rate in the exposed region [144, 145], acoustic radiation forces, which have been proven responsible for cell deformation [146], and even the generation of reactive oxygen species [147], which are responsible for reactions that reduce the viability of cells.

The main technical challenge was that spheroid retrieval from the wells using a pipette was difficult, resulting in the loss of 25% of spheroids after treatment, even after changing the gel colour from grey to pinkish/orange to improve the colour contrast with the white spheroids.

This system also has other limitations. The height of the pixels of the 3D-printed holographic lens will not be completely precise but will depend on the tolerance of the printer. Also, driving the transducer in continuous mode results in lens heating which can change its geometry and the polymer properties. On the other hand, regarding the exposure system, the phantom holder must be held rigidly in a fixed and reproducible position relative to the transducer-lens system and be removed and replaced when spheroids are changed. Another difficulty is the location of the fine-wire thermocouples just below and in the centre of the well, which needs to be done manually and gives an error on their exact location. The phantom gets degraded when pipetting spheroids in and out of the wells and when exposing it to ultrasound heating, so it needs to be changed quite often, ideally each time a new experiment is to be done. Also, spheroids need to be removed from their sterile environment for being exposed to ultrasound, even though all manipulation and system mounting is done in a sterile manner.

The expansion of the clinical applications of HIFU seen in recent years has resulted in an increase in the number of pre-clinical in vivo studies. This hologram-based system can contribute to a reduction in the use of research animals because it provides a reliable, inexpensive, and quick method of exposing appropriate tumour models to ultrasound heating thus providing an opportunity for the investigation of their biological and immunological responses. It is also amenable to studies investigating hyperthermia enhancement of radiotherapy.

Iso-thermal dose delivery systems are also of future interest for treating tumours in vivo with a uniform TID over the whole tumour volume. To design a holographic system for such conditions, a number of challenges need to be addressed. For example, in-vivo models are complex biological systems of different shapes, sizes, anatomical locations, and subjected to variable levels of blood perfusion. Although complicated, thermodynamic modelling is possible as shown by elegant studies performed by Kaczmarek et al. [148] who have used a range of blood perfusion rates to predict lesion sizes in a model of ultrasound-induced hyperthermia in the presence of magnetic nanoparticles. Also, it is possible to modify the tissue mimicking phantom used in this study to include an artificial blood vessel [149]. Hence, for future investigations our approach can be extended to generate a uniform 3D thermal pattern using a 3D distribution of virtual acoustic sources taking into account the expected heat-sinking effect caused by blood perfusion. For designing the optimal acoustic hologram, fast optimization techniques to tune the amplitude and phase of these acoustic sources will be required.

5.5 Chapter conclusions

Using a hologram designed to produce a 3-focus acoustic field with equal focal peak pressures, i.e., an iso-pressure design strategy, did not deliver simultaneous uniform TID to spheroids contained in 3 individual wells, because of the heat transport mechanisms, which are more efficient for the external targets than for the central one. The 15% maximum difference in peak pressure foci resulted in TID differences up to 63%. In order to achieve a similar TID within each well, an iso-thermal strategy was used to design holograms that produced multiple focus acoustic fields with different pressures at each focal peak, resulting in a uniform TID. Using this approach, differences of 40% in focal peak pressure were found, but TID with differences less than 4%, could be delivered. A case study was performed with U87-MG tumour spheroids to study their response to different TIDs with this last acoustic hologram. Biological response showed greater anti-cancer effects for ultrasound-mediated heating than for thermocycler heating, suggesting that our system provides a reasonably high throughput platform for investigating the biological responses of tumour spheroids in vitro to ultrasound hyperthermia. These results show that holographic lenses designed to deliver iso-thermal doses coupled to single-element HIFU transducers can provide simultaneous uniform TIDs in complex targets or over relatively wide regions, using a low-cost but robust system. Further work could be carried out to optimize thermal uniformity in different complex 2D or even 3D targets, by, for example, applying optimization and machine learning algorithms [83] to accurately engineer the acoustic wavefront and produce uniform thermal patterns for ultrasound hyperthermia systems.

Publications

Results related with this Chapter have been presented in the following publications:

Journal papers

Andrés, D., Rivens, I., Mouratidis, P., Jiménez, N., Camarena, F., & Ter Haar, G. (2023). Holographic Focused Ultrasound Hyperthermia System for Uniform Simultaneous Thermal Exposure of Multiple Tumor Spheroids. Cancers, 15(9), 2540.

This paper was highlighted in an article published by the Focused Ultrasound Foundation (URL: https://www.fusfoundation.org/posts/a-new-focused-ultrasound-system-for-treating-multi-focal-cancer/)

Conference papers

Andrés, D., Rivens, I., Mouratidis, P., Jiménez, N., Camarena, F., & Ter Haar, G. Acoustic Holograms for Homogeneous Hyperthermia Over Several Tumor Spheroids. *2023 IEEE International Ultrasonics Symposium (IUS)*. Montreal, Canada. September 3-8, 2023. Published by IEEE Institute of Electrical and Electronic Engineers (ISBN: 979-8-3503-4645-9) in November 2023.

Rivens, I., Mouratidis, P., **Andrés, D.**, Symonds-Tayler, R., N., Jiménez, N., Camarena, F., & Ter Haar, G. An in vitro system for focused ultrasound hyperthermia (and radiotherapy) studies using spheroids. *34th Annual Meeting of the European Society for Hyperthermic Oncology*. Gothenburg, Sweden. September 14-17, 2022.

Chapter 6

Ultrasound targeting through the temporal window using holograms

Acoustic holograms can encode complex wavefronts to compensate the aberrations of a therapeutical ultrasound beam propagating through heterogeneous tissues such as the skull and, simultaneously, they can generate diffraction-limited acoustic images, i.e., arbitrary shaped focal spots. In this Chapter, we numerically study the performance of acoustic holograms focusing at the thalamic nuclei when the transducer is located at the temporal bone window, which is a thin and accessible area of the skull. However, when targeting from this area the bilateral thalamic nuclei are not aligned with the elongated focal spots of conventional focused transducers and, in addition, skull aberrations can distort the focal spot. We found that using patient-specific holographic lenses, the focal spot can be sharply adapted to the thalamic nuclei in a bilateral way while skull aberrations are mitigated, even targeting from this small region of the human head. Furthermore, the performance of these holograms was studied under misalignment errors between the source and the skull, concluding that for misalignments up to 5 degrees acoustic images are correctly restored. Finally, a thermal study was conducted to simulate bone heating. This work paves the way to design clinical applications of transcranial ultrasound such as blood-brain barrier opening for drug delivery or deep-brain neuromodulation using this low-cost and personalized technology, presenting desirable aspects for long-term treatments because the patient head does not need to be shaved completely and skull heating is low.

6.1 Introduction

Transcranial focused ultrasound have become an emerging technique with great potential for treating brain diseases in a non-invasive and non-ionizing way. Ultrasound waves can penetrate the skull bones and produce thermal and mechanical effects in the brain tissue [150]. These kind of interactions are the base of several treatments that are being developed in the recent years, ranging from thermal ablation, where ultrasound absorption results in a localized temperature rise producing cell necrosis [151], to hyperthermia, where ultrasound induces a mild temperature rise to enhance chemotherapy or radiation therapy [50]. In addition, using high amplitude and short pulses, ultrasound histotripsy can enable cavitation of bubble clouds to generate sharp lesions at the targeted region using mechanical effects [152]. At lower intensities, it also has been widely proven that focused ultrasound can disrupt the blood-brain barrier in a localized, safe and reversible way [153, 154], enabling localized drug-delivery applications in the central nervous system. In addition, at lower acoustic intensities the mechanical interaction of the waves can produce neuromodulation effects at different parts of the brain [155].

However, the presence of the skull bones between the ultrasonic source and the target region of the brain is a major obstacle to the application of focused ultrasound in the brain. This wall of high stiffness and density protects the brain from mechanical loads, including mechanical waves such as ultrasound. Its high acoustic impedance and complex poroelastic and layered internal structure produces strong scattering, refraction and attenuation effects to the propagating acoustic waves. This results in beam aberrations and poor focusing. Several systems have been proposed to overcome these drawbacks and take control of the acoustic focus, its location, size and shape. Using a minimally invasive approach, intracranial ultrasound implants can be placed inside the skull to directly sonicate brain tissues avoiding phase aberrations [156]. This technique requires craniotomy, therefore, it is suitable after surgical resection of a tumour, i.e., a glioblastoma, to open the blood-brain barrier for delivering postoperative chemotherapeutic agents. Fully non-invasive techniques are desirable, such as MR-guided phased-array systems, which control the delay and amplitude of the vibration of each individual piezoelectric transducer to electronically steer the focal spot, and mitigate the aberrations produced by the skull [48]. However, as these therapeutical sources require a wide aperture and the number of active transducers of state-of-the-art phased-arrays is on the order of 1024/2048 elements, this approach results in large piezoelectric elements. In this way, the focal steering capabilities are limited by the emergence of diffraction grating lobes because active elements are separated more than half a wavelength. This novel technology stands out for its complexity and high cost, which makes it unattainable for many health and research centres. One approach to avoid MRI-guided systems is to use stereoscopic image-guided single-element transducers, and use simulations to select the optimal transducer location to minimize beam aberrations [33]. Recent approaches include conformal helmet

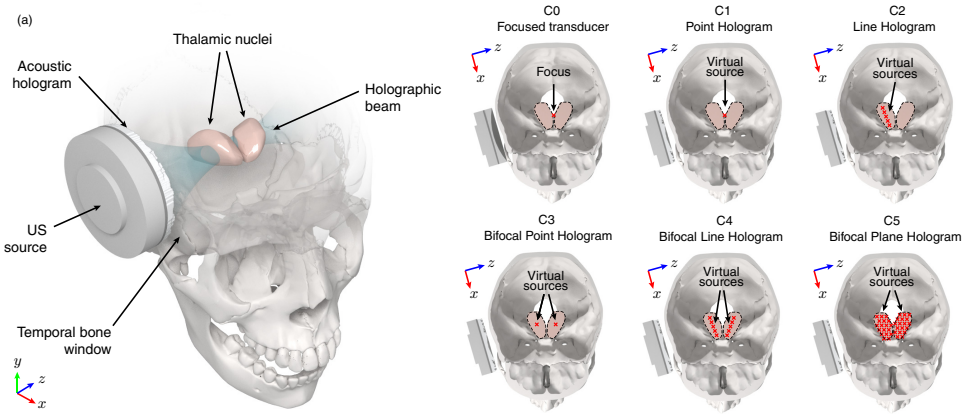

Figure 6.1: (a) Scheme of the proposed device, an acoustic hologram is coupled to a flat circular ultrasound source and located at the temporal bone window targeting the deep-brain nuclei. Several configurations are studied, a reference focused transducer (configuration C0), a point hologram targeting at the central point of the thalamic nuclei (C1), a line hologram targeting at the centre of the targets (C2), a bifocal point hologram targeting at each nucleus (C3), a bifocal line hologram targeting at each nucleus (C4), and a bifocal plane hologram targeting at each nucleus (C5).

scaffolds, composed of a patient-specific 3D-printed helmet designed to hold reusable phased-array transducer modules. These systems enable near-normal incidence of multiple phased array modules, where the position of each transducer is determined by the location of the therapeutical target [157].

Recently, in response to the need of low-cost and non-invasive ultrasonic focusing systems, 3D-printed acoustic lenses [61] and acoustic holograms [63] have been proposed. On the one hand, using refractive 3D printed lenses, aberrations introduced by the skull can be compensated recovering the single focal spot of a focused transducer. When focusing in a single spot, the focal point reconstructed by a 3D-printed lens can even be steered by mechanically moving the source [62]. On the other hand, acoustic holograms can go beyond, reconstructing sharp and complex acoustic images inside the brain [63]. Acoustic holograms, first proposed for homogeneous media [51], can generate focal spots whose shape and size can be controlled and modified to target a specific structure at the central nervous system [63]. Recently, this technique has been tested ex-vivo using human skulls [64] and validated in-vivo for blood-brain barrier opening in mice [65].

Skull heating is a main concern when performing transcranial ultrasonic therapy and it has been observed to be critical at thicker parts of the human skull, in particular at high

ultrasound frequencies, above 1 MHz [158, 159]. When using single-element transducers to tackle deep-brain nuclei, the elongated focal spot must be aligned with the therapeutical target and a normal incidence is required to minimize beam refraction. This usually results in better targeting through the occipital and parietal bones [160]. However, the bone at the trans-temporal window is thinner and more uniform. Indeed, this location is usually selected for brain imaging [161]. The thinness of this layer produces fewer aberrations and lower skull heating, therefore, it is desirable for transcranial ultrasound therapy. In addition, only a small amount of hair needs to be shaved, which might be a common concern for patients, particularly during long-term treatments. One deep-brain target of main interest is the thalamus, a bilateral structure involved in many processes such as consciousness, sleep cycle, integration of sensory data and supporting motor and language systems [162]. Recent studies performed thalamic neuromodulation in humans using single-element transducers [163], with evidences of inhibiting effects [164]. Evidences of recovery from coma in a patient by the direct neuromodulation of this deep brain nuclei has been reported [165]. However, when targeting the thalamic nuclei through the temporal window using a single-element focused transducer, the therapeutic target is not completely aligned with the elongated focal spot of the ultrasound source.

In this Chapter, we numerically study acoustic holograms to target the thalamic nuclei in humans through the trans-temporal window. Using acoustic holograms coupled to a flat transducer, as sketched in Fig. 6.1, the skull aberrations can be compensated and, simultaneously, the shape of the focal spot and its location can be adapted to bilaterally target the thalamic nuclei. Five different strategies to design the holograms are presented and their performance is compared to a reference focused transducer. As we will show, holograms allow using the trans-temporal window to accurately focus acoustic energy at the thalamic nuclei. In addition, note that, while the control of the physical location of the system can be performed using mechanical or optical methods [166], these systems will introduce some degree of uncertainty in the positioning. Therefore, we study aberrations introduced by the misplacement of the source, evaluating the robustness of the resulting field against misalignments. We have studied how the use of acoustic holograms through the temporal bone window results in a lower temperature increase as compared to other thicker skull bones, such as the parietal or frontal bones. Finally, the performance of holograms on different subjects using the same lens for different patients, and patient-specific lenses was studied.

6.2 Materials and Methods

We use a flat circular transducer with an aperture of $2a = 65$ mm. It is located at the temporal bone window, at a distance of 15 mm from the skin to allow for the inclusion of a holographic lens (see Fig. 6.1). A second transducer with similar characteristics to those used for thalamic focusing through the temporal bone window [165] is used. It is a spherically focused transducer with a radius of curvature of $F = 80$ mm and same aperture as the first one (f-number$= 1.23$), also located at the temporal bone window at a distance of 13 mm from the skin. The focused transducer is aligned to focus at the centre in between both thalamic nuclei, in the middle of the thalamus, as represented in Fig. 6.1, configuration C0. Both sources are excited with a 650-kHz sinusoidal signal.

To design the hologram we use a time-reversal simulation method, following the procedure described in [63]. The tomographic image of the skull used in this study was acquired using a GE LightSpeed VCT 64 scanner (GE Medical Systems, Milwaukee, WI) from an anonymous patient using a resolution of 0.488 mm and slice resolution of 0.625 mm. To introduce the skull in the numerical simulations and match the numerical grid, it has been interpolated with an isotropic resolution of 0.39 mm, which corresponds to $\lambda/6$ at the transducer frequency. The CT linear x-ray attenuation data, in Hounsfield units, is converted to density and sound speed maps using empirical linear relationships [79, 80]. Values of mean and maximum sound speed and density at the skull are the following: $c_{\mathrm{mean}} = 2332.6$ m/s, $c_{\mathrm{max}} = 3100$ m/s, $\rho_{\mathrm{mean}} = 1611.3$ kg/m^3, $\rho_{\mathrm{max}} = 2190$ kg/m^3. Acoustic attenuation of the skull has been set constant, since it has been proved that a variation in this value along the skull weakly affects the acoustic transmission [167], and its value was set to 8.371 dB/(cm·MHz$^\gamma$), according to bibliography [81], using $\gamma = 1.1$. Brain tissue has also been considered in the studies, defining it as the whole interior volume of the skull, and with properties of density, speed of sound and acoustic absorption of 1000 kg/m^3, 1560 m/s and 0.659 dB/(cm·MHz$^\gamma$), respectively. Both the skull and the transducer are surrounded by water, with density of 1000 kg/m^3, sound speed of 1522 m/s and absorption of 0.0009 dB/(cm·MHz^2).

The selected therapeutic target of this study is the thalamus. The location and shape of this structure has been extracted from the human atlas published online and open-access by the International Consortium for Brain Mapping (ICBM) template from the Laboratory of Neuro Imaging [168]. The volume and shape of the brain has also been extracted from the same MRI image. Since the segmented MRI data does not correspond to the skull in the CT image, rotations and linear homothetic transformations have been performed until the brain extracted from the MRI fits into the cranial cavity, in order to ensure the correct location of the thalamus inside the skull model. The volume of both thalami is 7.9 cm^3 and the volume of the brain is 1523 cm^3.

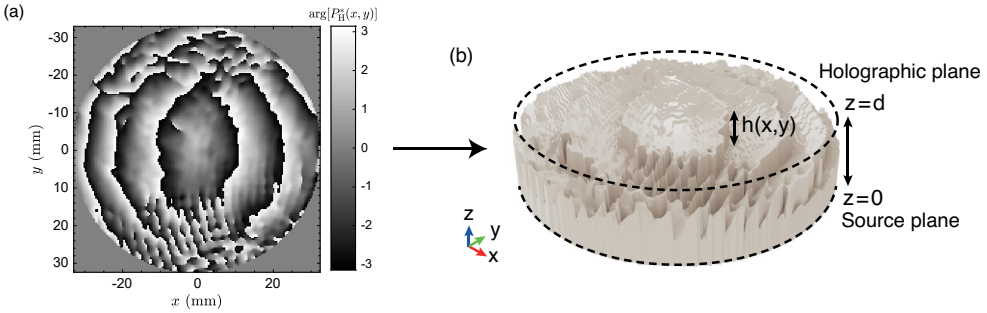

Figure 6.2: (a) Phase of the field after phase-conjugation recorded at the holographic surface for the single line hologram configuration (C2). (b) Rendering of the corresponding hologram showing the holographic plane at $z = d$. The flat circular source is located at the bottom of the lens.

Numerical simulations were performed using a pseudo-spectral time-domain method in the k-space, implemented in the open-source k-Wave software [117]. In the case of the reference focused transducer (configuration C0), the acoustic field is obtained directly by propagating the converging wavefront generated by the source. In the case of the holograms, several configurations are studied, a point hologram targeting the central point of the thalamic nuclei (configuration C1), a line hologram targeting the centre of the targets (configuration C2), a bifocal point hologram targeting each nucleus (configuration C3), a bifocal line hologram targeting each nucleus (configuration C4), and a bifocal plane hologram targeting each nucleus (configuration C5), as shown in Fig. 6.1. To design the holograms, a time-reversal procedure is performed. First, a set of virtual acoustic monopole sources are located at the target, each set according to the corresponding configuration. Then, in a first simulation, the resulting field radiated by the virtual sources is recorded at a holographic surface in the $x - y$ plane, $P_{\mathrm{H}}(x, y)$, located at a distance $z = d$ from the source (see Fig. 6.2). The temporal inversion is performed by complex-conjugating the recorded pressure field at the holographic plane, resulting in a field $P^*_{\mathrm{H}}(x, y)$.

Then, the holographic surface is divided into squared pixels of 0.39×0.39 mm^2, equal to the resolution of the simulation grid, each pixel corresponding with a pixel of the holographic lens (see Fig. 6.2). Each pixel of the lens presents a different height, as described in Chapter 2, and vibrate longitudinally like an elastic Fabry-Perot resonator given by the Eq. (2.3).

Once the height function is found, holograms can be constructed, resulting in surfaces with a total of 22,129 pixels and a maximum height of 10.8 mm. Note each of them acts as a phased-array emitter, allowing an accurate control of the phase profile. In this way, the compensation of the aberrant effects of the skull and the time-reversal focusing

towards the positions of the original virtual sources are simultaneously encoded on the high-density pixel hologram. Phase-conjugated profiles and 3D models of the lenses for each configuration are shown in Figure 6.3.

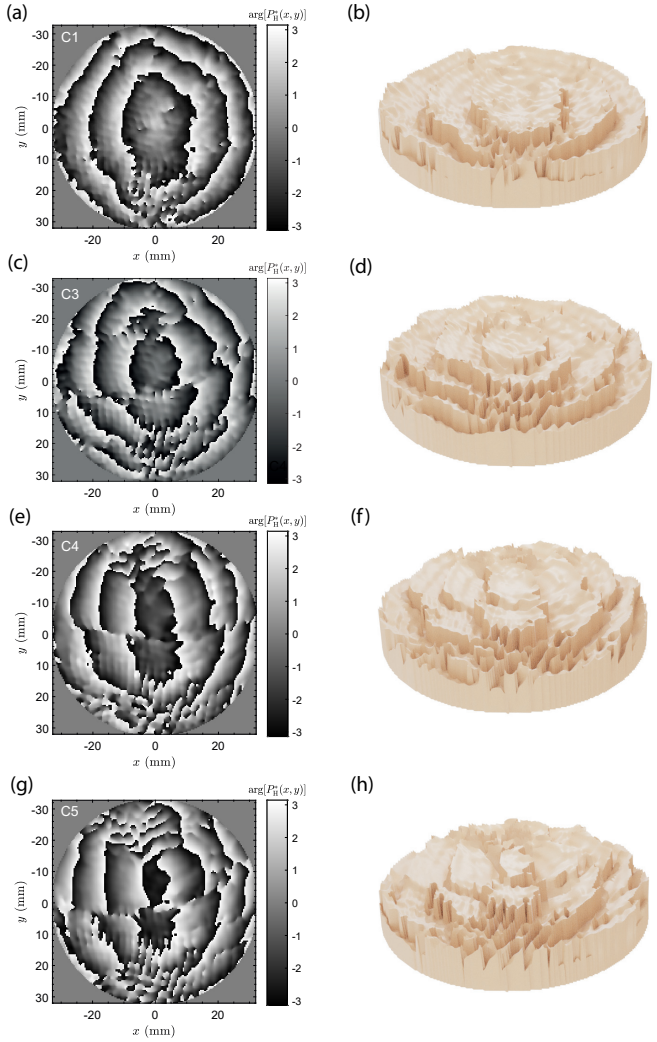

Figure 6.3: Phase of the field after phase-conjugation recorded at the holographic surface for (a) configuration C1, (c) configuration C3, (e) configuration C4 and (g) configuration C5. Rendering of the corresponding holographic lens for 3D-printing for (b) configuration C1, (d) configuration C3, (f) configuration C4 and (h) configuration C5.

Finally, a simulation was carried out to retrieve the acoustic field produced by the holograms. All designed lenses use the material properties corresponding to Clear resin (Formlabs), a photopolymer used for 3D printing. The speed of sound and acoustic absorption of this material has been experimentally measured with pulse-eco techniques in cylindrical samples of different height, while the density has been calculated knowing the dimensions of each cylinder and its mass. These experiments resulted in $\rho_L = 1170.8$ kg/m^3, $c_L = 2580.1$ m/s and $\alpha_L = 2.871$ dB/(cm·MHz). These values match those reported for similar materials [51, 63, 64]. In all simulations the source was driven with a 100-cycles sinusoidal tone burst of 650 kHz frequency and 1 Pa amplitude at the surface of the source. Each simulation was running during 300 μs so the pulsed burst could cross the medium twice. This time was considered for both backward and forward propagation simulations, so that multiple internal reflections of the acoustic wave in the skull can be encoded by the hologram.

To study the robustness of ultrasound holograms under small deviations between the acoustic lens and the skull, several parameters have been studied under rotations and displacements of the lens: maximum pressure gain at the focus position, total focus volume, sonicated target volume, and out-of-target sonicated volume. Normalized peak pressure is calculated as the pressure gain relative to the pressure at the transducer surface and to half the average pressure at the exit of the holographic lens for the focused transducer and holograms, respectively. Volumes are calculated as the region with a pressure gain between the maximum and -3 dB for each focus separately. Performances under rotations of 1.25° from 0° to 17.5° and under translations of 1 mm from 1 mm to 8 mm in the y-axis have been studied for the focused transducer and C2, C3 and C4 configurations.

The skull heating rate was used as a figure of merit to quantify the capacity of acoustic beam to rise the temperature of the skull. We have first calculated the acoustic pressure field in the steady state. The particle velocity vector, assuming a harmonic wave, is calculated as $v_i = 1/(i\omega\rho)\partial p/\partial x_i$, with $i = x, y, z$, and period-averaged acoustic intensity is calculated as $\mathbf{I} = \mathrm{Re}(p\mathbf{v}^*)/2$, where $(\cdot)^*$ denotes complex conjugation. Then, the total heating rate in a given volume is

$$W_Q = \int_V Q \cdot dV, \tag{6.1}$$

where $Q = 2\alpha I$ is the heating rate per unit volume, being α the medium attenuation value and I the magnitude of the acoustic intensity. Also the heating rate was evaluated in terms of temperature rise in time like

$$\frac{\Delta T}{\Delta t} = \frac{Q}{C\rho d}, \tag{6.2}$$

where ΔT is the rise of temperature in the interval of time Δt, C = 1440 J/kg K is the skull heat capacity and d is the skull thickness.

Finally, additional simulations were carried out on different subjects to study the performance of the same lens on different patients. The simulation study for the C1 configuration was repeated for three different anonymous patients (subjects #2-#4), targeting the same region from the right temporal bone. For each additional subject, two calculations were performed. First, a lens was created ad-hoc for each patient. Remark that the target segmentation for the subject #1 was used for subjects #2-#4, but we considered the new skull anatomy, inner structure and acoustical properties. Second, the lens created for the subject #1 was used for subjects #2-#4.

6.3 Results

6.3.1 Focused ultrasound transducer

We start showing the results for the reference focused transducer, summarized in Fig. 6.4. This source was first simulated in homogeneous media (water) and, then, including the human head. Fig.6.4 (a) shows a 3D rendering, by using a maximum intensity projection method, of the magnitude of the acoustic field for the transcranial propagation through the temporal bone window. It can be visually identified that the focused beam presents strong aberrations. A detailed picture is shown in the sagittal and coronal sections in Fig. 6.4 (b, c), respectively. Note that the transducer was located carefully to grant normal incidence and the cartesian axis are aligned to the transducer axis, so the images does not exactly correspond to anatomical sagittal and coronal sections. While the energy roughly focuses around the geometrical focus of the transducer, which has been located in the centre of the thalamus (configuration C0), the ultrasound beam covers several areas outside the target, see Fig. 6.4 (c). In fact, the maximum sound pressure inside the brain does not correspond to the maximum in the main focal spot, but to a secondary lobe. A high amount of energy is focused at the prefocal zone, outside the target. A total of 0.28 cm^3 of both thalami is sonicated with a pressure higher than -3 dB the peak pressure, which represents a 3.6% of the total thalamic volume, while 1.208 cm^3 have been sonicated outside the therapeutic target, which is a 0.08% of the total brain volume, including the thalamus.

Fig. 6.4 (d-f) show the normalized cross-section of the maximum pressure field in the z, y and x directions for the focused transducer considering the human tissues, and the corresponding field in water. It can be observed that the elongated focal spot does not accurately fit the target, shown by dashed lines. Maximum focal pressure gain in

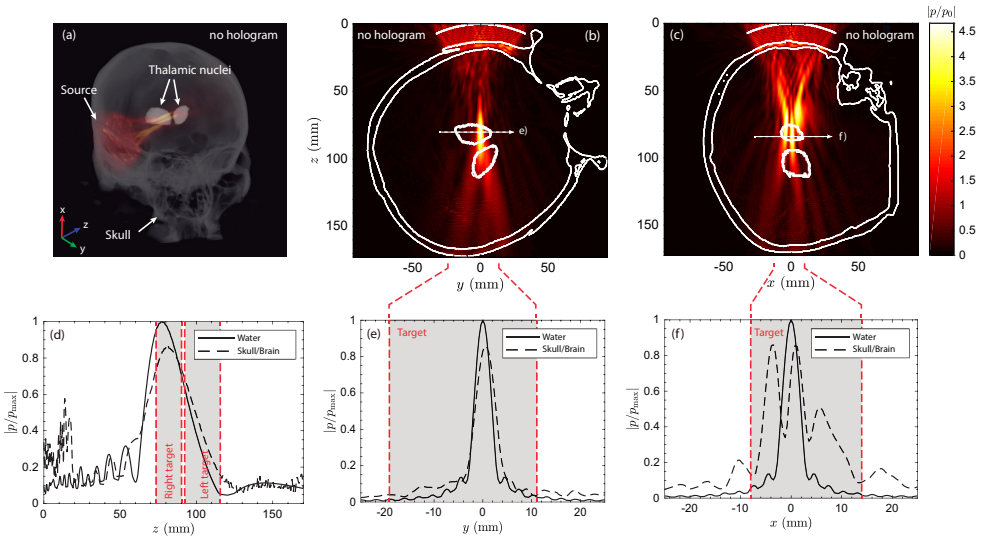

Figure 6.4: (a) 3D view of the studied configuration using the focused source (C0). Maximum intensity projection of the CT data (grey colormap), segmented thalamic nuclei (white areas) and maximum intensity projection of the acoustic field (red colormap). (b) Cross-section of the acoustic field in the x-z plane (quasi-axial) and (c) in the x-z plane (quasi-sagittal) cut, colormaps normalized to p_0. (d) Normalized peak pressure in water and through the skull along the z-axis, (e) along x-axis and (f) along y-axis.

water for this transducer is 17.8 p/p_0, whereas when considering the skull and the brain is 4.7 p/p_0, where p_0 is the pressure at the transducer surface, so the skull and brain tissues introduce a loss in pressure gain of 5.8 dB, according to these results. In the axial direction, Fig. 6.4 (d), the depth-of-field of the focused transducer including the skull (36.5 mm) is longer that dimensions of the right half of the thalamus (13.2 mm) and therefore acoustic energy is also focused at the 3rd ventricle in the midline between the two halves of the thalamus. In the lateral direction, the full-width at half-maximum of the beam (4.25 mm in the y and 8.1 mm in the x-direction) is narrower than the target (16.8 mm and 26.2 mm, respectively). Aberrations introduced by the skull become more evident in Fig. 6.4 (f), where multiple lateral lobes appear. The defocusing effect produced by the skull usually increases the sonicated volume inside the target (1.48 cm^3 in this simulation compared to 0.43 cm^3 obtained with the focused source in water), which could be considered positive. However, it is an uncontrollable phenomenon that also increases the sonication in out-of-target regions (1.19 cm^3 in this simulation).

6.3.2 *Holograms for skull aberration correction*

With the aim of correcting skull defocusing, a single virtual source was set in the centre of both thalami, located at $(0, 0, 101)$ mm in cartesian coordinates, corresponding to the configuration C1 shown in Fig. 6.1. The acoustic field produced by this hologram is shown in Fig. 6.5 (b, d). It can be seen that the focal zone is similar to that of the focused transducer including the skull, see Fig. 6.5 (f), but lateral lobes due to defocusing and aberrations are not present. The lens corrects beam aberrations producing an ultrasonic field equivalent to that of a focused source in homogeneous media. The acoustic image of a single virtual source (C1) is a diffraction-limited focal spot, whose full-width at half-maximum is 5.2 mm, as compared with 3.9 mm of the focused source in water. In this way, while this configuration corrects aberrations, the width of the beam is still narrower than the selected therapeutical target.

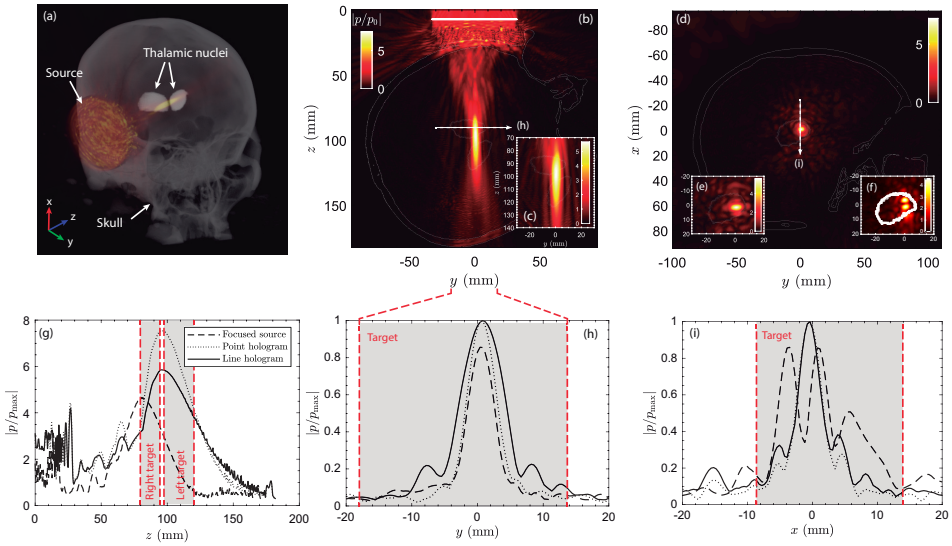

Figure 6.5: (a) 3D scheme of the line hologram acoustic field. (b) Coronal cut of the point hologram (C1 configuration) and (c) line hologram (C2 configuration). d)Axial cut for the left thalamus of the point hologram, (e) line hologram and (f) focused transducer. (g) lineal cut along the z-axis at the maximum pressure point for the focused transducer, point hologram and lineal hologram. (h) Normalized pressure comparison in a cut along the y-axis. i) Normalized pressure comparison in a cut along the x-axis

To laterally magnify the focus in one dimension in order to cover a greater volume of the thalamic nuclei, 22 virtual sources have been located in a line along the midline of the thalamic nuclei, in the x-y plane, see configuration C2 in Fig. 6.1. A 3D rendering of this configuration and the resulting field is shown in Fig. 6.5 (a). The resulting field produced by the C2 hologram is shown in Fig. 6.5 (c, e) in the z-y and x-y planes, respectively.

Using this hologram, the focal spot widens in the lateral dimension while the aberrations introduced by the skull are still compensated.

Both holograms are compared with the acoustic field of the focused transducer in Fig. 6.5 (g-i). In the axial direction, the elongated focal spot of holograms C1 and C2 is 41.7 mm and 52 mm, respectively, as compared with 37 mm of the focused source. As shown in Fig. 6.5 (g), the axial field does not accurately match the target region. However, note neither C1 nor C2 were designed to control the beam in the z-direction. In the transverse directions, (Fig. 6.5 (h-i)) secondary lobes of the focused transducer are controlled in both transverse directions, y and x. In the y direction, the C2 hologram widens the beam-width to 7.8 mm (50% larger than the single-virtual source hologram, see Fig. 6.5 (i)). However, as virtual sources were only arranged over a line in the y direction, the beam is not enlarged in the x direction, see Fig. 6.5 (i).

For the single-virtual source hologram, the amplitude of the pressure at the focal spot is 7.6 p/p_0, where p_0 is defined as half the average pressure at the exit plane of the holographic lens for all the studied holograms. We use this reference because at the exit of the lens the total pressure is the superposition of radiated waves and reflected waves by the skull, see Fig. 6.5 (b). The increase in amplitude, compared to the focused source case ($p/p_0 = 4.7$) is due to the correction of the aberrations, what results in a sharper focusing.

In addition, using multiple virtual sources as in configuration C2, maximum pressure at the focus is increased to 5.9 p/p_0. Note that this configuration produces a defocused beam of controlled width without aberrations. As compared with the focused transducer including the skull, the increase in pressure amplitude at the focal spot is 2.1 dB and 0.9 dB for configurations C1 and C2, respectively. Point (C1) and line (C2) holograms sonicate 5.2% (0.41 cm^3) and 8.5% (0.68 cm^3) of the total thalamic volume, respectively, compared to 3.6% (0.28 cm^3) sonicated with the focused source while the sonicated volume outside the target is 0.19 cm^3 (0.013%) and 0.77 cm^3 (0.05%), respectively, compared to 1.2 cm^3 (0.08%) with the focused source.

Using the focused transducer, the ratio between sonicated thalamic and brain volumes is 0.23. Using the C1 configuration it is 2.16, and using the C2 it becomes 0.88. The thalamic-to-brain sonicated volume ratio is 9.4 and 3.8 times better while using point and line holograms, respectively.

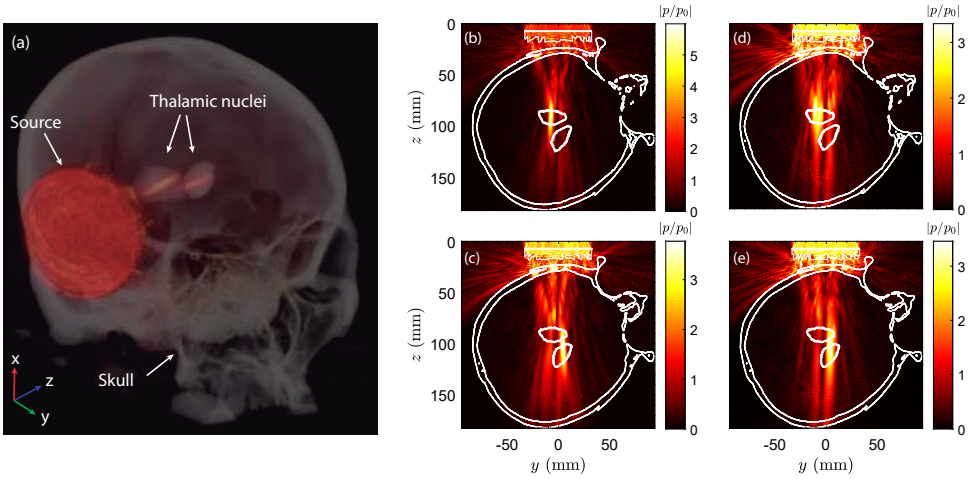

Figure 6.6: (a) 3D representation of bifocal sonication with hologram. Cut for (b) left and (c) right thalamus point hologram. Cut for (d) left and (e) right thalamus plane hologram.

6.3.3 Holograms for bifocal targeting

While the previous acoustic holograms can mitigate the skull aberrations and increase the target sonicated volume, further focusing improvements could be made to sonicate bilateral structures at the deep brain. Configurations using several sets of virtual sources distributed along the bilateral nuclei of the thalamus, as shown in Fig. 6.1, are presented in this section.

First, a pair of virtual sources have been located at each part of the thalamus, as shown in configuration C3 in Fig. 6.1. As we are sonicating through the trans-temporal bone window, both structures appear to be almost in the same line respect to the transducer. To individually treat them and optimise the target-brain sonication ratio, both sources have been steered in the x-axis, as represented in Fig. 6.6 (a-c). With this configuration 4.5% of the target structure has been treated (0.36 cm^3), while only 0.45 cm^3 of the brain is affected, which represents a 0.03% of the brain volume. Pressure gains at the focal points arrives at 5.84 p/p_0 and 3.7 p/p_0 at right and left thalami, respectively. The ratio between sonicated thalamic and brain volumes with this configuration is 0.79.

To further improve this results, a bifocal wide hologram has been created by locating virtual sources in two lines at different heights of the deep brain structures, which is represented in the configuration C4. In this case we get to treat 1.36 cm^3 of both thalami (17.1%) in just one sonication. The sonicated volume outside the target is 4.94 cm^3 (0.32%), greater than in the other studied systems, and the pressure gain is 3.9 p/p_0 and

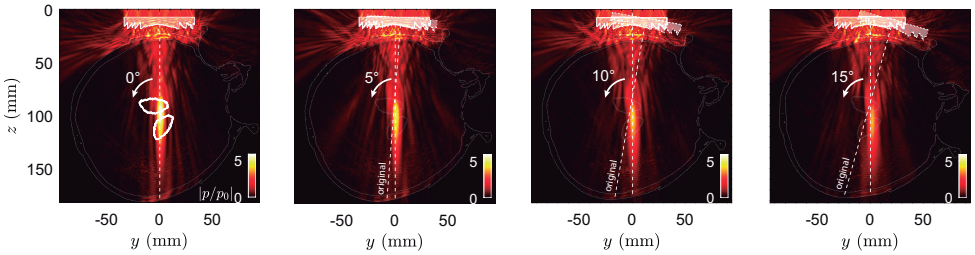

Figure 6.7: Example of how a misalignment between the source and the target impacts on the focusing performance of the hologram. In this example (configuration C2), a rotation with respect to the central point of the thalamic nuclei is shown.

3.4 p/p_0 at right and left thalami, respectively. The thalamic-to-brain sonicated volume ratio with this configuration is 0.28.

A last hologram has been made by locating two planes of virtual sources at the same x position as in the two points hologram and following the configuration C5. The resulting acoustic field is represented in Fig. 6.6(d, e). We treat 1.21 cm^3 (15.3%) of the thalamus and we sonicate 5.84 cm^3 (0.38%) of the brain, with a pressure gain of 3.4 p/p_0 and 3.3 p/p_0 at left and right thalami, respectively. In this case, ratio between sonicated thalamic and brain volumes is 0.21. Comparison between each studied case is shown in Table 6.1.

		Target volume (cm^3, %)	Out-of-target volume (cm^3, %)	Volume ratio (a.u.)	Max. pressure (p/p_0)
C0	Focused transducer	0.28 (3.6%)	1.21 (0.08%)	0.23	4.7
C1	Point hologram	0.41 (5.2%)	0.19 (0.013%)	2.16	7.6
C2	Line hologram	0.68 (8.5%)	0.77 (0.05%)	0.88	5.9
C3	Bifocal point hologram	0.36 (4.5%)	0.45 (0.03%)	0.79	5.8
C4	Bifocal line hologram	1.36 (17.1%)	4.94 (0.32%)	0.28	3.9
C5	Bifocal plane hologram	1.21 (15.3%)	5.84 (0.38%)	0.21	3.4

Table 6.1: Summary of thalamus and brain volume sonicated in each case. Values of percentages are referred to total thalamus volume (target volume column); and to total brain volume, including thalami (out-of-target volume column). Volume ratio measures the ratio between treated volume and untreated volume.

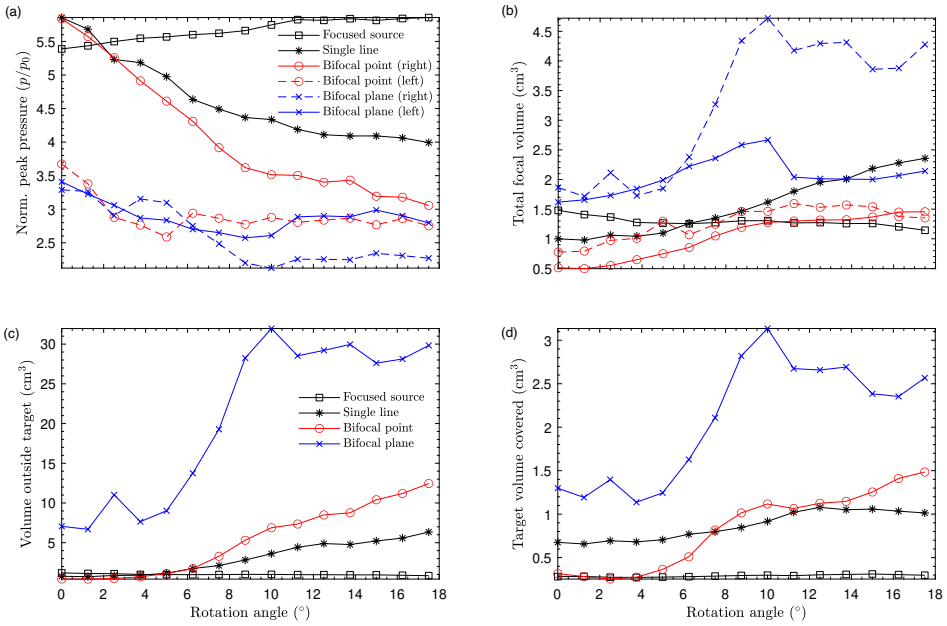

Figure 6.8: Parametric study of the focusing performance as a function of a rotational misalignment. (a) Maximum pressure at focus, normalized. (b) Focal volume. (c) Out-of-target volume. (d) In-target volume.

6.3.4 Robustness against misalignment

To evaluate the robustness of our proposal, we have studied the accuracy of ultrasound holograms inside the brain when rotation and translation errors are made, as described in the *Materials and Methods* section. In Fig. 6.7 we can observe an example of the pressure field degradation under a progressive rotation for the line hologram (C2). Pressure scale is normalized to the maximum at 0° rotation. The focal quality parameters of the parametric study are shown in Fig. 6.8 and 6.9. Figure 6.8 summarizes the focusing performance as a function of a rotational misalignment, while in Fig. 6.9 we summarize it as a function of a lateral linear translation.

For the focused transducer, its focus quality does not change under rotation from the centre of the skull. The main change in sonicated volumes and peak pressures is due to the secondary lobes that appear due to the aberrations introduced by the skull. The maximum change in pressure values is 8% of the original pressure gain, and sonicated volumes of the brain and both thalami remain almost constant. As the angle of incidence of the focused sound waves is always normal to the skull, the skull-transducer relative

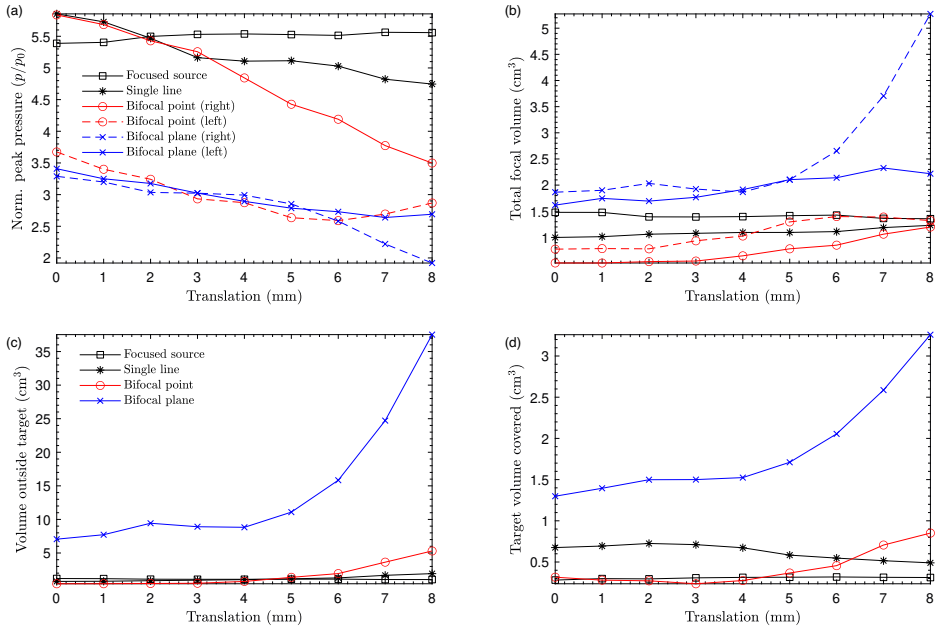

Figure 6.9: Parametric study of the focusing performance as a function of a lateral linear translation. (a) Maximum pressure at focus, normalized. (b) Focal volume. (c) Out-of-target volume. (d) In-target volume.

location does not affect the focus shape. Similar results are obtained while the skull is horizontally translated from its original location, with a maximum change of pressure gain at the focus of 3% (see Fig. 6.8 (a) and Fig. 6.9 (a)).

For the line hologram, the maximum pressure decreases with the rotated angle and treated volumes increase, which means that the hologram loses resolution when it is not correctly positioned. At 17.5° of rotation, the acoustic pressure at the focus is reduced by 32 % of the original value and the volume outside the target is 8.3 times greater. Also the target volume covered is increased 1.5 times compared to the original location. For rotation angles below 5° both volumes outside and inside the target remain almost constant (below 10% of increase) while the difference of pressure gain is 15%. In terms of translation error, the same behaviour in pressure values is observed for translation errors up to 6 mm (Fig. 6.8 (a) and Fig. 6.9 (a)).

In the case of the C3 configuration, the right focus, which is mainly laterally steered in the y-axis, shows more pressure amplitude and has a more delimited shape than the left one, which was steered also in the x-axis. When rotating 5° the lens around the skull

Table 6.2: Maximum pressure at focus related to transducer surface pressure (p/p_0) for different steering angles

	Steering angle				
Hologram	0°	2°	5°	10°	15°
Line	3.02	2.80	2.57	2.16	2.03
Point-left	3.12	2.94	2.43	1.77	1.47
Point-right	1.96	1.68	1.36	1.43	1.31

the loss in pressure at the right focus is 21%, while for 17.5° this loss arrives at 48%. A similar loss of 24% is obtained with a translation misalignment of 5 mm, arriving at 40% at 8 mm. If we study the left focus, for 5° we observe a pressure loss of 29% while for 17.5° the amplitude reduction is 24%. A similar value is obtained with a translation misalignment of 6 mm (24%), while at 8 mm the loss is 22% (see Fig. 6.8 (a) and Fig. 6.9 (a)). Target volume sonicated by both focus with this configuration is 0.32 cm^3 at the original location, increasing to 0.36 cm^3 for a rotation of 5°. A similar value is observed for a translation error of 5 mm, and the volume is increased to 1.48 cm^3 when the rotation is 17.5°, which is almost 5 times greater than in the original location. At the maximum translation error studied (8 mm), the target sonicated volume is 3 times greater. This is caused by the defocusing of the beam, which spreads the energy covering more volume of the thalamic nuclei. Nevertheless, sonicated brain volume outside the target follows the same tendency: at 5° the sonicated volume is increased by a factor of 3, same as at translation error of 5 mm, and at 17.5° this increase arrives at almost 30 times the volume covered wile the transducer-lens system is located in the original position. For translation errors, at 8 mm, the brain sonicated volume is 13 times greater. These values indicate that large misalignments result in a high defocusing, as expected, but for relatively small errors, e.g., a rotation of 5° or a translation of 4 mm, the acoustic images are still generated with good quality. Note the wavelength at 650 kHz in water is 2.3 mm, so images are restored even for misalignments greater than the wavelength (see Fig. 6.8 (b-d) and Fig. 6.9 (c-d)).

The last studied hologram is the corresponding to the C5 configuration. This hologram presents a similar behaviour than the C3 configuration. Both focus had a similar pressure gain in the original location. When rotating 5° the amplitude loss is 17% and 6% for the left and right focus, respectively (see Fig. 6.8 (a) and Fig. 6.9 (a)). For a 5 mm translation error, the loss arrives at 18% and 13%, respectively. At higher rotation angles and translation distances, pressure values for the left focus remain constant; for a rotation of 17.5° and for a translation of 8 mm, the pressure loss was about 18%. On the other hand, for the right focus, a decrease of 31% is reached for a rotation of 17.5°, and a loss of 44% was observed for a translation of 8 mm. Sonicated volumes in and outside the target are almost constant, the variations are 1.5 times the original value for rotations

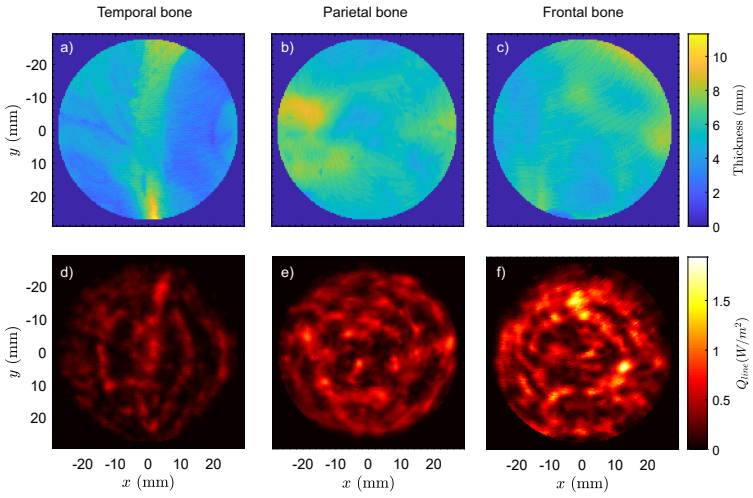

Figure 6.10: Skull thickness measured at (a) temporal bone window, (b) parietal and (c) frontal bones. (d-f) Heating rate per unit area obtained when targeting the holographic beam through the (d) temporal bone window, (e) the parietal and (f) the frontal bone.

below 5° and translations below 4 mm. These sonicated volumes increase for greater rotation or translation errors. The sonicated target volume arrives at a maximum, where a volume of 2.4 times greater than the original was observed for a rotation of 10°. At this rotation, the sonicated brain tissue is 4.5 times larger than in the original position. At the maximum studied translation error (8 mm), the sonicated target volume is 2.5 times larger and the sonicated brain tissue is 5.3 times larger than in the original position (see Fig. 6.8 (b-d) and Fig. 6.9 (c-d)). Note that this behaviour is similar for all studied holograms.

6.3.5 Skull heating rate

We have studied the heating rate by targeting the thalamus through different regions of the same skull. We have designed holograms to target the same location, i.e. a point between both thalamic structures (C1 configuration). The transducer is located at the temporal bone window, the parietal and the frontal bone. Bone thickness at each area is shown in Fig. 6.10 (a-c). The thickness is measured on a circle of about 55 mm diameter, matching the projection of the active hologram aperture on the bone surface. Average values of their thickness are 4.34, 5.98 and 5.69 mm for the temporal, parietal and frontal bones, respectively. The skull heating rate is calculated as described in *Materials and Methods*, considering that a peak pressure of 0.5 MPa is achieved at the target.

The obtained total absorbed power (W_Q) was 0.39, 0.74 and 0.99 W for the temporal, parietal and frontal bones, respectively, whilst the heating rate was of 2.1, 2.4 and 3.2 $degC/min$. The absorbed power per unit area is shown in Fig. 6.10 (d-f). Average heat capacity of the frontal bone and the parietal bone are 392 W/m^2 and 294 W/m^2, respectively, while for the temporal bone this parameter takes a value of 149 W/m^2, which is less than half the heat capacity of the other two bones. As expected, thicker bones results in higher heating rates.

6.3.6 Patient-specific lenses

Finally, we show the results of the study on different patients. The first set of simulations using the lens designed for the subject #1 (C1 configuration) but focusing on subjects #2-#4 is shown in Figs. 6.11 (a-c). It can be observed that the focal spot is not perfectly reconstructed, and strong aberrations distort the focal spot. The total gain for subjects #2-#4 is 2.0, 3.1, and 2.5, respectively. However, when a hologram is designed ad-hoc for each patient, aberrations are corrected as shown in Figs. 6.11 (d-f). Using patient-specific lenses the total gain for subjects #2-#4 rises to 4.4, 5.5, and 4.9, respectively. In addition, by using a personalized lens the side lobes are strongly reduced, and the strong secondary focal spots are no longer observed. This data shows that the skull aberrations are patient specific even when targeting from the temporal bone window using a 50-mm aperture system.

6.4 Discussion

Several strategies to design ultrasound holograms using virtual sources to enhance sonicated thalamic tissue and correct skull aberrations are presented and discussed in this Chapter. While designed to target a point, holograms allow for aberration correction and the resulting gain is increased as compared with the focused source, e.g., 1.6 times higher. Simultaneously, when designed to target a unique focal point, holograms can minimize the out-of-target volume, 6.3 times less compared to the focused source, indicating the ability of these lenses to mitigate aberrations. On the other hand, holograms allow to adapt the acoustic focus, i.e., the acoustic image, to the shape of the therapeutical target, in this case the two bilateral nuclei of the thalamus. In this way, a much higher volume of the target can be covered by the therapeutical beam, which can be useful for medical applications that need good covering of the target. The greatest sonicated target volume is achieved using bifocal wide holograms, about 5 times greater than using a focused source, even when the conventional beam is in fact defocused due to aberrations.

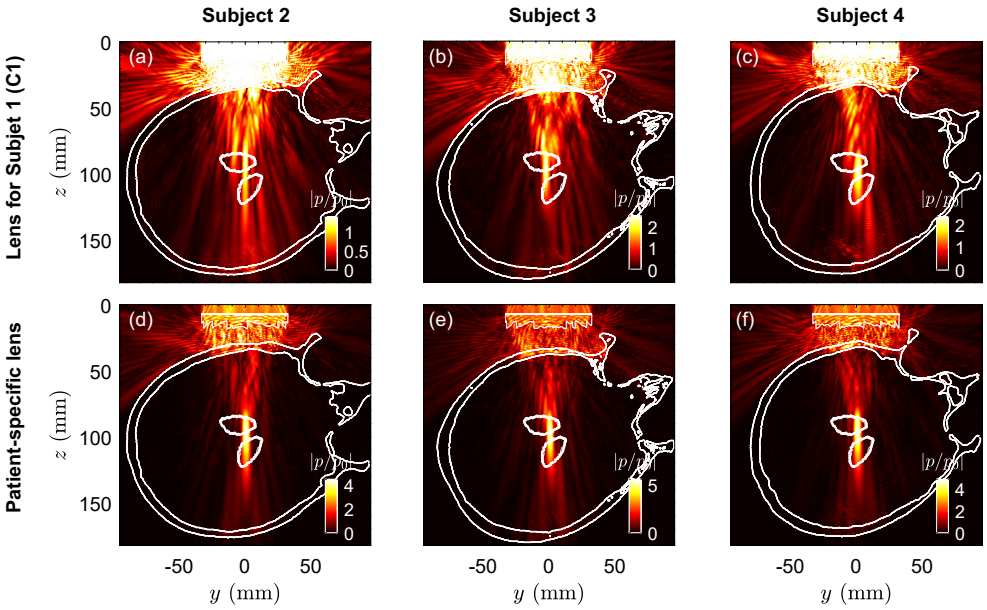

Figure 6.11: (a-c) Acoustic field simulated using the hologram designed for the subject #1 but focusing on subjects #2-#4. (d-f) Acoustic field simulated using a patient-specif hologram.

The process of generating the hologram includes the treatment planning, CT/MRI image processing, and both backward and forward simulation at the transducer central frequency on an Intel-Xeon workstation (E5-2680@2.8GHz CPU, 256 GB RAM), taking a total of about 46 hours. The physical lens is printed and ready in about 6 hours, so the whole process to treat a specific patient will last about two days from the reception of the CT image and segmented therapeutic target to the manufacturing of the holographic lens ready for the treatment. Shorter times should be obtained by performing the simulations on high performance computers, e.g., using GPUs, and/or using faster industrial 3D printers.

However, acoustic holograms show several drawbacks. On the one hand, when holograms are designed to generate a wide acoustic image, e.g., bilaterally covering both nuclei, the gain is generally reduced. In fact, the lens is defocusing the therapeutic beam and the acoustic energy is distributed in a higher area. A reduction of about 40% compared to the focused source was observed. This effect can be mitigated increasing the amplitude of the source, but attention must be paid to additional effects outside the target, e.g., heating effects in the skull. Selecting the temporal window to locate the source will help to mitigate skull heating as skull bones are thin at this region, which in fact is

one of the main motivations of this work. The skull heating rate of this region has been estimated and compared to other targeting regions, the parietal and frontal bones. The total heating rate of the temporal bone window is approximately half that of the parietal bone and less than half the corresponding to the frontal bone. On the other hand, note that the retrieved acoustic images using holographic lenses are a diffraction-limited version of the target. When targeting deep-brain nuclei using a limited-aperture source, such as the transducer used in this Chapter, the generated acoustic image can spread in the axial direction. This effect increases the out-of-target region of wide holograms. The out-of-target volume can be mitigated increasing the effective f-number of the source, i.e., increasing the aperture of the transducer. However, in the application proposed in this Chapter the transtemporal window limits the maximum aperture.

Note that the selected strategy to design the holograms in this Chapter was a direct method for a flat circular transducer, using virtual sources and a time-reversal method, therefore, the lens was designed to produce a set of focal spots covering the target. Optimization techniques applied to transcranial propagation can help to design holograms producing a better matching between the diffraction-limited focal spots and the target [169], or using multi-frequency approaches [53]. Other effects, such as the heating of the lens due to acoustic absorption can be mitigated using a water-coupling system, or using novel 3D printed materials with low absorption coefficient.

In this study, therapeutical targets are located in the deep-brain area, quite central inside the brain. For this scenario, holograms designed for flat or slightly focused transducers are able to correct skull aberrations and generate the desired acoustic image. If the therapeutical targets were located closer to the skull, curvilinear holographic lenses coupled to focused transducers would present better performance than flat or bulk holograms, according to the results shown in Chapter 2.

In a realistic scenario, the physical location of the acoustic hologram and the ultrasound source with respect to the patient's head will show some degree of misalignment from the design location. The results of this work show that when using a focused transducer without hologram, the shape and gain of the produced acoustic field hardly changes when it is rotated around the centre of the thalamus, which is logical because the incidence is always normal to the skull and the focused transducer presents a stable acoustic field. However, rotations with other references can result in uncontrolled focusing [164]. On the other hand, when using acoustic holograms, the retrieved acoustic images are robust under relatively small misalignment. The degradation of the focal spots in terms of focal gain and targeting volumes was quantified. For the line hologram, the effect of misalignment is not so relevant than in the two-focus holograms due to the relative simplicity of the former compared to the latter. This can be seen by comparing the spreading of the focus for large rotations (or translations). For the line hologram, the volume outside the

target at the maximum studied rotation error (17.5°) is increased 1.5 times compared to the original location, while for the two lines hologram is increased 4.5 times and for the two points it arrives at 30 times greater. This means that for this target the transducer-lens system is less robust as more complex is the performed hologram. When the relative position between the head and the transducer is slightly different to the design, e.g., a rotation of 5° or a translation of 4 mm, the acoustic images are still accurately reconstructed, even for translations larger than a wavelength, in all the studied cases. The required precision can be achieved using image-guided systems, see e.g., [33].

Due to the diffraction in the axial direction or the misallocation of the focus in the lateral dimensions, adjacent deep brain structures could be sonicated. If errors are made along the propagation axis of the transducer (z direction), structures as the putamen or the globus pallidus could be partially sonicated. If the focus suffers translation in the negative x-axis (towards the parietal bone), the caudate nucleus can be affected, while if there is a shift in the positive x-axis and in both positive and negative z-axis, portions of the hippocampus and amygdala could be sonicated. All these structures except the amygdala participate in the coordination of fine motions and inhibit non-desired movements. Between other functions, the amygdala links emotions as fear or aggression to human experiences. Finally, between both thalamic nuclei, we can find the third ventricle, which could be potentially sonicated. This structure is a part of the ventricles, connects both hemispheres and produces, contains and distribute cerebrospinal fluid. It is important to note that when translation and angle errors occur, we have observed that pressure gain decreases. Therefore, neuromodulatory or other bio-effects on out-of-target structures will be low or even may not happen. The higher peak pressure is only observed at the target, and when the lens is at its design location.

6.5 Chapter conclusions

In this Chapter, acoustic holograms are numerically studied to target the thalamus through the temporal bone window using a 65-mm aperture transducer working at 650 kHz, and compared to a focused source with the same aperture and a curvature such that it can sonicate in the centre of both thalamic nuclei. The results show that holograms can enhance the targeting performance of the focused transducer in terms of treated volume and focal aberrations because they can improve focus quality and optimize sonicated volume ratio between brain and target tissues.

Secondary lobes and aberrations appearing using single element focused transducers can be corrected and focal spots can be adapted to the target even for bilateral sonications. These lenses also show a good focusing performance under relatively small mislocation of the therapeutic device. Nevertheless, when creating bilateral focusing, not only

sonicated target volume increases, but also out-of-target volume, a consideration that must be taken into account when deciding what hologram suits best for each therapeutical approach. Simple bilateral-point holograms minimize out-of-target focusing, while bifocal-plane holograms, while covering a larger area of the target deep-brain nuclei, may focus energy at adjacent CNS structures, which seems undesirable for neuromodulation applications [164], as a result of the limited angular spectrum of this trans-temporal transducer. Enlarging the aperture of the transducer, or using optimization methods to generate the hologram, have the potential to improve targeting performance of broad holograms, and recent advances on spatial sound modulators can open new ways to design reconfigurable holograms and go beyond traditional phased-array systems [170].

The results shown in this study also demonstrate that when a lens designed for one patient is used on a different subject the acoustic image cannot be reconstructed with accuracy because aberrations, even those produced at the temporal bone window, are strongly dependent on subject's skull anatomy. The particular anatomy of the patient's head is shown to be very relevant during trans-temporal targeting, and patient-specific lenses should be designed to obtain an accurate focusing, i.e., to reconstruct diffraction-limited acoustic images without aberrations. Finally, targeting through the temporal window offers other practical advantages such as reduced skull heating and the need to shave only a small area of the head. These results pave the way to design accurate therapeutic devices for neuromodulation or drug-delivery through blood-brain barrier opening in deep-brain structures using a low-cost and patient-specific approach.

Publications

The contents of this Chapter have been presented in the following publications:

Journal papers

Andrés, D., Jiménez, N., Benlloch, J. M., & Camarena, F. (2022). Numerical study of acoustic holograms for deep-brain targeting through the temporal bone window. *Ultrasound in Medicine & Biology*, 48(5), 872-886.

Conference papers

Andrés, D., Jiménez, N. & Camarena, F. (2021). Holographic lenses to enhance thalamic therapy through the temporal bone window. *20th International Symposium for Therapeutic Ultrasound (ISTU 2021)*. Gyeongju, Republic of Korea. June 6-9, 2021.

Andrés, D., Jiménez, N. & Camarena, F. (2021). Acoustic holograms for thalamic focusing through the temporal-bone window. *180th Meeting of the Acoustical Society of America*. Online. June 8-10, 2021. Published in The Journal of the Acoustical Society of America, Volume 149, Issue 4 (https://doi.org/10.1121/10.0004703)

Andrés, D., Jiménez, N. & Camarena, F. (2021).Transtemporal Ultrasound Holograms for Thalamic Therapy. *2021 IEEE International Ultrasonics Symposium (IUS)*. Online. September 11-16, 2021. Published in *2021 IEEE International Ultrasonics Symposium (IUS) (ISBN: 978-0-7381-1209-1). IEEE.*

Andrés, D., Pi-Martín, I., Jiménez, N. & Camarena, F. (2021). Therapeutic ultrasound holograms to target thalamic nuclei through the temporal bone window. *European Congress and Exposition on Noise Control Engineering (EuroNoise 2021)*. Online. October 25-27, 2021. Published by *Sociedade Portuguesa de Acústica (SPA) (ISBN: 978-989-53387-0-2)*.

Andrés, D., Jimenez-Gambin, S., Jiménez, N., Camarena, F. & Benlloch, J. M. (2021). Ultrasound holograms to enhance deep-brain neuromodulation. *2nd FUN Symposium*. Online. September 7-10, 2021.

Chapter 7

Experimental evaluation of transcranial ultrasonic lenses using acoustic holographic projections

Evaluating the targeting performance of ultrasonic 3D-printed holograms requires the measurement of complex volumetric acoustic fields, which in many practical situations cannot be estimated by direct hydrophone measurements. In this Chapter, we apply single-plane holographic measurement techniques to experimentally calibrate and measure the full volumetric field produced by holographic lenses. Two ex-vivo test cases are presented, a four-foci lens and a preclinical case, both targeting through a macaque skull. Time-reversal and angular spectrum projection methods are compared to direct experimental measurements. Results show that holographic projection methods can reconstruct the complex acoustic images produced by holographic lenses, matching direct measurements in all test cases. However, while direct measurements are restricted to transverse field cross-sections, holographic projection allows estimating the field on the whole targeting volume. In this way, the location and the full three-dimensional shape of all acoustic foci can be obtained. Furthermore, these techniques can provide the field at the surface of the lens to compare it to the design phase distribution. Using this procedure, complex volumetric acoustic fields can be reconstructed, saving significant measurement time and computational resources, and enabling an accurate characterization of phase-plates and other holographic lens topologies.

7.1 Introduction

Holography was first proposed in optics at the mid-twentieth century [92], and short time later, around the 1960s, optical holography was combined with acoustic systems to generate optical images [171, 172]. Acoustic holography allows imaging of optically opaque objects by combining diffraction and interference of acoustic wavefronts. Acoustic holographic imaging can use one or more acoustic beams to generate a sound field over an object. Then, the scattering is raster scanned to generate the image. In contrast, acousto-optical holographic techniques use the acoustic radiation pressure produced by the scattered field to generate an interference pattern at a liquid-gas interface, which is optically detected and used to generate a real-time image. In this context, several applications were already reviewed in the 1970s [173]. Later, Fourier-acoustics methods were applied in near-field acoustic holography techniques to evaluate the spatial pattern of vibration and radiation of acoustic sources [174, 175], becoming a standard practice in acoustic engineering, e.g., for noise control and visualization, wave field synthesis or loudspeaker design.

Recently, acoustic holography has become a powerful metrological tool for characterizing ultrasound fields generated by imaging and therapeutic applications, e.g., to characterize the radiation pattern produced by High Intensity Focused Ultrasound (HIFU) transducers [176, 137]. This robust technique has been included as a part of IEC standards for ultrasound field metrology (IEC TS 62556:2014)[177]. Among other applications, holography has been proposed for acoustic field reconstruction through complex media [178]. In all these techniques, by measuring the acoustic field in a plane, e.g., transversally to an ultrasound beam, acoustic holography enables the knowledge of the field on an orthogonal plane, e.g., at the surface of the source.

Beyond these metrological and imaging techniques, holography has also been proposed to modulate acoustic wavefronts, generating acoustic images at a given target distance [179, 100, 55, 180]. In this context, and acoustic image is defined as an acoustic field with arbitrary amplitude distribution. For ultrasound, phased-array systems were proposed first to tune the phase and amplitude along the surface of the transducer, mimicking a hologram, allowing to synthesize acoustic images even traversing absorbing areas [93]. While phased-arrays provide reconfigurability, the holographic information encoded on the transducer surface is strongly limited by the small number of piezoelectric elements of the current systems, limiting the hologram capability to generate complex acoustic images. With the rise of 3D-printing techniques, acoustic holograms can be generated via holographic lenses [51, 96, 53, 95]. In this case, the holographic information becomes encoded in a passive structure, e.g., a 3D-printed lens of rough surface, which modulates the transmitted phase of the ultrasound field generated by a transducer. Among other applications, acoustic holograms have been proposed for ultrasound particle manipulation

and trapping [101], acoustic vortex generation for transmitted [181] or reflected wavefronts [103], fast 3D-printing via volumetric particle agglomeration [56], cell patterning [58], generation of cavitation patterns [59], producing arbitrary-shaped thermal patterns in tissues using ultrasound [182], tuning the acoustic field to control the total thermal dose on multiple targets for ultrasound hyperthermia [183], or performing 3D acoustic imaging using a single-channel transducer [106].

One emerging application of 3D-printed acoustic holograms is transcranial ultrasound for non-invasive brain therapy [63]. During transcranial ultrasound, the high acoustic contrast between soft-tissues and the skull bones produces strong beam refraction, scattering and absorption. For example, when using a single-element focused ultrasound transducer, the transmitted beam suffers from strong aberrations, and the targeting accuracy on the brain relies on simulation techniques during treatment planning to find the best-case scenario [154, 33]. Therefore, wavefront aberration correction is desirable for precise targeting inside the brain [184, 185]. To avoid these limitations, state-of-the-art clinical systems are based on therapeutic phased-array systems [151], allowing beam steering and aberration correction. However, in addition to their complexity and high cost, the steering range of therapeutic arrays is limited to a narrow region around the centre of the array. Since they are composed of large piezoelectric surfaces, diffraction grating appear, limiting their focusing performance. Recently, 3D-printed holographic lenses coupled to flat or focused transducers have been proposed for aberration correction for focused beams [61], and even adapting the acoustic field to arbitrary brain targets [63, 107]. It has been shown that acoustic holograms can generate arbitrary and complex patterns within human skulls [64]. They have been recently applied for blood-brain barrier opening in small laboratory animals, creating multiple sharply-focused spots close to the diffraction limit [65], or wide focal areas [66]. In all these biomedical applications, a mandatory step before in-vivo trials is to validate the acoustic field produced by the hologram in the relevant scenario.

Usually, the field generated by a therapeutic focused ultrasound transducer is assessed by direct measurements using hydrophones in a water tank [186]. While this approach is convenient for axisymmetric beams, e.g, those focusing at a single focal spot, the acoustic images produced by holographic lenses can present a far more complex spatial distribution over a large volume. In practice, the direct evaluation of the targeting performance of complex acoustic holograms requires huge amount of data and measurement time, making unfeasible the estimation of the field over a large volume. In addition, for transcranial validation measurements, the size of the hydrophone limits the measurement range inside a skull. Faster techniques such as acousto-optical Fabry-Perot interferometers [187] require large sensors, limiting their application in transcranial ultrasound. Well-known optical methods such schlieren imaging [188] or Doppler velocimetry [189] can provide a volumetric field estimation, but they require transparent optical windows and complex

instrumentation. Note schlieren imaging can also be combined with optical holographic interferometers to estimate the acoustic field [190]. Indirect thermometric methods include the use of liquid-crystal thermochromic sheets sandwiched between sound absorbing materials [191]. Ultrasound absorption results in heat, and the temperature change produces a variation of the optical colour of the sheet, that is detected by a camera. This method results in a fast transverse field scanning, however, it becomes difficult to calibrate. An alternative is the use of a thin sound-absorbing membrane combined with a thermal camera to measure the temperature at its surface [192]. However, the thermal radiation does not propagate through water and the method is limited to measurements on the surface of the water-tank. To overcome these limitations, magnetic-resonance thermometry techniques become more reliable for evaluating the field of acoustic holograms inside tissues [182], but these systems are expensive and unaffordable for many biomedical ultrasound research facilities. A faster and robust method is therefore desirable for volumetric field evaluation, in particular for transcranial holographic devices.

In this Chapter, we apply acoustic holography [176, 137] to experimentally and efficiently evaluate transcranial ultrasound fields produced by complex holographic lenses targeting through an ex-vivo macaque skull. To evaluate the complex field produced by the lenses, three measurement methods are compared. First, direct hydrophone measurements, second, a projection technique based on time-reversal full-wave simulations and, third, a projection using the angular spectrum method. These methods are tested on two holographic lenses. The first one is designed to create four equidistant foci inside the macaque skull, while the second lens is designed to focus on the left post-commissural putamen of the specimen. Furthermore, the field at the exit surface of the lens is estimated experimentally using holographic techniques, and compared with the design phase field. The experimental fields are compared with full-wave simulations of the system, taken as the gold-standard. Figure 7.1 illustrates the process to reconstruct the acoustic field at the focus from a single measured holographic plane. First, as shown in Fig. 7.1 (a), a hologram modulates the wavefront generating an acoustic image inside a skull and the corresponding acoustic field in the holographic plane. Then, as shown in Fig. 7.1 (b), a holographic projection technique is used to estimate the field along a target volume inside the skull. Fig. 7.1 (c) summarizes the three acoustic field reconstruction algorithms discussed in Section 7.2.

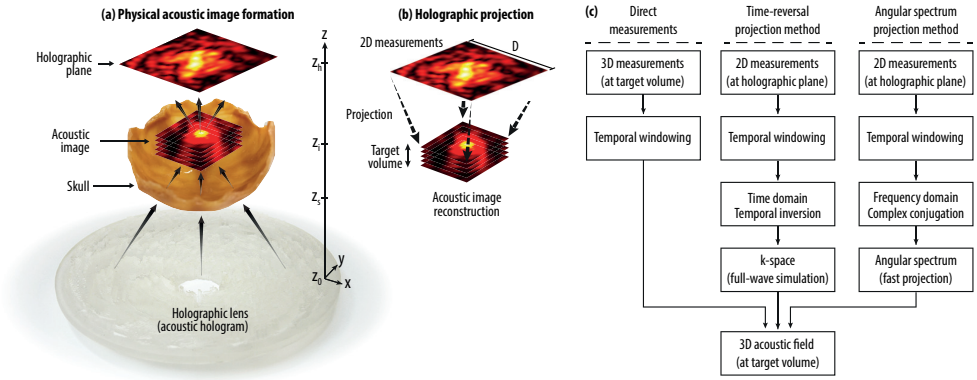

Figure 7.1: (a) Schematic representation of the process to reconstruct the acoustic field at the focus from a single measured holographic plane. (b) Detail of the holographic projection. (c) Block diagram of the acoustic field reconstruction algorithms.

7.2 Techniques for field estimation

7.2.1 Direct measurements

Direct field measurements consist of scanning the area of interest with a hydrophone to record the corresponding waveforms. The hydrophone is usually mounted on a 3D positioning system and synchronized point-by-point measurements are performed to cover the desired target, e.g., 2D planes or even 3D volumes. This technique presents the advantage that the acoustic pressure is directly measured. However, acquiring large volumes requires long measurement time and large amount of data and the instrumentation can interfere with the field or objects such as the skull bones like in the case presented here.

7.2.2 Holographic projection methods

To avoid point-to-point scanning over the whole volume, holographic projection methods only require the direct measurements at a plane, the holographic plane, normally transverse to the beam, located at a distance $z = z_h$ and covering a squared area of side length D (see Fig. 7.1). Then, the field at any point is calculated using a projection method.

Projection using time-reversal simulations

The time-reversal simulation projection method rely on the time-reversal invariance of the wave equation in a lossless medium. To project the field using time-reversal simulations, we use a full-wave simulation method which solves the system of constitutive acoustic equations for a lossless homogeneous medium

$$\frac{\partial \rho(\mathbf{r},t)}{\partial t} = -\rho_0 \nabla \cdot \mathbf{v}(\mathbf{r},t) + \frac{\partial q(\mathbf{r}_h,t)}{\partial t}, \tag{7.1}$$

$$\frac{\partial \mathbf{v}(\mathbf{r},t)}{\partial t} = -\frac{1}{\rho_0}\nabla p(\mathbf{r},t), \tag{7.2}$$

$$p(\mathbf{r},t) = c_0^2 \rho(\mathbf{r},t), \tag{7.3}$$

where $\mathbf{v}(\mathbf{r},t)$ is the particle velocity field, $p(\mathbf{r},t)$ is the pressure, $\rho(\mathbf{r},t)$ is the acoustic density, ρ_0 is the medium density, c_0 is the sound speed, and $q(\mathbf{r}_h,t)$ is a spatial distribution of monopole sources, $\mathbf{r} = (x,y,z)$ and $\mathbf{r}_h = (x,y,z_h)$. These equations are solved numerically using a pseudo-spectral time-domain simulation method, implemented in the software k-Wave [117].

To make use of the time-reversal mirror symmetry, we acquire the experimental pressure waveforms over the holographic plane, $p_h(\mathbf{r}_h,t)$. A temporal window is applied to the signals to avoid reflections from boundaries. Then a temporal inversion is applied, letting $p_h(\mathbf{r}_h,t) \rightarrow p_h(\mathbf{r}_h,-t)$. Finally, the computational solution is found by setting the monopole source amplitude in Eq. (7.1) to $q(\mathbf{r}_h,t) = p_h(\mathbf{r}_h,-t)/c_0^2$. Note that time-reversal symmetry no longer holds in absorbing media [193]. In this Chapter, we measure the field in pure water, whose absorption at ultrasonic frequencies can be considered negligible for a propagation path length of tens of wavelengths.

Projection using angular spectrum

Angular spectrum approach was also used to project the measured field at the holographic plane to several planes covering the target volume. This calculation was performed assuming neither absorption nor medium stratification. First, we calculate the frequency-domain amplitude of each spectral component of the field measured at the holographic plane, $z = z_h$, by a Fourier transform

$$P\left(x,y,z_h,\omega\right) = \int_{-\infty}^{\infty} p_h\left(\mathbf{r}_h,t\right) e^{i\omega t} dt. \tag{7.4}$$

Then, each spectral component of the field is complex conjugated, $P\left(x,y,z_h\right) \rightarrow P^*\left(x,y,z_h\right)$, to perform the temporal inversion in the frequency domain. In the spatial Fourier space, each spectral component of the field is given by

$$\tilde{P}^*\left(k_x,k_y,z_h\right) = \iint_{-\infty}^{+\infty} P^*(x,y,z_h)e^{i(k_x x+k_y y)}dxdy. \tag{7.5}$$

In this way, the field is decomposed into a spectrum of plane waves travelling in different directions, being their azimuth, θ, and elevation angles, ϕ, related to the transverse components of the wavevector by

$$k_x = k\cos\theta\sin\phi, \tag{7.6}$$

$$k_y = k\sin\theta\sin\phi, \tag{7.7}$$

where $k = \omega/c_0$. Each spectral component measured at the holographic plane $z = z_h$ is projected to the image plane $z = z_i$ by multiplying it in the Fourier space with the spectral propagator $H\left(k_x,k_y,z_i,z_h\right)$ as

$$\tilde{P}\left(k_x,k_y,z_i\right) = \tilde{P}\left(k_x,k_y,z_h\right)H\left(k_x,k_y,z_i,z_h\right), \tag{7.8}$$

where the spectral propagator for the pressure field, assuming a Fourier time convention of the type $e^{i\omega t}$, is defined as [194],

$$H\left(k_x,k_y,z_i,z_h\right) = e^{-ik_z|z_h-z_i|}, \tag{7.9}$$

where the axial component of the wavevector is given by

$$k_z = \sqrt{k^2-(k_x^2+k_y^2)}. \tag{7.10}$$

Therefore, if $k_x^2+k_y^2 \leq k^2$, then k_z is real and the propagator consists of propagating modes, while if $k_x^2+k_y^2 > k^2$, then k_z is purely imaginary and the propagation function models the rapidly decaying evanescent modes of the field. Angular restriction is applied to avoid aliasing of rapidly oscillating waves propagating at grazing angles, using a low-pass circular window of radius $k_c = k\sqrt{D^2/2(D^2/2+z^2)}$ in the k-space [195].

For each spectral component, an inverse spatial Fourier transform of $\tilde{P}(k_x,k_y,z_i)$ is computed to recover the field amplitude $P\left(x,y,z_i\right)$ in the spatial domain,

$$P(x,y,z_i) = \iint_{-\infty}^{+\infty} \tilde{P}\left(k_x,k_y,z_i\right)e^{-i(k_x x+k_y y)}dxdy. \tag{7.11}$$

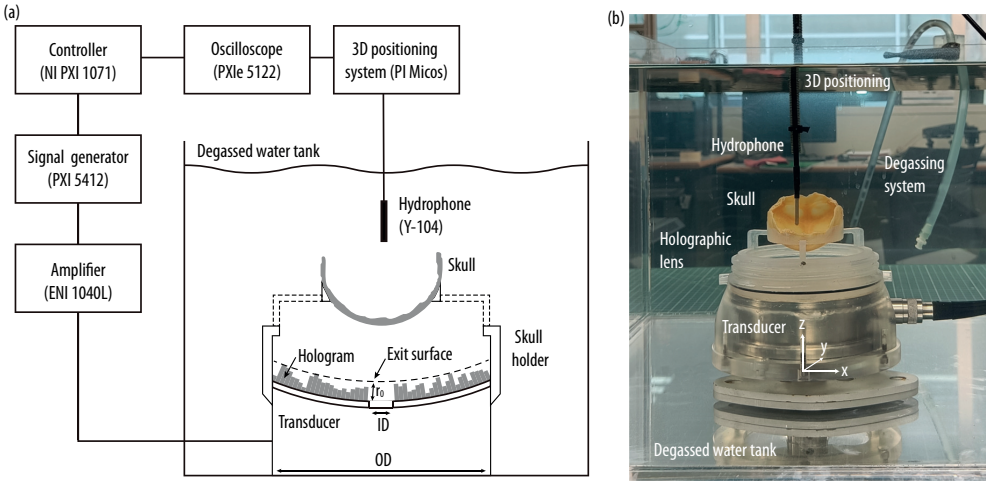

Figure 7.2: (a) Schematic and (b) real image of the experimental setup.

Finally, an inverse Fourier transform is applied at each location to recover the temporal waveforms in the time domain, as

$$p\left(\mathbf{r}_i, t\right) = \int_{-\infty}^{\infty} P\left(x, y, z_i\right) e^{-i\omega t} dt, \tag{7.12}$$

where $\mathbf{r}_i = (x, y, z_i)$. In this Chapter, angular spectrum was used to evaluate the acoustic volume generated by the holographic lens inside the skull, $z_h > z > z_s$, z_s being the distance between the holographic plane and the inner surface of the skull. We project all spectral components of the measured signals.

Note, the Fourier-space product of Eq. (7.8) is equivalent to a spatial convolution from the plane z_h to z_i of the field $P^*(\mathbf{r}_h)$, given by Eq. (7.4), with the spectral propagator function, Eq. (7.9), in the spatial domain, the latter given by $h(\mathbf{r}_h, \mathbf{r}_i)$. In addition, the spatial domain propagator relates to the Green's function of the Helmholtz equation in 3D as $h(\mathbf{r}_h, \mathbf{r}_i)/2 = \partial G(\mathbf{r}_i, \mathbf{r}_h)/\partial z$, where $G(\mathbf{r}_i, \mathbf{r}_h) = e^{-ikr}/4\pi r$, and $r = \sqrt{(x_i - x_h)^2 + (y_i - y_h)^2 + (z_i - z_h)^2}$. Therefore, Eq. (7.8) is equivalent to the second Rayleigh-Sommerfeld diffraction integral, but since the spectrums are calculated using the Fast Fourier transform algorithm, it results in a more computationally efficient method.

7.3 Experimental setup

7.3.1 System design

A spherically focused custom-made ultrasound transducer with outer diameter $OD = 100$ mm and $R = 140$ mm radius of curvature, with an inner aperture diameter of $ID = 20$ mm and central frequency $f = 500$ kHz was used. The piezoelectric ceramic is mounted in a customized stainless steel housing, with air backing. To tune the field of the transducer, a holographic 3D-printed lens was attached to it. Evaluation of the acoustic field was done in water and through an ex-vivo cut out and hollowed out non-human primate skull, of the species *macaca mulatta*. A coupling cone and a supporting frame for the skull were 3D printed to position the skull relative to the transducer and the lens during measurements (see Fig. 7.2).

7.3.2 Lens design and manufacturing

Holograms were calculated with time-reversal methods considering the boundary conditions used in the experimental validation, i.e., including the ex-vivo skull and also the coupling cone and the supporting frame, as described in [63].

The time-reversal method employed consisted on locating virtual sources at the focused desired target and simulating their radiated field during long time to take account for several reflections. These acoustic signals were recorded in a spherical exit surface parallel to the transducer, as described in Chapter 2.

Each curved lens is implemented in the numerical model for validation and also 3D printed with stereolithography techniques (Form 3, Formlabs, USA) using the Clear photopolymer, whose density and sound speed values were experimentally obtained (ρ_L = 1186 kg/m^3 and c_L = 2599 m/s, respectively). Attenuation value was set to α_L = 3.4 dB/(cm-MHz$^\gamma$) as reported in the literature for similar photopolymers [63, 51].

7.3.3 Test cases

Two holographic lenses were designed and evaluated in this study: a first lens with which we wanted to create four equidistant foci across the skull (*four-foci lens*), and a second preclinical case where we aim to target the left post-commissural putamen of a macaque (*preclinical lens*). Ex-vivo macaque skull morphology and acoustic characteristics were derived from tomographic images acquired with a Toshiba Aquilion Prime TC scanner, with in-plane resolution of 0.245 mm and slice thickness of 1 mm. These X-ray attenu-

ation values were converted into acoustic impedance data (density and sound speed) by using the linear empirical relationships obtained by [80] adjusting the data from [79], implemented in the software k-Wave [117].

Tomographic data were interpolated to an isotropic spatial step of $dh = \lambda_0/6$, where $\lambda_0 = c_0/f_0$ in water, which corresponds to $dh = 0.5$ mm, matching the numerical grid used in simulations. Average and maximum density and sound speed values were as follows: $\rho_{avg} = 1563$ kg/m^3, $\rho_{max} = 2542$ kg/m^3, $c_{avg} = 2191$ m/s and $c_{max} = 3237$ m/s. Acoustic attenuation was taken into account for backward and forward propagation simulations for both designing and numerically validating the holographic lens. This physical magnitude was considered to be constant for all the skull and set to $\alpha = 9.6$ dB/(cm-MHz$^\gamma$), with γ = 1.1, according to [81].

To create the four-foci lens, four virtual sources were located at the coordinates (x, y, z) (-5.6, 5.6, 63) mm for focus F_1, (-5.6, -5.6, 63) mm for focus F_2, (5.6, 5.6, 63) mm for focus F_3, and (5.6, -5.6, 63) mm for focus F_4. The preclinical lens was created by setting a virtual source in the middle of the target brain structure, the left post-commissural putamen of the specimen, that was identified in co-registered MRI images by an experienced neuroscientist, at coordinates (-6.6, -11.2, 55.3) mm. Each virtual source was set to emit sinusoidal continuous signals with the same phase and amplitude, and the resulting wavefront was recorded at the exit surface, located at $r_0 = 4$ mm in both cases.

Numerical validation of the acoustic field generated by each holographic lens was performed by considering the transducer was homogeneously vibrating, producing a 20-cycle sinusoidal pulsed-burst signal, with unitary amplitude. Maximum pressure in steady state was recorded, and its amplitude was scaled to the maximum pressure obtained experimentally using the angular spectrum projection.

7.3.4 Experimental procedure

All acoustic experiments were carried out in a tank of dimensions $400 \times 800 \times 600$ mm^3, filled with degassed water at room temperature maintained by a water conditioning unit (WCU Series, Sonic Concepts, USA).

We used high-temperature water-insoluble coupling gel (Sonotech Sono 600) to ensure constant coupling of the lens to the transducer during experiments. The transducer was excited with a 20-cycle sinusoidal pulse burst at 500 kHz using a signal generator (model PXI-5412, 14-bit, 100 MS/s, National Instruments, USA) and amplified with a linear RF amplifier (model 1040L, 400 W, 55 dB, ENI, Rochester, NY, USA). Acoustic fields were measured with a piezoelectric hydrophone (model Y-104, -225.5 dB re 1 V/μPa at 1 MHz, Sonic Concepts, USA), calibrated from 40 kHz to 2 MHz, mounted on a 3D axis

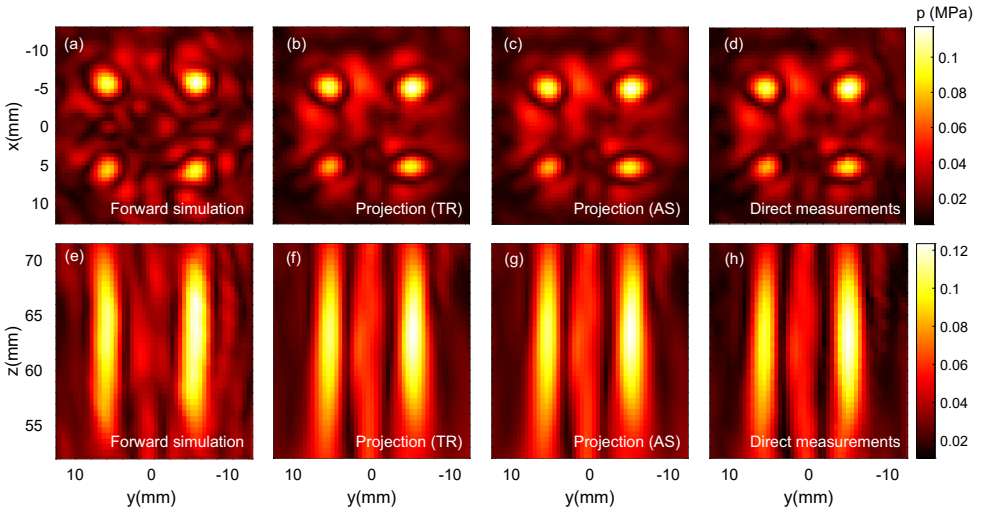

Figure 7.3: Transverse field, $p(x, y)$, for the four-foci lens at $z = 63$ mm for (a) forward simulation, (b) time-reversal projection, (c) angular spectrum projection and (d) direct measurement. Axial field, $p(y, z)$, for (e) forward simulation, (f) time-reversal projection, (g) angular spectrum projection and (h) direct measurements.

system (5 μm resolution, PI Micos GmbH, Germany). Lens, cone and skull holder were 3D-printed and mounted matching simulation conditions. The skull was located into its holder, which smoothly fitted on the design position. A schematic and a photograph of the experimental setup are presented in Fig. 7.2.

The origin of coordinates was set at the centre of the hole of the transducer. Direct measurements of the four-foci lens were performed in two xz planes ($-12.5 < x < 12.5$ mm, $47 < z < 72$ mm, at $y = -5.6$ mm and $y = 5.6$ mm, respectively), two yz planes ($-12.5 < y < 12.5$ mm, $47 < z < 72$ mm, at $x = -5.6$ mm and $x = 5.6$ mm, respectively) and one xy plane ($-12.5 < y < 12.5$ mm, $-12.5 < x < 12.5$ mm, at $z = 63$ mm). The 2D measurement for holographic projection was performed in a xy plane of 35×30 mm^2 at $z = 72$ mm.

Direct measurements of the preclinical lens through the skull were performed in one xz plane ($-14.5 < x < 1.5$ mm, $44 < z < 71$ mm, at $y = -11$ mm), one yz plane ($-19.5 < y < -5.5$ mm, $44 < z < 71$ mm, at $x = -6.5$ mm) and one xy plane ($-19.5 < y < -5.5$ mm, $-14.5 < x < 1.5$ mm, at $z = 55.5$ mm). The 2D measurement for holographic projection was performed in a xy plane of 32×37 mm^2 ($-21.5 < x < 10.5$ mm, $-28 < y < 8.5$ mm) at $z = 71$ mm.

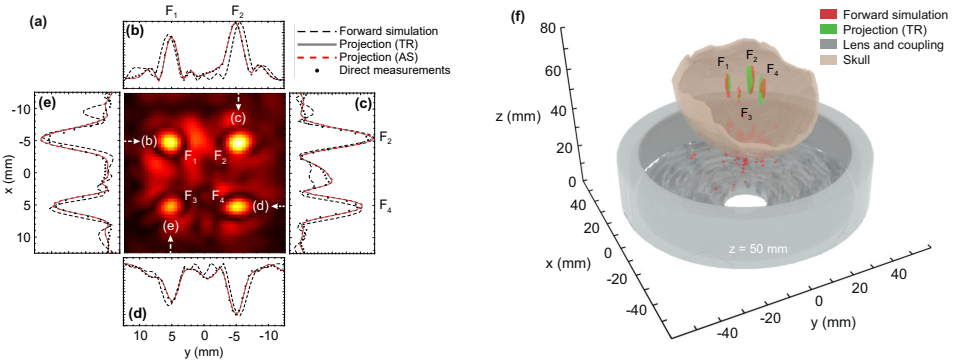

Figure 7.4: (a) 2D plane at the peak pressure for the time-reversal field (at $z = 63$ mm) of the four-foci lens with linear cuts over each focus maximum for simulation, experiment, time-reversal (TR) and angular-spectrum (AS) over (b) y-axis for F_1 and F_2 foci, (c) x-axis for F_2 and F_4 foci, (d) y-axis for F_3 and F_4 foci, and (e) x-axis for F_1 and F_3 foci. (f) 3D representation of the simulated and time-reversed (TR) field of the four-foci lens and its location relative to the skull.

All measurements had a spatial resolution of 0.5 mm, matching the simulation resolution. Simulated and measured fields were spline-interpolated to 0.1 mm precision for a more accurate calculation of location, sizes and volumes of each focus. Volumes of each focus were calculated using an amplitude threshold of half the peak intensity.

In addition to transcranial measurements, projection methods were applied to estimate the acoustic pressure field at the exit surface of the lens. This was performed for both test cases in the water tank and in the absence of the skull. In this case, for each lens one xy plane measurement was performed at $z = 44$ mm, and from -50 mm to 50 mm in both x and y directions, using a spatial resolution of 1 mm. To ensure that the exit plane of the lens and the plane measurement were completely parallel, transformations to its coordinates' system were performed as described by [196].

7.4 Results

7.4.1 Four-foci lens

Direct measurements for the four-foci lens show four clear focal spots, matching the design locations. By driving the transducer at 0.1 V peak before the amplification, the peak pressure is 0.12 MPa at the focus F_2. Focus F_1, F_3 and F_4 present a peak pressure of 0.1, 0.08, and 0.09 MPa, respectively. Figures 7.3 (a-d) show the transverse field,

$p(x, y)$, at $z = 63$ mm (at the location of the foci), obtained by forward simulation, projection using time-reversal and angular spectrum, and direct measurements, respectively. Figures 7.3 (e-h) show the corresponding sagittal planes, $p(y, z)$, at $x = 5.6$ mm (at the location of the focus F_1). All the measuring methods provide similar results. In particular, the fields calculated using the projection techniques are almost identical, with differences well below $< 1\%$. Direct measurements also match the field obtained using both projection techniques. The maximum field difference between direct measurements and projections, and through the focal region (defined as the region from -8 to 8 mm in both x and y directions and from 52 to 17 mm in z) is 9.4%, with a mean difference value of 1.4%. Comparing the direct measurement at the xy plane and the result of the time-reversal projection (from -8 to 8 mm in both x and y directions), we get that mean difference over this plane is 5.8% (5.9% when comparing with angular spectrum), where minimum differences are found in the foci region ($< 3\%$). Resemblances in terms of focal spot location and their lateral and axial dimension are summarized in Table 7.1. The maximum difference in the peak pressure location is 1 mm in the z direction for the focus F_1 and between experiment and both projection techniques. Lateral dimensions of all four foci are similar between experiment and projections, with maximum differences of 0.2 mm. The maximum difference is found in the z direction, where there exist a discrepancy of 1.5 mm in the axial FWHM at the focus F_2.

Figure 7.4 (a) shows a detailed field cross-section over the 4-foci. Comparing experiment with simulation, there exist a discrepancy in the peak pressure location, which is evident at insets Figs. 7.4 (b-e). The maximum focal shift in the y-direction appears for focus F_3, where a displacement of 2.3 mm is observed between forward simulation and direct measurements. In general, all foci in forward simulation appear further apart in x and y directions than in experiment and projection techniques.

Volumes were not characterized by direct measurements due to time and computational storage limitations. Instead, 3D fields are calculated by projecting the measured field using time-reversal or angular spectrum methods. In addition, forward simulations are inherently 3D. Figure 7.4 (f) shows a 3D rendering of the forward simulated and projected fields, where isosurfaces are obtained by using a threshold of $I = I_{\max}/2$. Both projection methods results in a very similar 3D field. Using forward simulations, the volume corresponding to each focal spot, from F_1 to F_4, are 17.1, 21.6, 25.1, and 16.5 mm^3, respectively. For time-reversal projection, volumes are 18.7, 17.4, 21.8, and 13.4 mm^3, while for angular-spectrum projection these values are 18.2, 17.2, 21.1, and 13.4 mm^3, respectively.

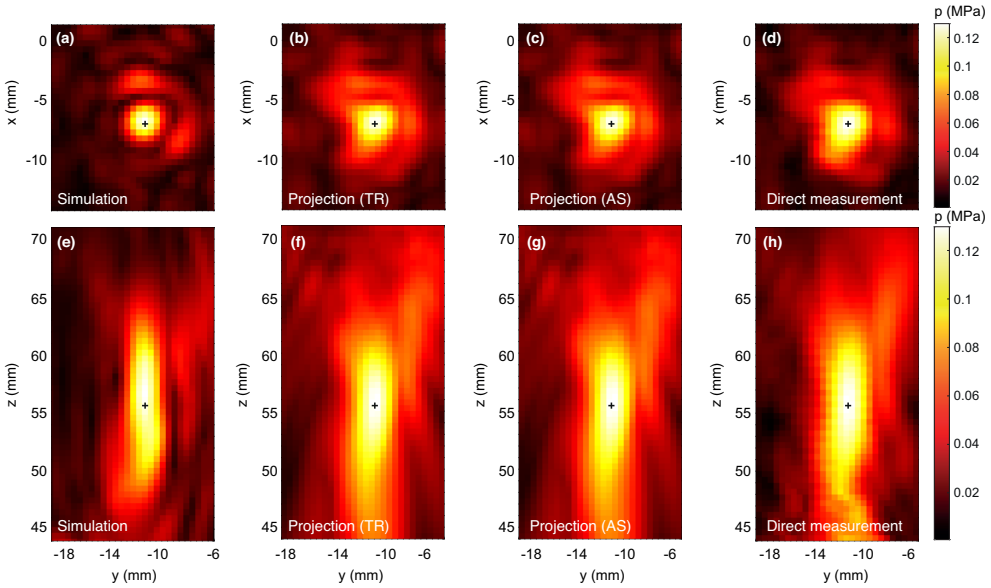

Figure 7.5: Transverse field, $p(x, y)$, for the preclinical lens at $z = 63$ mm for (a) forward simulation, (b) time-reversal projection, (c) angular spectrum projection and (d) direct measurement. Axial field, $p(y, z)$, for (e) forward simulation, (f) time-reversal projection, (g) angular spectrum projection and (h) direct measurements.

7.4.2 Preclinical lens

For the preclinical lens, direct measurement presented a maximum pressure value of 0.13 MPa while driving the transducer at 0.1 V, while for both time-reversal and angular spectrum projection this value was of 0.126 MPa, and 0.128 MPa, respectively. Figures 7.5 (a-h) graphically compares xy and yz planes over the maximum for forward simulation, time-reversal and angular spectrum projection, and direct measurements. Over the focal region (defined as the region $-12 < x < -2$ mm, $-16.5 < y < -6.5$ mm, and $45 < z < 66$ mm), the mean field difference between the two projection techniques is 1.5%, while the maximum local difference is 22%. Comparing direct measurements at the xy plane and time-reversal projection the mean field difference is 10.6% (10.3% when comparing with angular spectrum). Table 7.1 shows several quantitative metrics, e.g., the location and amplitude of the acoustic focus, for the four techniques. Peak pressure location is very similar for both projection techniques, but between direct measurements and projection methods there exist a difference of 0.5 mm in the z direction. Lateral dimensions are similar between direct measurements and projection methods (see Table 7.1). However, note that longitudinal dimension could not be estimated by direct

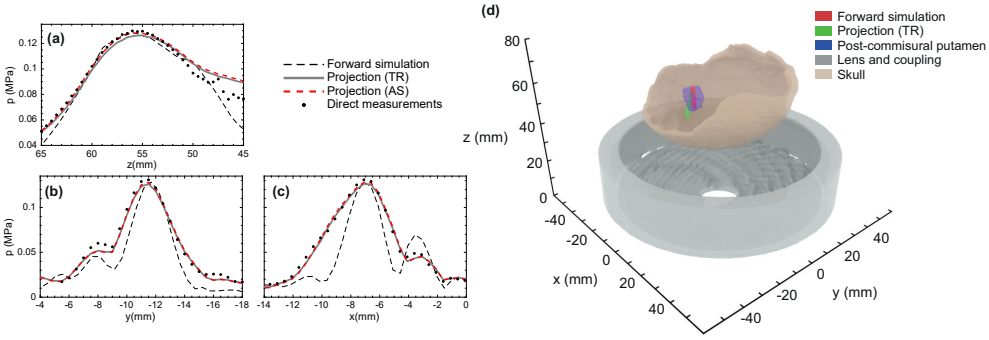

Figure 7.6: Linear cuts of the preclinical lens acoustic pressure for simulation, time reversal (TR) projection, angular spectrum (AS) projection and direct measurements in (a) the z direction, (b) the y direction and (c) the x direction. (d) 3D representation of the simulated and time-reversed (TR) field of the preclinical lens and its location relative to the skull and the post-comissural putamen.

measurements due to the proximity of the hydrophone to the skull, which introduced strong reflections. In this case, projection techniques allow reconstructing the acoustic field close to rigid boundaries. Indirect reconstruction strategies also avoid possible artefacts that may appear due to reflections with the measurement device.

Comparing experimental techniques with forward simulation, lateral and longitudinal dimensions of the focus show discrepancies. Figure 7.6 (a-c) shows a detailed picture of the peak pressure along the three axis, respectively. While the FWHM obtained by time-reversed projection is $5.3 \times 4.3 \times 27.7$ mm^3, simulated field is $3.1 \times 3.2\times$ 16.5 mm^3. The 3D rendering shown in Fig. 7.6 (d) compares the target structure, the reconstructed field by forward simulation, and the field reconstructed by TR projection method. The corresponding 3D volumes are 91.2 mm^3 for time-reversed projection, while 21.4 mm^3 for forward simulation. As the focus was designed to target the left post-commissural putamen, we have evaluated the volume of the target that was sonicated and the amount of energy that lied inside and out of the target structure. The target structure had a volume of 331.8 mm^3. The sonicated volume of the target, in simulation, was of 15.5 mm^3, with 72.4% of the focus lying within the target. With projection, the sonicated volume of the target was of 30.3 mm^3, with 33.3% of the focus lying within the target.

Table 7.1: Results for the four-foci lens and the preclinical lens acoustic fields

		4 foci lens				Preclinical focus
		Focus 1	**Focus 2**	**Focus 3**	**Focus 4**	
Coordinates (mm)	Simulation	(-6.1,5.1, 64.5)	(-5.1, -5.1, 63.5)	(6.1, 6.1, 62.5)	(5.1, -6.1, 64.5)	(-7.1, -11.6, 55.9)
	Experiment	(-4.9, 5.2, 63)	(-4.9, -5.2, 63)	(5.1, 4.8, 62)	(5, -5.2, 63.5)	(-7.1, -11.5, 56)
	Time reversal	(-5, 5.2, 64)	(-5, -5.2, 63.5)	(5, 5.2, 62.5)	(5, -5.2, 63.5)	(-7.1, -11.5, 55.5)
	Angular spectrum	(-5, 5.2, 64)	(-5, -5.2, 63.5)	(5, 5.2, 63)	(5, -5.2, 63.5)	(-7.1, -11.5, 55.5)
Peak press. (MPa)	Simulation	0.103	0.119	0.078	0.093	0.131
	Experiment	0.101	0.117	0.077	0.091	0.131
	Time reversal	0.102	0.116	0.077	0.092	0.131
	Angular spectrum	0.103	0.119	0.078	0.093	0.131
FWHM-x (mm)	Simulation	3.2	3.1	3.0	3.5	3.1
	Experiment	3.0	3.1	3.1	2.5	5.3
	Time reversal	3.0	3.2	3.1	2.4	5.3
	Angular spectrum	3.0	3.1	3.0	2.4	5.2
FWHM-y (mm)	Simulation	3.1	2.9	3.2	2.9	3.2
	Experiment	3.1	3.4	3.2	3.6	4.3
	Time reversal	3.2	3.4	3.2	3.8	4.3
	Angular spectrum	3.2	3.4	3.1	3.8	4.3
FWHM-z (mm)	Simulation	16.7	15.5	15.9	16.6	16.5
	Experiment	-	17.2	17.5	16.1	-
	Time reversal	20.2	15.6	17.6	15.3	27.7
	Angular spectrum	21.3	15.9	17.3	15.3	27.6
Volume (mm3)	Simulation	17.1	21.6	25.1	16.5	21.4
	Experiment	N/A	N/A	N/A	N/A	N/A
	Time reversal	18.7	17.4	21.8	13.4	91.0
	Angular spectrum	18.2	17.2	21.1	13.4	91.4

7.4.3 Holographic lens characterization

In order to understand the obtained differences between simulation and experimental results, projection techniques were also applied to evaluate the acoustic field at the exit surface of the holographic lens. This was compared with the phase map obtained with simulation (also performing projection) and the phase map used to design the lens. The experimental field was back-projected from the measured plane to the curved lens exit surface (see Fig. 7.2). The simulated field was obtained by performing one simulation in the absence of the skull, recording all the signals at a plane located 44 mm above the transducer with lateral dimensions of 100×100 mm^2 to match the same experimental measurement plane, and performing a time-reversal simulation. For the sake of simplicity, we only show the preclinical lens.

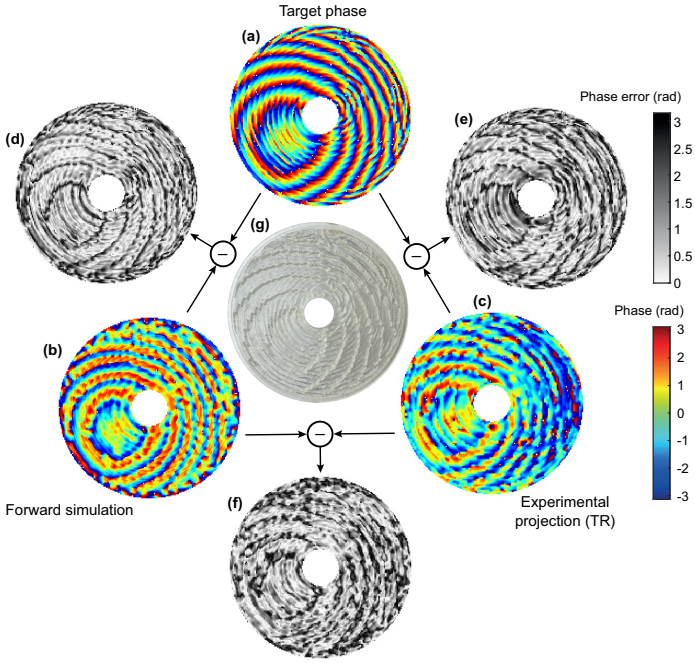

Figure 7.7: (a) Recorded phase at the holographic plane for which the preclinical lens was designed. (b) Simulated phase after projection. (c) Experimental projected phase. (d) Difference between the goal and the simulated phases. (e) Difference between the goal and the experimental phases. (f) Difference between the simulated and the experimental phases. (g) Photo of the 3D printed lens.

Figures 7.7 (a, b, c) show the target, simulated and experimental phase at the exit surface, respectively. We can observe concentric Fresnel rings in all phase maps indicating the focusing of the wavefront. However, the simulated and experimental phase map does not exactly match the target phase map at every location. These local errors, shown in Figs. 7.7 (d,e), are larger at phase jumps and at the areas far from the focal spot, where Fresnel rings and its corresponding phase jumps are tighter. In this way, this analysis show that the target phase is not perfectly encoded by the physical hologram design, with each pixel having a different height, as shown in the photograph Fig. 7.7 (g). The error between the target phase and the simulated phase map, Fig. 7.7 (d), follows a normal distribution with mean value of 0.014 radians and standard deviation of 0.85 radians. Comparing the experimental and target phase, Fig.7.7 (e), the mean error is 0.012 radians and standard deviation of 0.85 radians. Finally, between the simulated phase and the experimental projection, Fig.7.7 (f), we find a difference with a mean value of 0.024 radians and standard deviation of 0.88 radians.

7.5 Discussion

In this Chapter, acoustic holography has been used to experimentally estimate the complex 3D acoustic fields produced by holographic lenses. By performing experimental measurements in a transverse plane, these methods can provide volumetric acoustic fields. The methods have been applied to estimate the field inside an ex-vivo skull cap, opened in one side. Two different methods have been compared: time-reversal and angular spectrum projection. Projection methods have been compared with direct hydrophone measurements and forward simulations. Two test cases have been investigated: first, a holographic lens to create four equidistant foci through the skull and second, a holographic lens to focus on the left post-commissural putamen of the macaque.

For the four-foci lens case, we have first compared differences between both holographic techniques, observing that on the volume around the four foci the mean difference in pressure amplitude is 1.4%. When comparing with the 2D direct experimental measurement, this mean difference becomes 5.8%. Also, the peak pressure of the four foci appear at the same location and have very similar shape. The full width at half maximum in all three dimensions show errors smaller than 0.2 mm. The full potential of these projection techniques is unleashed when calculating the full 3D field by performing just one experimental measurement, i.e., a transverse 2D plane. This approach allows calculating metrics such as the treated volume. For example, for the four foci lens, volumes were 19.2 $\pm$ 0.3 mm^3 (focus F_1), 18.0 $\pm$ 0.1 mm^3 (focus F_2), 22.9 $\pm$ 0.4 mm^3 (focus F_3) and 14.4 $\pm$ 0.1 mm^3 (focus F_4). Using the proposed experimental system, the transverse 2D plane required for projections is composed of a total of 4331 waveforms (2.17 GBytes), every acquisition takes 3 seconds on average (measuring, averaging and moving to next position), leading to a total measurement time of 3.5 hours. Note that to measure the whole 3D volume, i.e., $-12.5 < x < 12.5$ mm,$-12.5 < y < 12.5$ mm and $47 < z < 72$ mm, with the same spatial resolution (0.5 mm), one must perform a total of 125000 acquisitions, which would take 4.3 days. In terms of memory, the corresponding measurements would occupy 62.5 GBytes.

For the preclinical lens case, mean difference between both holographic techniques at the focus region is 1.5%, while comparing with the 2D direct experimental measurement, this mean difference becomes 10.6%. Also, the peak pressure of the focus appears at the same location and have very similar shape, where the average volume of the focus was 92.3 mm^3. Measurement time of the corresponding 2D transverse plane for projections (4736 measurements, 2.37 GBytes) is 4 hours. In contrast, acquisition of direct measurements over the whole volume ($14 \times 14 \times 27$ mm^3) will lead to a total of 42336 measurements, which would take 35.3 hours (21.17 GBytes).

Greater differences are found between holographic projection and forward simulation for both lenses. For the four-foci lens, foci F_1 and F_3 appeared 1 mm apart in the x-axis from the experimental location, and foci F_3 and F_4 had this same shift in the y-axis. Also, forward simulation focus volumes are 17% greater than the experimental ones on average, except from the focus F_1 where it has been experimentally obtained that it was 6% larger. For the preclinical lens, experimentally the focus appears approximately at the same location than in the simulation, whereas simulated focus volume was 75% greater than the experimentally determined, with a region of relatively high pressure close to the skull. Discrepancies between simulation and experiment in both cases might be due to differences in the simulated skull properties, mode conversions in the skull, positioning errors and differences between the designed and the final 3D printed lens.

While 3D direct measurements are feasible with modern acquisition systems, most hydrophones can vary their sensitivity during time, in particular, polymer polyvinylidenfluorid (PVDF) ones are susceptible to changes during several hours of immersion. In addition, some hydrophones are very large to be introduced in cavities, such as a skull cap, limiting its use for transcranial measurements. In these situations, holographic projection can help to measure with large, sensitive and broadband devices, such as membrane hydrophones or large needle hydrophones. Another advantage of projection techniques is less exposure of the hydrophone to mechanical and thermal damage, including cavitation damage, since the field outside the focal point usually present a weaker amplitude than when the hydrophone is located directly at the focal spot. Also, holographic reconstruction makes it possible to characterize the field at the exit surface of a lens, identifying the error between the target phase to be encoded and the phase recovered by the manufactured lens.

However, the projection methods presented in this Chapter are restricted to homogeneous media. Note the experiments were performed using a skull cap, rather than a full skull. In this sense, it will be difficult to estimate the field inside a closed cranial cavity by performing holographic projections. The time-reversal simulation strategy can be adapted to heterogeneous media by solving the constitutive equations considering spatially varying density, sound velocity and sound absorption maps. However, this would introduce uncertainties, as it requires precise knowledge of the properties of the medium and its location with respect to the holographic plane.

7.6 Chapter conclusions

In this Chapter we have used holographic techniques, first, to create acoustic holographic lenses and, then, to evaluate their performance. In this way, time-reversal and angular spectrum projection methods were applied to obtain the whole volumetric field produced by an acoustic holographic lens focusing through an ex-vivo macaque skull cap. Results show that projection methods are equivalent to direct measurements, whereas the former require only a single 2D-plane measurement. This strategy saves significant measurement time and memory requirements, especially when evaluating the complex field produced by acoustic holograms. Furthermore, this indirect procedure also mitigates signal artefacts that may appear during direct measurements due to the experimental setup. For example, in the studied cases we avoided bringing the hydrophone too close to the surface of the skull to avoid interferences due to bone-sensor reflections.

In addition, since phase-only holograms suffer from diffraction at the edges, corresponding with phase jumps at the central frequency, they cannot perfectly encode the target phase. Other sources of error, like tolerance of the 3D printing, positioning, coupling with the transducer, etc, also produce discrepancies between the target phase and the actual phase distribution generated by the lens. In this way, holographic reconstruction techniques emerge as a fundamental tool to experimentally recover the actual phase at the exit surface of the lens and compare it with the theoretical phase required for a particular design. This procedure can also help to design, tune and test novel hologram topologies to go beyond the limitations of current phase-only holograms, which is of great interest for low-cost therapeutical ultrasound systems and other emerging applications of acoustic holograms that involve the accurate synthesis of complex acoustic fields.

Publications

The contents of this Chapter have been presented in the following publications:

Journal papers

Andrés, D., Carrión, A., Jiménez, N., & Camarena, F. (2023). Methods to design and evaluate transcranial ultrasonic lenses using acoustic holography. Physical Review Applied, 20(4), 044071.

Conference papers

Andrés, D., Carrión, A., Lamothe, N., Pineda-Pardo, J. A., Jiménez, N., & Camarena, F. Design and Holographic Field Reconstruction of Ultrasonic Lenses for Drug Delivery in Non-Human Primates. *2022 IEEE International Ultrasonics Symposium (IUS)*. Venice, Italy. October 10-13, 2022. Published in *2022 IEEE International Ultrasonics Symposium (IUS) (ISBN: 978-1-6654-6657-8)*.

Andrés, D., Carrión, A., Lamothe, N., Pineda-Pardo, J. A., Jiménez, N., & Camarena, F. Hologramas acústicos para la administración localizada de fármacos en el cerebro: validación ex-vivo en primates. *TECNIACUSTICA 2022. 53 Congreso Español de Acústica. XII Congreso Ibérico de Acústica*. Elche, Spain. November 2-4, 2022. Published by *Sociedad Española de Acústica-SEA (ISBN:978-84-87985-32-4)*.

Chapter 8

Preclinical holographic ultrasound system for blood-brain barrier opening

Holographic lenses have recently started to be used in-vivo with small animals with great success. However, whether they are a good option for humans should be studied, beginning with previous experiments in non-human primates. In this chapter we present a low-cost preclinical system based on a moderately focused transducer, a holographic lens, a passive cavitation detector and an optical guidance system. This particular device is designed for blood-brain barrier opening at specific locations into a macaque's brain. The system was designed and calibrated, with the results showing that it fulfils the specifications for drug-delivery applications.

8.1 Introduction

Blood-brain barrier opening (BBBO) has become one of the main therapeutical objectives when focusing low-intensity ultrasound inside the brain, due to the potential of ultrasound to locally disrupt this protective system of the brain unlike any other technique. Before ultrasound was proposed for this purpose, drugs were usually delivered using gene medicines or recombinant proteins as carriers, and even injecting directly the drug into the brain [197, 198]. Even some chemicals were discovered to open the barrier,

but in all these cases the opening was observed in all the brain and not just in the area of interest [199]. It was known from time ago that ultrasound could perform this same effect but in a localized manner and without any damage to the tissue [26], even monitoring the therapy during in-vivo experiments with animals via the stable cavitation of ultrasonographic contrast agents [17]. Detection of the success of the intervention was firstly performed with histology [200] and afterwards using MR imaging with magnetic contrast agents that were perfused into the regions where the barrier was opened [17].

Disrupting this barrier allows introducing therapeutic and contrast agents inside the brain, but also permits the entrance of pathogens. With ultrasound, the inactivation of this protective system is temporary, with mean recovery times of hours, normally being completely recovered after 24 to 48 hours as evidences in rabbits and non-human primates have demonstrated [17, 154]. Also, it has been proven that the closure times of the BBB is independent of the volume of the region affected [201].

Many recent studies of BBBO have been performed in small animals [202], and large animals like dogs [203] and non-human primates [204], even in an awaken state where no anaesthesia was needed [205]. In humans, disruption of the BBB has already been successfully performed by Abrahao et al. with a phased-array system guided with magnetic resonance imaging [206].

With animals, delivering ultrasound using single-element transducers can be convenient for their ease of use and less cost. However, the focal spot of the transducer is fixed and just one focus can be performed at a time. Large or multiple location openings require several microbubble administration procedures. Some studies with non-human primates using commercial MRI-guided phased-array systems for humans have been done [207], but the access to this instrumentation is often complicated. Holographic 3D-printed lenses have already been used to perform bilateral BBBO in small animals as an alternative to phased-array systems [65, 66]. These systems were tested in mice using a single-element transducer coupled to a 3D-printed hologram designed to produce sharp, quasi-spherical and bilateral focal spots close to the diffraction limit [65], or elongated focal spots covering a narrow and large area [66].

In this Chapter, a system to open the blood-brain barrier in non-human primates with optical guidance and real time cavitation monitoring is developed. The final aim of this system is to perform a feasibility study of using acoustic lenses coupled to a large-aperture and slightly focused transducer, with the long-term goal to disrupt the blood-brain barrier in a macaque's brain. The system is calibrated and the acoustic targeting accuracy quantified combining simulations and ex-vivo experiments. To do so, seven different locations have been chosen to sonicate, three at the left caudate nucleus and four at the right hemisphere cortex. The results show that the system fulfils design specifications,

and the final outputs are lens design protocols and the instrumentation itself, which is calibrated and ready to use for future in-vivo experiments, planned to be performed in collaboration with Dr. José Obeso and José A. Pineda at HM-CINAC (Madrid, Spain).

8.2 Materials and methods

8.2.1 System specifications and subsystem design

The therapeutic system consists in several subsystems. The ultrasound generation subsystem uses a moderately-focused ultrasound transducer, based on a single-element spherical cap piezoelectric ceramic, an arbitrary signal generator and a power amplifier. The focusing subsystem is based on acoustic holograms, and consist in a 3D-printed holographic lens using the curvilinear hologram topology. The lens is coupled to the transducer with coupling gel, and a water-coupling system was 3D-printed, consisting in a 3D-printed holding cone, a water bladder and a water conditioning unit for temperature control and degassing. The positioning subsystem is based on a commercial optical guidance, consisting in a stereoscopic camera, and calibration and tracking constellations, integrated in a neuronavigation software. Finally, the acoustic monitoring for BBBO applications is based on a passive cavitation detector, consisting in a confocal flat single element ultrasound transducer, a data acquisition system, and a computer used for control and real-time post-processing. A diagram summarizing these systems is shown in Figure 8.1.

8.2.2 System constraints

Single focal spot lens

Some system specifications result in constraints that must be fulfilled by the rest of the subsystems. First, the passive cavitation detector (PCD) for real time monitoring is located at the centre of the main ultrasound transducer, in a confocal configuration. The PCD presents a narrow directivity and beamwidth to increase its sensibility in reception mode. Therefore, the acoustic focal spot needs to be aligned with the system axis. Note that, in this particular configuration, if a hologram is used to target several focal spots at once, this will result in a loss of calibration for the off-axis detected cavitation signals. In order to maintain the calibration of the passive cavitation detector, it becomes convenient that the therapeutic target lies at the axis of the system, also aligned with the axis of the

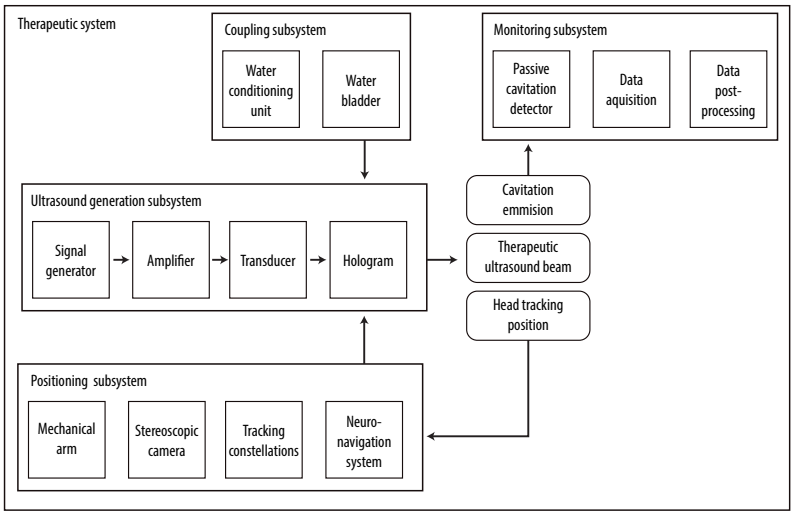

Figure 8.1: Diagram of the subsystems forming part of the whole therapeutic system

PCD and the ultrasound transducer. As a result, single focal spot lenses will be used for this particular system.

Target specific lenses

The system must be able to perform several sonications in different targets with various power levels. In addition, the maximum sedation time for macaques is limited to about three hours.If target specific lenses are used, the lens must be changed after each sonication. This includes the lens replacement procedure, filling the water bladder, conditioning the water, optical tracking calibration and positioning. This process, for this particular system, takes around 30 minutes. Total time is mainly defined by lens replacing time and treatment time per sonication. A post-treatment MRI must be acquired in BBBO protocols to confirm BBB disruption by gadolinium extravasation, which takes at least 45 more minutes. As a result, and if target specific lenses are used, we estimate that these constraints limit the number of sonications per sedation to two sonications. Therefore, for this particular system, we cannot afford to change the lens for each target. To overcome this constraint, a general-purpose lens was designed, targeting at a distance of 50 mm from the transducer surface in free water, and their validity and focus quality, i.e. possible aberrations, were studied when focusing at all the intended targets.

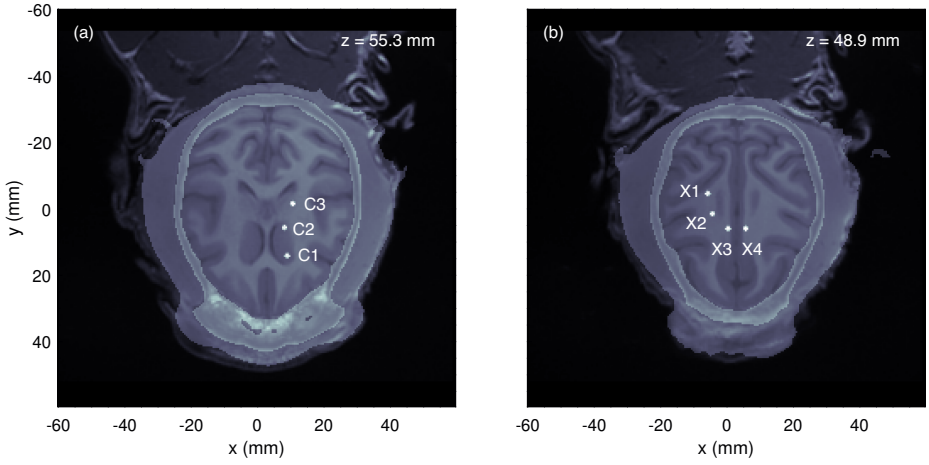

Figure 8.2: (a) Target locations at the caudate nucleus inside the brain. (b) Target locations at the cortex inside the brain.

8.2.3 Lens design

A first approach was studied, setting a virtual source at each desired location and computing an aberration-corrected lens for each target. The targets were three points at the left caudate nucleus (Figure 8.2 (a)) and four points in the right hemisphere cortex (Figure 8.2 (b)). Considering the centre of the transducer as the coordinates' origin, the caudate target points were C1 (8.6, 14.2, 55.3) mm, C2 (8.1, 5.6, 55.3) mm and C3 (10.2, -1.5, 55.3) mm, whilst the four points at the cortex were X1 (-6.1, -4.6, 49.8) mm, X2 (-4.6, 1.5, 49.8) mm, X3 (0, 5.6, 49.8) mm and X4 (5.6, 6.1, 49.8) mm. The lens was designed after the head was rotated and translated as described in the previous section, so this lens is just used to bring the focus of the transducer to the desired depth and compensate phase aberrations. Each lens was designed for a focused transducer as explained in Chapter 2, locating a virtual source at the coordinates of each target and performing the back propagation considering the skull.

8.2.4 Experimental setup

On the one hand, we have performed calibration measurements in a water tank with the same experimental setup and ex-vivo macaque skull as in Chapter 7 (Figure 7.2). First, the focal point of the lens was located measuring the acoustic field with the hydrophone and then evaluation of the acoustic pressure at this maximum was performed at voltages from 50 to 450 V in 50-Volts steps. Second, the skull was mounted on its holder and the same procedure was followed, making pressure measurements for an identical voltage sweep.

On the other hand, the setup for future in-vivo experiments was designed in the laboratory, and consisted on a therapy system, a monitoring system and an optical positioning system. The therapy system consisted on the same focused transducer described in Chapter 7 (a custom-made high-intensity ultrasound transducer with outer diameter $OD = 100$ mm and radius of curvature $R = 140$ mm, with an inner aperture diameter of $ID = 20$ mm and central frequency $f = 500$ kHz) to which the lens is coupled, and a 3D-printed cone with two orifices to attach tubes to fill a water bag that will be used as the coupling medium between the transducer and the macaque's head. The two tubes are connected to a water conditioning unit (WCU-Series, Sonic Concepts, USA) to ensure constant degassed-water flow. High-temperature water-insoluble coupling gel (Sonotech Sono 600) was used to ensure constant coupling of the lens to the transducer during experiments. The transducer was driven using a USB oscilloscope with integrated function generator (Handyscope HS5, TiePie engineering) and amplified by a 400-Watts amplifier (E&I Ltd, USA) with a 50-Ohm impedance matching network to maximize power transferred from the amplifier to the transducer.

The monitoring system consisted on a piezoelectric PCD (V382-SU, Olympus) with a central frequency of 3.5 MHz and a bandwidth (- 6 dB) of 65.17% placed in the central hole of the transducer and aligned with it. This system captures the signal emitted by microbubbles' cavitation, allowing a real-time evaluation of the therapeutic effect. The cavitation signal was acquired with the same USB oscilloscope used to generate the signal. A program was designed to control the emitted signal and allow real-time monitoring of the bubbles' activity.

The optical positioning system was a commercial TMS neuronavigation system (Brainsight, https://www.rogue-research.com/) adapted to our custom transducer. The optical positioning system consisted on a camera, two constellations that the camera was able to recognize and know their relative coordinates, and a calibration piece which marks the central coordinates of the transducer. One constellation was fixed to the transducer and the other constellation was attached to a fixed point of the macaque i.e its stereotactic frame or the table. A training on how to properly locate the transducer relative to the

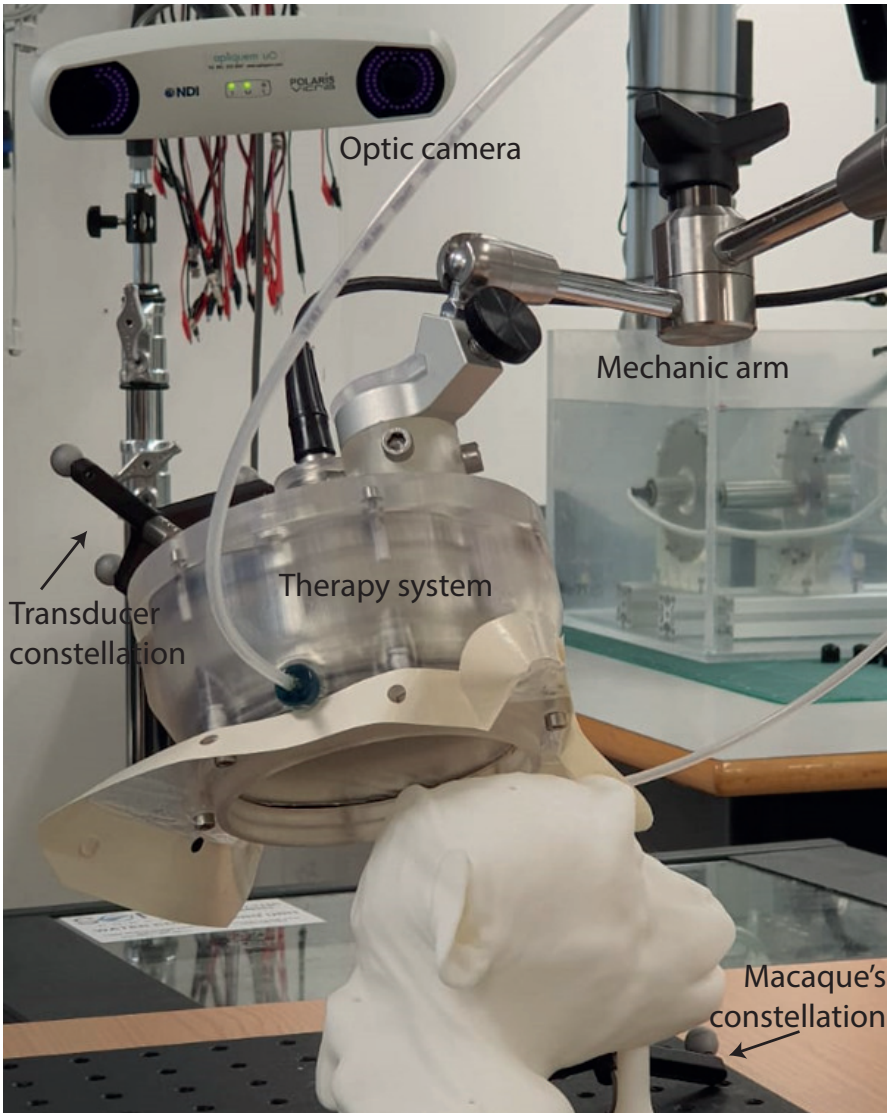

Figure 8.3: Experimental system for in-vivo experiments.

head using this system was performed using a 3D printed head of the macaque and its CT information. The transducer is attached to a mechanic arm with full range of movement to allow its manual positioning. The setup is shown in Figure 8.3.

To minimize possible aberrations, the transducer was located as normal as possible with the macaque's head surface. To do so, an algorithm was designed. This algorithm uses the optimization toolbox of MATLAB to find the optimal transducer location that is located normal to the head surface and targeting at the desired location. The `fmincon` built-in algorithm is used. The input data of the algorithm is the segmented tomographic data of the skull, the target location, and the transducer geometry. The output is the transducer location and its orientation, and this data is used as the input for the neuronavigation subsystem. Note that, using in this procedure, the PCD would be also aligned to record all the cavitation signals.

8.2.5 Experimental protocol design

In order to perform the BBB disruption in the brain of a macaque, first an MRI image must be performed for the specific specimen. In this image, the segmentation of the areas to be treated must be carried out. Also a CT image is needed to design and test the performance of the lenses as this image contains the main information of the physical properties of the skull and brain. The lens will be designed performing computational simulations and will be 3D printed using stereolithography methods. Simulation parameters of the specific location of the skull and the transducer-lens system must be loaded into the neuronavigation system to pre-plan the experimental conditions. To perform the in-vivo experiment, first the macaque will be sedated and with all the necessary monitoring systems in place. The animal's head will be located in a stereotactic frame with the neuronavigation tracking constellations fixed on it to ensure no movement of the macaque and that the therapy will be performed accurately where it was designed to be. The transducer will be mounted with the lens, the monitoring system and the coupling medium, ensuring the water inside the cone is in optimal conditions, i.e. without any bubbles. With the animal sedated and in the stereotactic frame, the calibration of the neuronavigation system will be done. Once this is performed, the transducer will be located in the correct position to target one of the specified locations and perform a first sonication with the treatment parameters but without microbubbles injection to obtain an acoustic baseline signal in the PCD. The chosen treatment parameters were burst length of 10 ms, repetition frequency of 1 Hz and a total duration of 100 s, inspired in the work of N. McDannold [208]. After the baseline will be obtained, an injection of microbubbles at concentration of 20 μL/kg diluted in 5 mL of phosphate buffered saline (PBS) will be be continuously injected by using an infusion pump at an infusion rate of 0.02 mL/s. In these conditions, several sonications at the defined powers and locations will be performed, ensuring microbubbles are being continuously injected and the animal is in perfect conditions. Once sonications are finished, the macaque will be transferred to the MRI facility. An injection of gadolinium will be administered and, immediately, a T1-MRI protocol image will be obtained to assess the blood-brain barrier opening. After

24 hours of this procedure, another T1-MRI protocol image with gadolinium injection will be done to study the closure of the blood-brain barrier.

8.3 Results

8.3.1 Lens performance

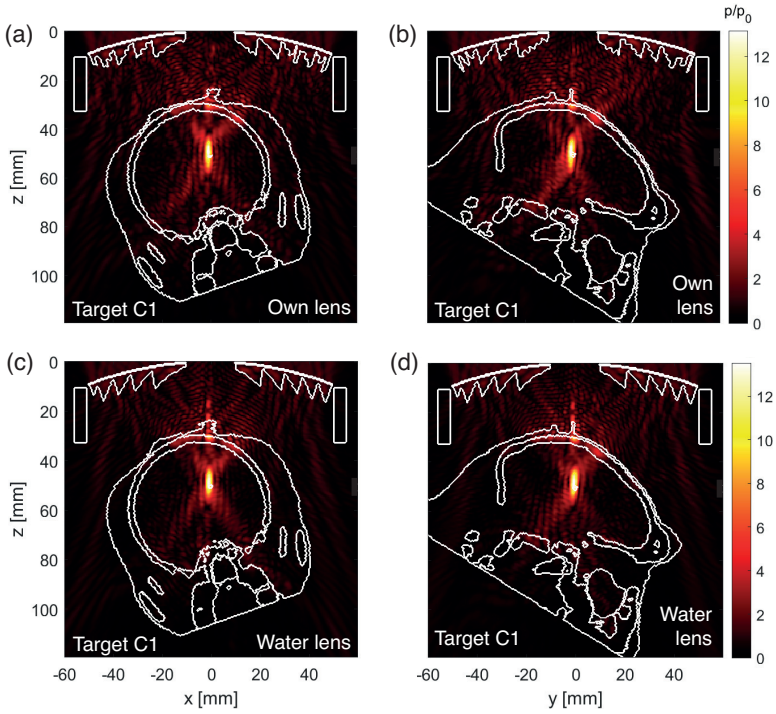

Figure 8.4: Comparison of an aberration-corrected lens for target C1 in a (a) transversal cut and (b) sagittal cut, and the generic lens in a (c) transversal cut and (d) sagittal cut.

First, a comparison between the performance of the aberration-corrected lenses and the water lens is studied for the three targets at the caudate nuclei. A comparison for targets C1 and C3 are shown in Figure 8.4 and Figure 8.5, respectively. In these examples it can be seen that both gain and focus shape differ very little. For target C1, maximum pressure gain, defined as the ratio between the pressure at the transducer's surface and at the focus, with its aberration-corrected lens, is 12.8, whereas with the generic water lens is 12.7. For C2 and C3 the aberration-corrected lenses lead to a gain of 14.7 and

13.9, respectively, while the generic lens gives a gain of 13 and 13.4, respectively. Both aberration-corrected and generic lenses led to good-quality acoustic foci. At the view of these results, it is possible to use one single generic lens to treat all the therapeutic targets with a very similar gain at each location. For the cortex targets, with the generic lens gains were of 10.9 for target X1, 11.5 for X2, 10.4 for X3 and 9.5 for X4. Pressure gains were very similar in all cases, which results in an advantage for the in-vivo experiment. This ensures that a given voltage value will produce a very similar pressure value at any target studied, giving us confidence in the performance of a safe blood-brain barrier opening.

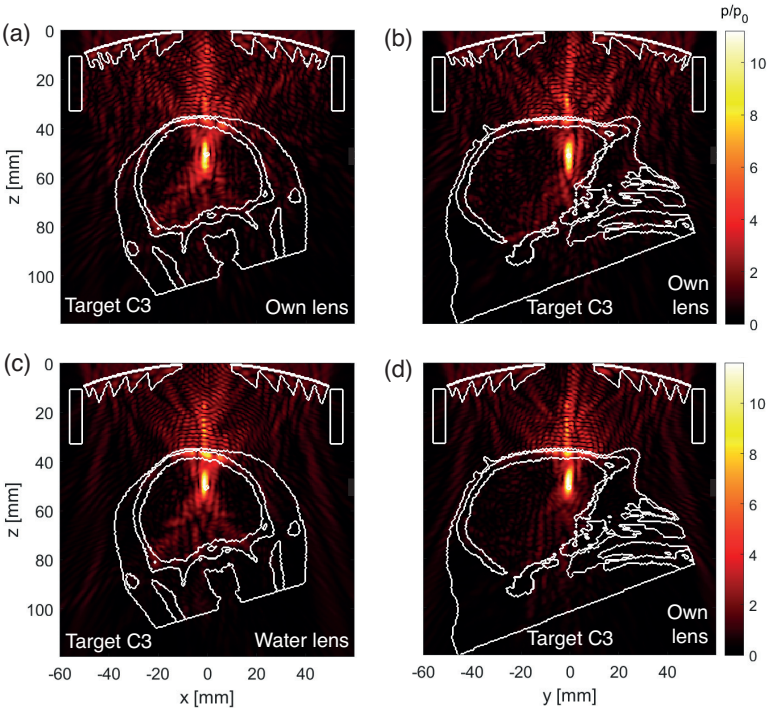

Figure 8.5: Comparison of an aberration-corrected lens for target C3 in a (a) transversal cut and (b) sagittal cut, and the generic lens in a (c) transversal cut and (d) sagittal cut.

8.3.2 Lens calibration

The calibration of the system gave nine experimental points. Both pressure values versus voltage for free water and through the ex-vivo skull were fitted to a quadratic polynomial. For the lens in free water, the resulting equation was P (MPa) = 5· $10^{-6}V^2$ + 5·$10^{-3}V$ - 2·10^{-2}, with voltage V values in mV. When the skull was located, the fitted equation was P (MPa) = 2·$10^{-6}V^2$ + 3·$10^{-3}V$ - 1.2·10^{-2}. All data points are represented in Figure 8.7. With this information, a derating factor between water and inside the brain can be approximately calculated as the ratio between the pressure in water and through the skull for each voltage pressure. In these measurements, the derating factor was 1.99 $\pm$ 0.05. Note that the brain is more attenuating than the water, so the pressure is presumably less than the obtained with the calibration. This gives us a safety margin when performing in-vivo experiments that the animal will not suffer any damage. Experimental and simulated normalized pressure values when focusing through the ex-vivo skull are shown in Figure 8.6

As the aim of the proposed in-vivo study is to evaluate the feasibility and safety of the system, three pressure values inside the brain were proposed to study in different targets of the brain: 0.25, 0.5 and 0.75 MPa. These pressure values, according to the calibration, correspond to input voltages of 90, 170 and 240 mV, respectively. Targets C1 and X1 will be treated at 0.25 MPa, targets C2, C3, X2 and X4 at 0.5 MPa and target X3 at 0.75 MPa.

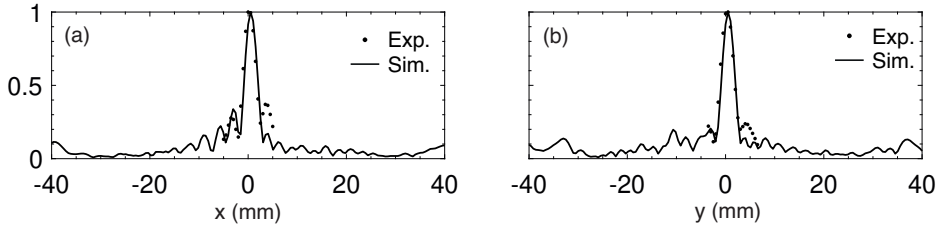

Figure 8.6: Measured (dots) and simulated (line) normalized pressure fields for the water lens through the ex-vivo macaque skull. (a) x-cut and (b) y-cut.

8.4 Chapter conclusions

In this last Chapter of the thesis we have designed a preclinical system to perform blood-brain barrier opening in macaques. Some subsystems impose constraints that were considered when designing the holograms and the rest of the system. First, the acoustic focus must be confocal with the PCD located at the axis of the transducer. Second, the

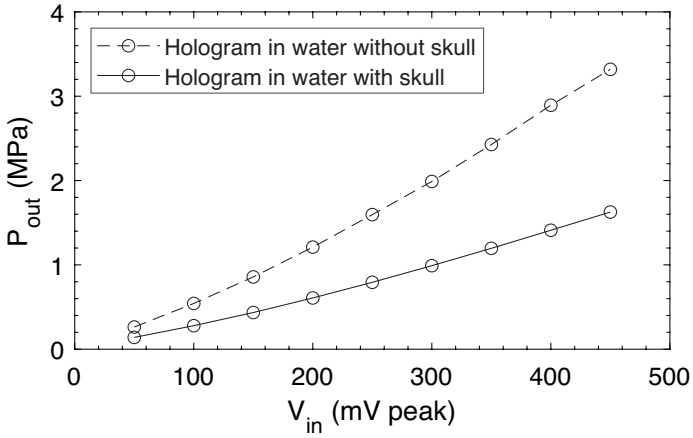

Figure 8.7: Pressure values given a voltage value to the system. Calibration in free water (dashed line) and through the skull (solid line)

sedation time estimated for in-vivo experiments may be shorter than 3 hours, limiting the system to perform a maximum of two lens changes during the procedure. Considering both constraints, a simulation study was performed to calculate the differences between aberration-correction lenses for each location and the use of a generic lens. Pressure fields and gains were very similar in both cases. Therefore, this study demonstrates the viability of using generic lenses in future in-vivo experiments with macaques. In particular, simulation and ex-vivo results show that this setup can be used to target up to seven locations to study the blood-brain barrier opening using the confocal real-time monitoring system. The resulting system is like having used a single-element focused transducer whose radius of curvature matches the desired targeting location. Nevertheless, the system was designed with that aperture and radius of curvature to be versatile for both non-human primates and humans, and to be able to target any possible structure inside the brain. This system calibration and future experiments are thought to get insight of the system characteristics and to be used in the future to create more complex holograms and even arrive to clinical trials.

To overcome the system constraints, passive cavitation mapping could be used instead of a single-element PCD. With this system, we could use one only lens to target several spots at the same time, as shown in Chapter 7. This might be more relevant for human applications, where, as demonstrated in previous Chapters, aberration correction is critical, and patient and target specific holograms are required. In addition, lateral and axial steering are encoded in these latter lenses, and, therefore, this facilitates the positioning

of the transducer when targeting multiple locations. Using multi-target holograms, the transducer must only be positioned once.

Other solution under investigation is the use of lenses to change the directivity of the PCD adapting it to the acoustic focus region.

As a future step in this system with the aim of saving positioning time and avoiding precision errors, a robotic arm with direct feedback from the neuronavigation system would be beneficial. This robot would locate the transducer at the same location as it was in the simulation in a faster and robust way, reducing the positioning errors and treatment time.

Publications

Contents related with this Chapter have been sent in the form of a manuscript and is in process of review

Journal papers

Lamothe, N., **Andrés, D.**, Carrión, A., Jiménez, N., & Camarena, F. (2024). Monitoring holograms for therapeutic ultrasound using passive cavitation beamforming. Sent to Applied Acoustics, in peer review process.

Chapter 9

Conclusions

This concluding chapter brings all the thesis conclusions together, highlighting the potentials, drawbacks and future work to be done in the development of acoustic holograms with the focus of making them feasible and attractive for clinics.

9.1 General discussion and conclusions

Throughout this thesis, new methods for designing acoustic holographic lenses have been presented, along with some potential applications for hyperthermia and brain therapies.

In the first part of the thesis, two methods for hologram generation were proposed and tested. The first method, presented in Chapter 2, allows designing holographic lenses that match the curvature of a focused transducer. Lenses made in spherical coordinates present pixels that are totally perpendicular to the transducer's surface and result in truncated pyramids. These lenses perform better in general, as there is no material between the transducer and the lens, as it would happen with a flat lens. The conditions in which this method fails were explored and its limitations quantified. We observed that when trying to use highly focused transducers and the lens was designed to focus acoustic energy further from their radius of curvature, the method fails, and bulky holograms can perform better than curvilinear holograms. Besides this uncommon situation, curvilinear holograms emerge as an efficient topology to modulate the acoustic field and produce sharp focal spots and acoustic images with the required accuracy for biomedical applications.

The holographic lenses described above were designed by recording the wave phase information in a single plane, usually called the holographic plane, in front of the transducer. Lenses made like this can focus further than they were supposed to because wavefront diffraction is not accurately encoded and the thin-lens approximation is not fulfilled. Therefore, in Chapter 3, we present a novel method for designing holograms by recording wave information in a volume rather than in a single plane. In this way, the lens encodes the full-wavefront information at the exit of the lens, instead of at the exit plane as in traditional holograms. By designing them for a single focal spot, we obtain lenses whose curvature coincides exactly with the shape of an ellipsoid, which is indeed the optimal solution for refracting lenses of high refraction index materials. In contrast, any of the traditional procedures result in lenses with a hyperbolic profile. Note that, for long focusing distances and limited apertures, both curvatures are similar because the wavefront curvature can be approximated as parabolic instead of spherical. However, for short focal distances, i.e., low f-number devices, phase-matching holograms are revealed as a more accurate lens topology. The limitations of this method were also explored. We observe that for materials whose sound speed is greater than the surrounding medium, this approach can result in an undetermined solution at some pixels. This phenomenon emerges when the axial component of the wavevector of the time-reversed wavefront in the host medium is equal to the one in the lens material. This phenomenon appears to be universal for any refracting hologram or lens composed of a refraction index material higher than one. We observe that this occurs even for lenses based on traditional holographic methods. Any of these lenses is able to codify these specific waves arriving at angles larger than the so-called critical angle. However, we observe that this problem does not occur when focusing at long distances or when using a lens with lower sound speed than the host medium.

Acoustic holograms have been explored to enhance ultrasound treatments such as hyperthermia. For the first time, acoustic holograms have been shown to produce thermal patterns inside an absorbing medium, such as soft tissue, as described in Chapter 4. With holographic lenses, a sharp acoustic image can be produced, and when applied to a tissue with absorbing characteristics this image turns into a heat pattern which is spatially modulated. We tested this concept using a 3D-printed hologram and a magnetic resonance-compatible transducer. Thermographic imaging using an infrared camera and magnetic resonance imaging thermometry were used to validate the spatially modulated thermal patterns produced in the bulk of phantoms and ex-vivo liver tissues. The device itself, a low-cost magnetic resonance compatible transducer coupled with a hologram, was revealed as a powerful and efficient tool to perform hyperthermia treatments inside any commercial MRI facility.

Moreover, we observe that after a long time heat transport mechanisms, such as diffusion, blur the image. This means that for long-time treatments, it is not the acoustic image that

should be tuned but instead its equivalent thermal pattern. As of now, when aiming for hyperthermia treatments, where long pulses or continuous signals are commonly used, it is necessary to make thermal simulations and to use the information of them to tune the acoustic hologram as an iterative process to make the most precise thermal pattern for a specific application. Indeed, this was explored in Chapter 5, where a uniform thermal pattern is produced by a non-uniform acoustic field. The system was tested to deliver a controlled and uniform thermal dose over several tumour spheroids and its viability was measured in-vitro. Results show that spatially-modulated ultrasound hyperthermia produces a significant effect on tumour spheroids as compared with controls or thermocyler heating. Results show that ultrasound is more effective at killing cells or reducing cell growth tan just heating when delivering the same thermal dose. As explored in this fifth chapter, ultrasound-induced hyperthermia using holograms is revealed as an attractive approach to treating cancer beyond current techniques. However, more preclinical and clinical research is needed in this field, and holographic lenses can help to perform faster and more efficient studies by simultaneously applying hyperthermia treatments to several large tumour targets.

The second application of acoustic holograms investigated in this thesis is brain therapy. Acoustic holograms are of great interest for transcranial ultrasound treatments because they can compensate for the aberrations introduced by the skull. Current technologies based on single-element transducers cannot take into account how the skull affects the focus, and the ones based on phased arrays can overcome this drawback but are not able to produce good quality acoustic images when moving away from their focal zone, in addition to their complexity and high cost. Acoustic holograms designed with time-reversal methods not only encode the information of the desired acoustic image, but also the skull aberrations introduced in the wavefront. In this way, curved and flat transducers with holographic lenses coupled to them can be used positioned at any bone of the skull and obtain a precise focus without lateral lobes or undesired focusing. One general problem of transmitting pressure waves through the skull is the local heating of it. In general, the thicker the bone is, the worse it is. This can turn into undesired skull, skin or brain heating. One solution to this is applying ultrasound from the temporal bone, the thinnest part of the skull, located at the temples. Results, presented in Chapter 6, show that using acoustic holograms from this region several structures of neurological interest can be treated, such as the thalamus. As explored, using acoustic holograms, skull aberrations produced by conventional focused transducers are corrected and the focus can be adapted to a specific target and even produce two bilateral focal spots to treat the thalamic nuclei in both hemispheres at the same time. The amount of skull heating is reduced compared with the same focusing through other skull bones, with the advantage for the patient of not needing to shave the area to be treated. Also, these lenses present good performance under small misalignments. Nevertheless, numerical results show that if the positioning error committed is high, the lens focus is completely

lost, and the same effect occurs when using the same lens for different patients. In this sense, the lack of adaptability of holographic lenses as a passive and non-reconfigurable element is their main drawback, although their low manufacturing cost makes them still worthwhile.

Holography is not only useful for designing acoustic images but also to measure pressure fields, as exposed in Chapter 7. With holography, a single-plane measurement can be turned into a full volumetric image provided that it is performed in free-field, i.e, without any absorbing or distorting medium that prevents the time-invariance from being fulfilled. This procedure is very useful to evaluate any holographic lens performance, no matter how complex its generated acoustic image is, saving measuring time and storage resources. Also, it allows acoustic field assessment in places where the hydrophone cannot reach for reasons of space or logistics, and even knowing if there are regions where pressure is higher than expected. Another strength of this technology with great potential is the evaluation of the acoustic field at the exit plane of the lens. In this way, these techniques can be used to evaluate and quantify how different is the obtained field from that the lens was designed to encode, and use this information in a reciprocal way to improve the lens design.

Finally, in the case of designing holograms for pre-clinical testing with animals, the problems mentioned above are, in general, not so important. As exposed in Chapter 8, numerical simulations reveal that when focusing inside a macaque's brain, a general-purpose lens can be used. In this particular case, the skull of the animal is small and thin, with an average thickness of 2 mm [209] compared with the average human skull thickness of 8 mm [210], so for ultrasound of therapeutical frequencies, around 500 kHz (with wavelength in the skull of 4 mm), the acoustic field is not very distorted. The results obtained in this eighth chapter support the hypothesis, and in this sense, holographic lenses are well-suited for in-vivo experiments with small non-human primates.

In summary, holographic lenses have great potential for precise and low-cost therapy both in soft tissues and inside the brain, where their ability to encode aberrations introduced by stiff layers such as the skull is fully exploited. There is still room to research both in new methods to design holographic lenses for a better encoding of the desired field, and in the use of the already developed technology applied in the biomedical field, with demonstrated successful experiments in small animals and non-human primates. I hope that this thesis will contribute to further progress in the design and application of holographic lenses and help to bring this technology to clinics as an effective and low-cost alternative to current technologies.

9.2 Future work

Future work must be focused on obtaining good quality volumetric acoustic images. All the work done so far aimed to obtain acoustic images in a transversal or axial plane. Transversal holograms are very visual and can generate good quality acoustic images in the plane where they are defined to be, but in general there is a lack of control of the energy that falls outside this plane. On the other hand, axial holograms have a good control of where the energy is delivered, but they can only tune the acoustic focus by enlarging it or generating specific acoustic beams, like Bessel beams, even not a precise control of the image is accomplished. Very recently, Melde et al. have shown the creation of 3D acoustic images with several transducers by employing Deep-Learning methods [56]. Future research on acoustic holograms must be directed into the design of better 3D holograms, exploiting the full potential of the new Artificial Intelligence algorithms, and, as a final objective, be able to compensate aberrations created by the skull to completely adapt the acoustic beam to the whole volume of a brain structure. These same algorithms could be used in applications where it is not only important to control the shape of the hologram but also its amplitudes in different regions, like varying the maximum acoustic pressure in BBBO applications to account for differences in grey and white matter, as has been recently explored in free field [83].

In this way, low-cost systems based on acoustic holograms would be a good alternative to the actual phased array systems, providing precise treatments in very short time without the need of very complex electronics. Volumetric holograms could be also obtained by encoding the full wave information, i. e., both phase and amplitude. More research should be done in printable acoustic metamaterials which are able to tune all this information into a simple prototype, by changing the shape of the pixels or by making lenses of different printable materials and in this way achieve independent and precise control of both phase and amplitude.

Another important improvement to make holographic lenses gain importance in clinics is managing to make them dynamically reconfigurable or build them in a very fast way, so that at the time of applying it, it could rapidly change the location and shape of the therapeutic focal spot. With the development of 3D-printing technology and new techniques for matter assembly I believe that quick manufacturing of holographic lenses would be possible even at the same medical facility. On-site manufacturing can help reduce fabrication, transportation and deployment costs, and help bring this technology to clinical practice.

Bibliography

[1] Robert Williams Wood and Alfred L Loomis. “XXXVIII. The physical and biological effects of high-frequency sound-waves of great intensity”. In: *The London, Edinburgh, and Dublin philosophical magazine and journal of science* 4.22 (1927), pp. 417–436 (cit. on p. 1).

[2] R Dyroff and J Horvath. “Ultraschallwirkung beim menschlichen Sarkom”. In: *Strahlentherapie* 75 (1944), p. 126 (cit. on p. 2).

[3] WJ Fry et al. “Production of focal destructive lesions in the central nervous system with ultrasound”. In: *Journal of Neurosurgery* 11.5 (1954), pp. 471–478 (cit. on pp. 2, 3, 9).

[4] L Bakay et al. “Ultrasonically produced changes in the blood-brain barrier”. In: *AMA Archives of Neurology & Psychiatry* 76.5 (1956), pp. 457–467 (cit. on pp. 2, 3).

[5] Frederick W Kremkau. “Cancer therapy with ultrasound: a historical review”. In: *Journal of Clinical Ultrasound* 7.4 (1979), pp. 287–300 (cit. on p. 2).

[6] Jane B Marmor, Douglas Pounds, and George M Hahn. “Clinical studies with ultrasound-induced hyperthermia 1, 2”. In: *Third International Symposium, Cancer Therapy by Hyperthermia, Drugs, and Radiation: A Symposium Held at Colorado State University, Fort Collins, Colorado, June 22-26, 1980; Sponsored by*

the National Cancer Institute...[et Al.] 82. US Department of Health and Human Services, Public Health Service, National. 1982, p. 333 (cit. on p. 2).

[7] Gail Ter Haar. "Therapeutic ultrasound". In: *European Journal of ultrasound* 9.1 (1999), pp. 3–9 (cit. on p. 2).

[8] Michael D Gray et al. "Focused ultrasound hyperthermia for targeted drug release from thermosensitive liposomes: results from a phase I trial". In: *Radiology* 291.1 (2019), pp. 232–238 (cit. on pp. 2, 46).

[9] Chi-Feng Chiang et al. "Pulsed-wave ultrasound hyperthermia enhanced nanodrug delivery combined with chloroquine exerts effective antitumor response and postpones recurrence". In: *Scientific Reports* 9.1 (2019), p. 12448 (cit. on p. 2).

[10] Lifei Zhu et al. "Ultrasound hyperthermia technology for radiosensitization". In: *Ultrasound in Medicine & Biology* 45.5 (2019), pp. 1025–1043 (cit. on p. 2).

[11] Nathan McDannold et al. "MRI evaluation of thermal ablation of tumors with focused ultrasound". In: *Journal of Magnetic Resonance Imaging* 8.1 (1998), pp. 91–100 (cit. on p. 2).

[12] Yao-Sheng Tung et al. "Contrast-agent-enhanced ultrasound thermal ablation". In: *Ultrasound in Medicine & Biology* 32.7 (2006), pp. 1103–1110 (cit. on p. 2).

[13] Yu-Feng Zhou. "High intensity focused ultrasound in clinical tumor ablation". In: *World Journal of Clinical Oncology* 2.1 (2011), p. 8 (cit. on p. 2).

[14] Zhiguang Chen et al. "Ultrasound-guided thermal ablation for hyperparathyroidism: current status and prospects". In: *International Journal of Hyperthermia* 39.1 (2022), pp. 466–474 (cit. on p. 2).

[15] Zhen Xu et al. "Histotripsy: the first noninvasive, non-ionizing, non-thermal ablation technique based on ultrasound". In: *International Journal of Hyperthermia* 38.1 (2021), pp. 561–575 (cit. on p. 2).

[16] Alissa Hendricks-Wenger et al. "Immunological effects of histotripsy for cancer therapy". In: *Frontiers in Oncology* 11 (2021), p. 681629 (cit. on p. 2).

[17] Kullervo Hynynen et al. “Noninvasive MR imaging–guided focal opening of the blood-brain barrier in rabbits”. In: *Radiology* 220.3 (2001), pp. 640–646 (cit. on pp. 2, 128).

[18] Meaghan A O’Reilly and Kullervo Hynynen. “Ultrasound enhanced drug delivery to the brain and central nervous system”. In: *International Journal of Hyperthermia* 28.4 (2012), pp. 386–396 (cit. on p. 2).

[19] Carmen Gasca-Salas et al. “Blood-brain barrier opening with focused ultrasound in Parkinson’s disease dementia”. In: *Nature communications* 12.1 (2021), p. 779 (cit. on p. 2).

[20] Pierre-François D’Haese et al. “β-Amyloid plaque reduction in the hippocampus after focused ultrasound-induced blood–brain barrier opening in Alzheimer’s disease”. In: *Frontiers in Human Neuroscience* (2020), p. 422 (cit. on p. 2).

[21] Ying Meng et al. “MR-guided focused ultrasound enhances delivery of trastuzumab to Her2-positive brain metastases”. In: *Science Translational Medicine* 13.615 (2021), eabj4011 (cit. on p. 2).

[22] Randy L King et al. “Effective parameters for ultrasound-induced in vivo neurostimulation”. In: *Ultrasound in Medicine & Biology* 39.2 (2013), pp. 312–331 (cit. on p. 2).

[23] Joseph Blackmore et al. “Ultrasound neuromodulation: a review of results, mechanisms and safety”. In: *Ultrasound in Medicine & Biology* 45.7 (2019), pp. 1509–1536 (cit. on p. 2).

[24] Nir Lipsman et al. “MR-guided focused ultrasound thalamotomy for essential tremor: a proof-of-concept study”. In: *The Lancet Neurology* 12.5 (2013), pp. 462–468 (cit. on p. 2).

[25] Mohammad Rohani and Alfonso Fasano. “Focused ultrasound for essential tremor: review of the evidence and discussion of current hurdles”. In: *Tremor and Other Hyperkinetic Movements* 7 (2017) (cit. on p. 2).

[26] HT Ballantine, Eugene Bell, and Jesus Manlapaz. “Progress and problems in the neurological applications of focused ultrasound”. In: *Journal of Neurosurgery* 17.5 (1960), pp. 858–876 (cit. on pp. 3, 128).

[27] Johannes Gruetzmacher. “Piezoelektrischer kristall mit ultraschallkonvergenz”. In: *Zeitschrift für Physik* 96.5 (1935), pp. 342–349 (cit. on p. 3).

[28] John G Lynn et al. “A new method for the generation and use of focused ultrasound in experimental biology”. In: *Journal of General Physiology* 26.2 (1942), p. 179 (cit. on p. 3).

[29] WJ Fry and FJ Fry. “Fundamental neurological research and human neurosurgery using intense ultrasound”. In: *IRE Transactions on Medical Electronics* 3 (1960), pp. 166–181 (cit. on p. 3).

[30] Hans Jaffe. “Piezoelectric ceramics”. In: *Journal of the American Ceramic Society* 41.11 (1958), pp. 494–498 (cit. on p. 3).

[31] Osama Al-Bataineh, Jürgen Jenne, and Peter Huber. “Clinical and future applications of high intensity focused ultrasound in cancer”. In: *Cancer Treatment Reviews* 38.5 (2012), pp. 346–353 (cit. on p. 3).

[32] Hao-Li Liu et al. “Blood-brain barrier disruption with focused ultrasound enhances delivery of chemotherapeutic drugs for glioblastoma treatment”. In: *Radiology* 255.2 (2010), pp. 415–425 (cit. on p. 3).

[33] Antonios N Pouliopoulos et al. “A clinical system for non-invasive blood–brain barrier opening using a neuronavigation-guided single-element focused ultrasound transducer”. In: *Ultrasound in Medicine & Biology* 46.1 (2020), pp. 73–89 (cit. on pp. 3, 82, 102, 107).

[34] Meaghan A O’Reilly and Kullervo Hynynen. “Blood-brain barrier: Real-time feedback-controlled focused ultrasound disruption by using an acoustic emissions–based controller”. In: *Radiology* 263.1 (2012), pp. 96–106 (cit. on p. 3).

[35] JC Somer. “Electronic sector scanning for ultrasonic diagnosis”. In: *Ultrasonics* 6.3 (1968), pp. 153–159 (cit. on p. 3).

[36] Charles A Cain and Shin-ichiro Umemura. “Concentric-ring and sector-vortex phased-array applicators for ultrasound hyperthermia”. In: *IEEE Transactions on Microwave Theory and Techniques* 34.5 (1986), pp. 542–551 (cit. on p. 3).

[37] Emad S Ebbini et al. “A cylindrical-section ultrasound phased-array applicator for hyperthermia cancer therapy”. In: *IEEE Transactions on Ultrasonics, Ferroelectrics, and Frequency Control* 35.5 (1988), pp. 561–572 (cit. on p. 3).

[38] Kullervo Hynynen et al. “Feasibility of using ultrasound phased arrays for MRI monitored noninvasive surgery”. In: *IEEE Transactions on Ultrasonics, Ferroelectrics, and Frequency Control* 43.6 (1996), pp. 1043–1053 (cit. on p. 3).

[39] Emad S Ebbini and Charles A Cain. “Multiple-focus ultrasound phased-array pattern synthesis: optimal driving-signal distributions for hyperthermia”. In: *IEEE Transactions on Ultrasonics, Ferroelectrics, and Frequency Control* 36.5 (1989), pp. 540–548 (cit. on p. 3).

[40] Kullervo Hynynen and Ryan M Jones. “Image-guided ultrasound phased arrays are a disruptive technology for non-invasive therapy”. In: *Physics in Medicine & Biology* 61.17 (2016), R206 (cit. on p. 3).

[41] Stephen A Goss et al. “Sparse random ultrasound phased array for focal surgery”. In: *IEEE Transactions on Ultrasonics, Ferroelectrics, and Frequency Control* 43.6 (1996), pp. 1111–1121 (cit. on p. 3).

[42] JW Hand et al. “A random phased array device for delivery of high intensity focused ultrasound”. In: *Physics in Medicine & Biology* 54.19 (2009), p. 5675 (cit. on p. 3).

[43] Pascal Ramaekers et al. “Evaluation of a novel therapeutic focused ultrasound transducer based on Fermat’s spiral”. In: *Physics in Medicine & Biology* 62.12 (2017), p. 5021 (cit. on p. 4).

[44] Juanjuan Gu and Yun Jing. “Modeling of wave propagation for medical ultrasound: a review”. In: *IEEE Transactions on Ultrasonics, Ferroelectrics, and Frequency Control* 62.11 (2015), pp. 1979–1992 (cit. on p. 4).

[45] Xiaobing Fan and Kullervo Hynynen. “Ultrasound surgery using multiple sonications’ treatment time considerations”. In: *Ultrasound in Medicine & Biology* 22.4 (1996), pp. 471–482 (cit. on p. 4).

[46] Ari Partanen et al. “Reduction of peak acoustic pressure and shaping of heated region by use of multifoci sonications in MR-guided high-intensity focused ultra-

sound mediated mild hyperthermia". In: *Medical Physics* 40.1 (2013), p. 013301 (cit. on pp. 4, 60).

[47] Jean-François Aubry et al. "Experimental demonstration of noninvasive transskull adaptive focusing based on prior computed tomography scans". In: *The Journal of the Acoustical Society of America* 113.1 (2003), pp. 84–93 (cit. on p. 4).

[48] Nir Lipsman et al. "Blood–brain barrier opening in Alzheimer's disease using MR-guided focused ultrasound". In: *Nature Communications* 9.1 (2018), pp. 1–8 (cit. on pp. 4, 82).

[49] Ko-Ting Chen et al. "Neuronavigation-guided focused ultrasound for transcranial blood-brain barrier opening and immunostimulation in brain tumors". In: *Science Advances* 7.6 (2021), eabd0772 (cit. on p. 4).

[50] Matti Tillander et al. "High intensity focused ultrasound induced in vivo large volume hyperthermia under 3D MRI temperature control". In: *Medical Physics* 43.3 (2016), pp. 1539–1549 (cit. on pp. 4, 46, 60, 82).

[51] Kai Melde et al. "Holograms for acoustics". In: *Nature* 537.7621 (2016), pp. 518–522 (cit. on pp. 4, 10, 15, 23, 24, 46, 48, 66, 83, 88, 106, 113).

[52] Luke Cox et al. "Acoustic hologram enhanced phased arrays for ultrasonic particle manipulation". In: *Physical Review Applied* 12.6 (2019), p. 064055 (cit. on p. 4).

[53] Michael D Brown, Ben T Cox, and Bradley E Treeby. "Design of multi-frequency acoustic kinoforms". In: *Applied Physics Letters* 111.24 (2017) (cit. on pp. 4, 46, 101, 106).

[54] Michael D Brown, Ben T Cox, and Bradley E Treeby. "Stackable acoustic holograms". In: *Applied Physics Letters* 116.26 (2020), p. 261901 (cit. on p. 5).

[55] Michael D Brown. "Phase and amplitude modulation with acoustic holograms". In: *Applied Physics Letters* 115.5 (2019), p. 053701 (cit. on pp. 5, 24, 106).

[56] Kai Melde et al. "Compact holographic sound fields enable rapid one-step assembly of matter in 3D". In: *Science Advances* 9.6 (2023), eadf6182 (cit. on pp. 5, 107, 145).

[57] Athanasios G Athanassiadis et al. “Multi-plane Diffractive Acoustic Networks”. In: *IEEE Transactions on Ultrasonics, Ferroelectrics, and Frequency Control* (2023) (cit. on p. 5).

[58] Zhichao Ma et al. “Acoustic holographic cell patterning in a biocompatible hydrogel”. In: *Advanced Materials* 32.4 (2020), p. 1904181 (cit. on pp. 5, 46, 107).

[59] Jinwook Kim et al. “Acoustic holograms for directing arbitrary cavitation patterns”. In: *Applied Physics Letters* 118.5 (2021), p. 051902 (cit. on pp. 5, 46, 107).

[60] Akshay Randad et al. “Design, fabrication, and characterization of broad beam transducers for fragmenting large renal calculi with burst wave lithotripsy”. In: *The Journal of the Acoustical Society of America* 148.1 (2020), pp. 44–50 (cit. on pp. 5, 46).

[61] Guillaume Maimbourg et al. “3D-printed adaptive acoustic lens as a disruptive technology for transcranial ultrasound therapy using single-element transducers”. In: *Physics in Medicine & Biology* 63.2 (2018), p. 025026 (cit. on pp. 5, 10, 24, 25, 46, 83, 107).

[62] Guillaume Maimbourg et al. “Steering capabilities of an acoustic lens for transcranial therapy: numerical and experimental studies”. In: *IEEE Transactions on Biomedical Engineering* 67.1 (2019), pp. 27–37 (cit. on pp. 5, 83).

[63] Sergio Jiménez-Gambín et al. “Holograms to focus arbitrary ultrasonic fields through the skull”. In: *Physical Review Applied* 12.1 (2019), p. 014016 (cit. on pp. 5, 10, 24, 46–48, 56, 83, 85, 88, 107, 113).

[64] Sergio Jiménez-Gambín, Noé Jiménez, and Francisco Camarena. “Transcranial focusing of ultrasonic vortices by acoustic holograms”. In: *Physical Review Applied* 14.5 (2020), p. 054070 (cit. on pp. 5, 10, 46, 83, 88, 107).

[65] Sergio Jiménez-Gambín et al. “Acoustic holograms for bilateral blood-brain barrier opening in a mouse model”. In: *IEEE Transactions on Biomedical Engineering* 69.4 (2021), pp. 1359–1368 (cit. on pp. 5, 46, 83, 107, 128).

[66] Jiaru He et al. “Multitarget transcranial ultrasound therapy in small animals based on phase-only acoustic holographic lens”. In: *IEEE Transactions on Ultrasonics,*

Ferroelectrics, and Frequency Control 69.2 (2021), pp. 662–671 (cit. on pp. 5, 107, 128).

[67] Geon Kook et al. “Multifocal skull-compensated transcranial focused ultrasound system for neuromodulation applications based on acoustic holography”. In: *Microsystems & Nanoengineering* 9.1 (2023), p. 45 (cit. on p. 5).

[68] Jeffrey K Woodacre, Thomas G Landry, and Jeremy A Brown. “A low-cost miniature histotripsy transducer for precision tissue ablation”. In: *IEEE Transactions on Ultrasonics, Ferroelectrics, and Frequency Control* 65.11 (2018), pp. 2131–2140 (cit. on p. 9).

[69] Ralph E Beard et al. “An annular focus ultrasonic lens for local hyperthermia treatment of small tumors”. In: *Ultrasound in Medicine & Biology* 8.2 (1982), pp. 177–184 (cit. on p. 9).

[70] Todd Fjield et al. “Design and experimental verification of thin acoustic lenses for the coagulation of large tissue volumes”. In: *Physics in Medicine & Biology* 42.12 (1997), p. 2341 (cit. on p. 9).

[71] Todd Fjield, Christina Elise Silcox, and Kullervo Hynynen. “Low-profile lenses for ultrasound surgery”. In: *Physics in Medicine & Biology* 44.7 (1999), p. 1803 (cit. on p. 10).

[72] Daniel Tarrazó-Serrano et al. “Acoustic focusing enhancement in fresnel zone plate lenses”. In: *Scientific Reports* 9.1 (2019), p. 7067 (cit. on p. 10).

[73] Noé Jiménez et al. “Sharp acoustic vortex focusing by Fresnel-spiral zone plates”. In: *Applied Physics Letters* 112.20 (2018), p. 204101 (cit. on pp. 10, 46).

[74] Xia Wu and Michael Sherar. “Theoretical evaluation of moderately focused spherical transducers and multi-focus acoustic lens/transducer systems for ultrasound thermal therapy”. In: *Physics in Medicine & Biology* 47.9 (2002), p. 1603 (cit. on p. 10).

[75] Ron Lalonde, Arthur Worthington, and JW Hunt. “Hyperthermia: Field conjugate acoustic lenses for deep heating”. In: *[1990] Proceedings of the Twelfth Annual International Conference of the IEEE Engineering in Medicine and Biology Society*. IEEE. 1990, pp. 264–265 (cit. on p. 10).

[76] Bradley E Treeby et al. “Modeling nonlinear ultrasound propagation in heterogeneous media with power law absorption using a k-space pseudospectral method”. In: *The Journal of the Acoustical Society of America* 131.6 (2012), pp. 4324–4336 (cit. on pp. 13, 37, 50).

[77] Josep Rodríguez-Sendra, Alicia Carrión, and Francisco Camarena. “Ultrasonic Measurement of Orthotropic Elastic Constants of 3D-Printed Photopolymer Materials”. In: *2022 IEEE International Ultrasonics Symposium (IUS)*. 2022, pp. 1–3. DOI: 10.1109/IUS54386.2022.9957208 (cit. on p. 15).

[78] JM Mi Pinkerton. “The absorption of ultrasonic waves in liquids and its relation to molecular constitution”. In: *Proceedings of the Physical Society. Section B* 62.2 (1949), p. 129 (cit. on pp. 15, 66).

[79] Uwe Schneider, Eros Pedroni, and Antony Lomax. “The calibration of CT Hounsfield units for radiotherapy treatment planning”. In: *Physics in Medicine & Biology* 41.1 (1996), p. 111 (cit. on pp. 15, 85, 114).

[80] T Douglas Mast. “Empirical relationships between acoustic parameters in human soft tissues”. In: *Acoustics Research Letters Online* 1.2 (2000), pp. 37–42 (cit. on pp. 15, 85, 114).

[81] Richard SC Cobbold. *Foundations of biomedical ultrasound*. Oxford university press, 2006 (cit. on pp. 15, 85, 114).

[82] Asier Marzo and Bruce W Drinkwater. “Holographic acoustic tweezers”. In: *Proceedings of the National Academy of Sciences* 116.1 (2019), pp. 84–89 (cit. on p. 24).

[83] Tatsuki Fushimi, Kenta Yamamoto, and Yoichi Ochiai. “Acoustic hologram optimisation using automatic differentiation”. In: *Scientific Reports* 11.1 (2021), pp. 1–10 (cit. on pp. 24, 78, 145).

[84] Scott Schoen and Costas D Arvanitis. “Heterogeneous angular spectrum method for trans-skull imaging and focusing”. In: *IEEE transactions on medical imaging* 39.5 (2019), pp. 1605–1614 (cit. on p. 24).

[85] Larry Schlussler. “The design and test results for an acoustic lens with elliptic surfaces”. In: *The Journal of the Acoustical Society of America* 67.2 (1980), pp. 699–701 (cit. on p. 31).

[86] Gregory T Clement, Hideyuki Nomura, and Tomoo Kamakura. “Ultrasound field measurement using a binary lens”. In: *IEEE Transactions on Ultrasonics, Ferroelectrics, and Frequency Control* 62.2 (2015), pp. 350–359 (cit. on p. 31).

[87] David T Blackstock. *Fundamentals of physical acoustics*. 2001 (cit. on p. 33).

[88] Andrea Cafarelli et al. “Speed of sound in rubber-based materials for ultrasonic phantoms”. In: *Journal of Ultrasound* 19 (2016), pp. 251–256 (cit. on p. 34).

[89] Noe Jimenez et al. “Acoustic Bessel-like beam formation by an axisymmetric grating”. In: *Europhysics Letters (EPL)* 106.2 (2014), p. 24005 (cit. on p. 37).

[90] Li Deng. “The mnist database of handwritten digit images for machine learning research”. In: *IEEE Signal Processing Magazine* 29.6 (2012), pp. 141–142 (cit. on p. 41).

[91] Zhou Wang et al. “Image quality assessment: from error visibility to structural similarity”. In: *IEEE Transactions on Image Processing* 13.4 (2004), pp. 600–612 (cit. on p. 41).

[92] Dennis Gabor. “A new microscopic principle”. In: *Nature* 161 (1948), pp. 777–778 (cit. on pp. 45, 106).

[93] Y Hertzberg and G Navon. “Bypassing absorbing objects in focused ultrasound using computer generated holographic technique”. In: *Medical Physics* 38.12 (2011), pp. 6407–6415 (cit. on pp. 45, 106).

[94] Peng Zhang et al. “Generation of acoustic self-bending and bottle beams by phase engineering”. In: *Nature Communications* 5.1 (2014), pp. 1–9 (cit. on p. 46).

[95] MD Brown et al. “Generating arbitrary ultrasound fields with tailored optoacoustic surface profiles”. In: *Applied Physics Letters* 110.9 (2017), p. 094102 (cit. on pp. 46, 106).

[96] Michael D Brown et al. “Control of broadband optically generated ultrasound pulses using binary amplitude holograms”. In: *The Journal of the Acoustical Society of America* 139.4 (2016), pp. 1637–1647 (cit. on pp. 46, 106).

[97] Yangbo Xie et al. “Acoustic holographic rendering with two-dimensional metamaterial-based passive phased array”. In: *Scientific Reports* 6.1 (2016), pp. 1–6 (cit. on p. 46).

[98] Ye Tian et al. “Acoustic holography based on composite metasurface with decoupled modulation of phase and amplitude”. In: *Applied Physics Letters* 110.19 (2017), p. 191901 (cit. on p. 46).

[99] Gianluca Memoli et al. “Metamaterial bricks and quantization of meta-surfaces”. In: *Nature Communications* 8.1 (2017), pp. 1–8 (cit. on p. 46).

[100] Yifan Zhu et al. “Fine manipulation of sound via lossy metamaterials with independent and arbitrary reflection amplitude and phase”. In: *Nature Communications* 9.1 (2018), pp. 1–9 (cit. on pp. 46, 106).

[101] Asier Marzo et al. “Holographic acoustic elements for manipulation of levitated objects”. In: *Nature Communications* 6.1 (2015), pp. 1–7 (cit. on pp. 46, 107).

[102] Mohd Adili Norasikin et al. “SoundBender: dynamic acoustic control behind obstacles”. In: *Proceedings of the 31st Annual ACM Symposium on User Interface Software and Technology*. 2018, pp. 247–259 (cit. on p. 46).

[103] Noé Jiménez, Jean-Philippe Groby, and Vicent Romero-García. “Spiral sound-diffusing metasurfaces based on holographic vortices”. In: *Scientific Reports* 11.1 (2021), pp. 1–13 (cit. on pp. 46, 107).

[104] Kai Melde et al. “Acoustic fabrication via the assembly and fusion of particles”. In: *Advanced Materials* 30.3 (2018), p. 1704507 (cit. on p. 46).

[105] Tatsuki Fushimi et al. “Acoustophoretic volumetric displays using a fast-moving levitated particle”. In: *Applied Physics Letters* 115.6 (2019), p. 064101 (cit. on p. 46).

[106] Pieter Kruizinga et al. “Compressive 3D ultrasound imaging using a single sensor”. In: *Science advances* 3.12 (2017), e1701423 (cit. on pp. 46, 107).

[107] Diana Andrés et al. “Numerical study of acoustic holograms for deep-brain targeting through the temporal bone window”. In: *Ultrasound in Medicine & Biology* 48.5 (2022), pp. 872–886 (cit. on pp. 46, 107).

[108] Thomas L Szabo. *Diagnostic ultrasound imaging: inside out*. Academic press, 2004 (cit. on p. 46).

[109] Jean-Michel Escoffre and Ayache Bouakaz. *Therapeutic ultrasound*. Vol. 880. Springer, 2015 (cit. on p. 46).

[110] Andreas Blana et al. “High-intensity focused ultrasound for the treatment of localized prostate cancer: 5-year experience”. In: *Urology* 63.2 (2004), pp. 297–300 (cit. on p. 46).

[111] Seiko Toraya-Brown and Steven Fiering. “Local tumour hyperthermia as immunotherapy for metastatic cancer”. In: *International Journal of Hyperthermia* 30.8 (2014), pp. 531–539 (cit. on p. 46).

[112] Matthew Mallory et al. “Therapeutic hyperthermia: The old, the new, and the upcoming”. In: *Critical Reviews in Oncology/Hematology* 97 (2016), pp. 56–64 (cit. on p. 46).

[113] Faheez Mohamed et al. “Thermal enhancement of new chemotherapeutic agents at moderate hyperthermia”. In: *Annals of Surgical Oncology* 10.4 (2003), pp. 463–468 (cit. on p. 46).

[114] Robert Staruch, Rajiv Chopra, and Kullervo Hynynen. “Hyperthermia in bone generated with MR imaging–controlled focused ultrasound: Control strategies and drug delivery”. In: *Radiology* 263.1 (2012), pp. 117–127 (cit. on p. 46).

[115] Chenchen Bing et al. “Drift correction for accurate PRF-shift MR thermometry during mild hyperthermia treatments with MR-HIFU”. In: *International Journal of Hyperthermia* 32.6 (2016), pp. 673–687 (cit. on p. 46).

[116] Navid Farr et al. “Hyperthermia-enhanced targeted drug delivery using magnetic resonance-guided focussed ultrasound: a pre-clinical study in a genetic model of pancreatic cancer”. In: *International Journal of Hyperthermia* 34.3 (2018), pp. 284–291 (cit. on p. 46).

[117] Bradley E Treeby and Benjamin T Cox. "k-Wave: MATLAB toolbox for the simulation and reconstruction of photoacoustic wave fields". In: *Journal of Biomedical Optics* 15.2 (2010), p. 021314 (cit. on pp. 47, 66, 86, 110, 114).

[118] Robert L Mcintosh and Vitas Anderson. "A comprehensive tissue properties database provided for the thermal assessment of a human at rest". In: *Biophysical Reviews and Letters* 5.03 (2010), pp. 129–151 (cit. on pp. 48, 50).

[119] Bruce E Hammer. "Physical properties of tissues". In: *Radiology* 181.1 (1991), pp. 128–128 (cit. on pp. 48, 49).

[120] Francis A. Duck. "Chapter 4 - Acoustic properties of tissue at ultrasonic frequencies". In: *Physical Properties of Tissues*. Ed. by Francis A. Duck. London: Academic Press, 1990, pp. 73–135. ISBN: 978-0-12-222800-1. DOI: https://doi.org/10.1016/B978-0-12-222800-1.50008-5 (cit. on p. 48).

[121] EJ Jackson, CC Coussios, and RO Cleveland. "Nonlinear acoustic properties of ex vivo bovine liver and the effects of temperature and denaturation". In: *Physics in Medicine & Biology* 59.12 (2014), p. 3223 (cit. on p. 49).

[122] Mark F Hamilton. "Effective Gol'dberg number for diverging waves". In: *The Journal of the Acoustical Society of America* 140.6 (2016), pp. 4419–4427 (cit. on p. 49).

[123] Harry H Pennes. "Analysis of tissue and arterial blood temperatures in the resting human forearm". In: *Journal of Applied Physiology* 1.2 (1948), pp. 93–122 (cit. on pp. 49, 67).

[124] NR Datta et al. "Local hyperthermia combined with radiotherapy and-/or chemotherapy: Recent advances and promises for the future". In: *Cancer Treatment Reviews* 41.9 (2015), pp. 742–753 (cit. on p. 60).

[125] Gianfranco Baronzio, Alberto Gramaglia, and Gianmaria Fiorentini. "Hyperthermia and immunity. A brief overview". In: *In Vivo* 20.6A (2006), pp. 689–695 (cit. on p. 60).

[126] H Petra Kok et al. "Heating technology for malignant tumors: A review". In: *International Journal of Hyperthermia* 37.1 (2020), pp. 711–741 (cit. on p. 60).

[127] Gail ter Haar and Constantin Coussios. “High intensity focused ultrasound: physical principles and devices”. In: *International Journal of Hyperthermia* 23.2 (2007), pp. 89–104 (cit. on p. 60).

[128] Brendon M Baker and Christopher S Chen. “Deconstructing the third dimension–how 3D culture microenvironments alter cellular cues”. In: *Journal of Cell Science* 125.13 (2012), pp. 3015–3024 (cit. on pp. 60, 68).

[129] Petros XE Mouratidis et al. “Relationship between thermal dose and cell death for ’rapid’ ablative and ’slow’ hyperthermic heating”. In: *International Journal of Hyperthermia* 36.1 (2019), pp. 228–242 (cit. on pp. 60, 68, 76).

[130] Petros XE Mouratidis, Ian Rivens, and Gail Ter Haar. “A study of thermal dose-induced autophagy, apoptosis and necroptosis in colon cancer cells”. In: *International Journal of Hyperthermia* 31.5 (2015), pp. 476–488 (cit. on pp. 60, 68, 76).

[131] Sarah C Brüningk et al. “3D tumour spheroids for the prediction of the effects of radiation and hyperthermia treatments”. In: *Scientific Reports* 10.1 (2020), p. 1653 (cit. on p. 60).

[132] Silke Roovers et al. “Sonoprinting liposomes on tumor spheroids by microbubbles and ultrasound”. In: *Journal of Controlled Release* 316 (2019), pp. 79–92 (cit. on p. 60).

[133] Miglė Paškevičiūtė et al. “Evaluation of low-intensity pulsed ultrasound on doxorubicin delivery in 2D and 3D cancer cell cultures”. In: *Scientific Reports* 10.1 (2020), pp. 1–8 (cit. on p. 60).

[134] Lisa Landgraf et al. “Focused ultrasound treatment of a spheroid in vitro tumour model”. In: *Cells* 11.9 (2022), p. 1518 (cit. on p. 60).

[135] William Chu et al. “Magnetic Resonance–Guided high-intensity focused ultrasound hyperthermia for recurrent rectal cancer: MR thermometry evaluation and preclinical validation”. In: *International Journal of Radiation Oncology, Biology, Physics* 95.4 (2016), pp. 1259–1267 (cit. on p. 60).

[136] Eugene Ozhinsky et al. “MR thermometry-guided ultrasound hyperthermia of user-defined regions using the ExAblate prostate ablation array”. In: *Journal of Therapeutic Ultrasound* 6.1 (2018), pp. 1–10 (cit. on p. 60).

[137] Oleg A Sapozhnikov et al. “Acoustic holography as a metrological tool for characterizing medical ultrasound sources and fields”. In: *The Journal of the Acoustical Society of America* 138.3 (2015), pp. 1515–1532 (cit. on pp. 63, 69, 106, 108).

[138] *IEC 60601-2-5:2015: Medical electrical equipment Part 2-37: Particular requirements for the basic safety and essential performance of ultrasonic physiotherapy equipment*. Standard. Geneva, CH: International Electrotechnical Commission, 2015 (cit. on p. 64).

[139] Lisa Braunstein et al. “Characterization of acoustic, cavitation, and thermal properties of poly (vinyl alcohol) hydrogels for use as therapeutic ultrasound tissue mimics”. In: *Ultrasound in Medicine & Biology* 48.6 (2022), pp. 1095–1109 (cit. on p. 64).

[140] Hugh Morris et al. “Investigation of the viscous heating artefact arising from the use of thermocouples in a focused ultrasound field”. In: *Physics in Medicine & Biology* 53.17 (2008), p. 4759 (cit. on p. 65).

[141] Stephen A Sapareto and William C Dewey. “Thermal dose determination in cancer therapy”. In: *International Journal of Radiation Oncology, Biology, Physics* 10.6 (1984), pp. 787–800 (cit. on p. 66).

[142] Frank E Jones and Georgia L Harris. “ITS-90 density of water formulation for volumetric standards calibration”. In: *Journal of Research of the National Institute of Standards and Technology* 97.3 (1992), p. 335 (cit. on p. 66).

[143] Wojciech Marczak. “Water as a standard in the measurements of speed of sound in liquids”. In: *The Journal of the Acoustical Society of America* 102.5 (1997), pp. 2776–2779 (cit. on p. 66).

[144] Constantine Coussios et al. “Role of acoustic cavitation in the delivery and monitoring of cancer treatment by high-intensity focused ultrasound (HIFU)”. In: *International Journal of Hyperthermia* 23.2 (2007), pp. 105–120 (cit. on p. 77).

[145] Dongxin Yang et al. “The influence of ultrasound-induced microbubble cavitation on the viability, migration and cell cycle distribution of melanoma cells”. In: *Applied Acoustics* 179 (2021), p. 108056 (cit. on p. 77).

[146] Puja Mishra, Martyn Hill, and Peter Glynne-Jones. “Deformation of red blood cells using acoustic radiation forces”. In: *Biomicrofluidics* 8.3 (2014), p. 034109 (cit. on p. 77).

[147] Walter Duco et al. “Generation of ROS mediated by mechanical waves (ultrasound) and its possible applications”. In: *Methods* 109 (2016), pp. 141–148 (cit. on p. 77).

[148] Katarzyna Kaczmarek et al. “Heating induced by therapeutic ultrasound in the presence of magnetic nanoparticles”. In: *ACS Applied Materials & Interfaces* 10.14 (2018), pp. 11554–11564 (cit. on p. 78).

[149] Subhashish Dasgupta et al. “Beam localization in HIFU temperature measurements using thermocouples, with application to cooling by large blood vessels”. In: *Ultrasonics* 51.2 (2011), pp. 171–180 (cit. on p. 78).

[150] Edwin L Carstensen. “Interaction of ultrasound with tissues”. In: *Ultrasound in Medicine*. Springer, 1976, pp. 517–517 (cit. on p. 82).

[151] Daniel Coluccia et al. “First noninvasive thermal ablation of a brain tumor with MR-guided focusedultrasound”. In: *Journal of Therapeutic Ultrasound* 2.1 (2014), pp. 1–7 (cit. on pp. 82, 107).

[152] Jonathan R Sukovich et al. “In vivo histotripsy brain treatment”. In: *Journal of Neurosurgery* 131.4 (2018), pp. 1331–1338 (cit. on p. 82).

[153] Nathan McDannold et al. “Temporary disruption of the blood–brain barrier by use of ultrasound and microbubbles: safety and efficacy evaluation in rhesus macaques”. In: *Cancer Research* 72.14 (2012), pp. 3652–3663 (cit. on p. 82).

[154] Elisa E Konofagou et al. “Ultrasound-induced blood-brain barrier opening”. In: *Current Pharmaceutical Biotechnology* 13.7 (2012), pp. 1332–1345 (cit. on pp. 82, 107, 128).

[155] Wynn Legon et al. “A retrospective qualitative report of symptoms and safety from transcranial focused ultrasound for neuromodulation in humans”. In: *Scientific Reports* 10.1 (2020), pp. 1–10 (cit. on p. 82).

[156] Catherine Horodyckid et al. “Safe long-term repeated disruption of the blood-brain barrier using an implantable ultrasound device: a multiparametric study in a primate model”. In: *Journal of Neurosurgery* 126.4 (2017), pp. 1351–1361 (cit. on p. 82).

[157] Chris Adams et al. “Implementation of a skull-conformal phased array for transcranial focused ultrasound therapy”. In: *IEEE Transactions on Biomedical Engineering* 68.11 (2021), pp. 3457–3468 (cit. on p. 83).

[158] Christopher W Connor and Kullervo Hynynen. “Patterns of thermal deposition in the skull during transcranial focused ultrasound surgery”. In: *IEEE Transactions on Biomedical Engineering* 51.10 (2004), pp. 1693–1706 (cit. on p. 84).

[159] Jie Sun and Kullervo Hynynen. “Focusing of therapeutic ultrasound through a human skull: a numerical study”. In: *The Journal of the Acoustical Society of America* 104.3 (1998), pp. 1705–1715 (cit. on p. 84).

[160] Weibao Qiu et al. “Ultrasound for the brain: A review of physical and engineering principles, and clinical applications”. In: *IEEE Transactions on Ultrasonics, Ferroelectrics, and Frequency Control* 68.1 (2020), pp. 6–20 (cit. on p. 84).

[161] Rune Aaslid, Thomas-Marc Markwalder, and Helge Nornes. “Noninvasive transcranial Doppler ultrasound recording of flow velocity in basal cerebral arteries”. In: *Journal of Neurosurgery* 57.6 (1982), pp. 769–774 (cit. on p. 84).

[162] Edward G Jones. *The thalamus*. Springer Science & Business Media, 2012 (cit. on p. 84).

[163] Mark E Schafer et al. “Design, development, and operation of a low-intensity focused ultrasound pulsation (LIFUP) system for clinical use”. In: *IEEE Transactions on Ultrasonics, Ferroelectrics, and Frequency Control* 68.1 (2020), pp. 54–64 (cit. on p. 84).

[164] Wynn Legon et al. “Neuromodulation with single-element transcranial focused ultrasound in human thalamus”. In: *Human Brain Mapping* 39.5 (2018), pp. 1995–2006 (cit. on pp. 84, 101, 103).

[165] Martin M Monti et al. “Non-invasive ultrasonic thalamic stimulation in disorders of consciousness after severe brain injury: a first-in-man report”. In: *Brain Stimulation* 9.6 (2016), pp. 940–941 (cit. on pp. 84, 85).

[166] Shih-Ying Wu et al. “Efficient blood-brain barrier opening in primates with neuronavigation-guided ultrasound and real-time acoustic mapping”. In: *Scientific Reports* 8.1 (2018), pp. 1–11 (cit. on p. 84).

[167] James Robertson et al. “Sensitivity of simulated transcranial ultrasound fields to acoustic medium property maps”. In: *Physics in Medicine & Biology* 62.7 (2017), p. 2559 (cit. on p. 85).

[168] Paul A Yushkevich et al. “User-guided 3D active contour segmentation of anatomical structures: significantly improved efficiency and reliability”. In: *Neuroimage* 31.3 (2006), pp. 1116–1128 (cit. on p. 85).

[169] Jianqing Li et al. “Comparison of balanced direct search and iterative angular spectrum approaches for designing acoustic holography structure”. In: *Applied Acoustics* 175 (2021), p. 107848 (cit. on p. 101).

[170] Zhichao Ma et al. “Spatial ultrasound modulation by digitally controlling microbubble arrays”. In: *Nature Communications* 11.1 (2020), pp. 1–7 (cit. on p. 103).

[171] Alexander F Metherell, Hussein Mohammed Amin El-Sum, and Lewis Larmore. *Acoustical holography*. Ed. by Lewis Larmore A. F. Metherell H. M. A. El-Sum. Vol. 1. Springer, 1969 (cit. on p. 106).

[172] Fredrick L Thurstone. “Holographic imaging with ultrasound”. In: *The Journal of the Acoustical Society of America* 45.4 (1969), pp. 895–899 (cit. on p. 106).

[173] Rolf K Mueller. “Acoustic holography”. In: *Proceedings of the IEEE* 59.9 (1971), pp. 1319–1335 (cit. on p. 106).

[174] Earl G Williams, James D Maynard, and Eugen Skudrzyk. “Sound source reconstructions using a microphone array”. In: *The Journal of the Acoustical Society of America* 68.1 (1980), pp. 340–344 (cit. on p. 106).

[175] Julian D Maynard, Earl G Williams, and Y Lee. “Nearfield acoustic holography: I. Theory of generalized holography and the development of NAH”. In: *The Journal of the Acoustical Society of America* 78.4 (1985), pp. 1395–1413 (cit. on p. 106).

[176] Wayne Kreider et al. “Characterization of a multi-element clinical HIFU system using acoustic holography and nonlinear modeling”. In: *IEEE Transactions on Ultrasonics, Ferroelectrics, and Frequency Control* 60.8 (2013), pp. 1683–1698 (cit. on pp. 106, 108).

[177] *IEC/TS62556 Ultrasonics-field characterization-specification and measurement of field parameters for high intensity therapeutic ultrasound (HITU) transducers and systems*. Tech. rep. Geneva: International Electrotechnical Commission, 2014 (cit. on p. 106).

[178] Bradley Treeby et al. “Equivalent-source acoustic holography for projecting measured ultrasound fields through complex media”. In: *IEEE Transactions on Ultrasonics, Ferroelectrics, and Frequency Control* 65.10 (2018), pp. 1857–1864 (cit. on p. 106).

[179] Yong Li et al. “Experimental realization of full control of reflected waves with subwavelength acoustic metasurfaces”. In: *Physical Review Applied* 2.6 (2014), p. 064002 (cit. on p. 106).

[180] Mingxin Xu et al. “Sound-speed modifying acoustic metasurfaces for acoustic holography”. In: *Advanced Materials* 35.14 (2023), p. 2208002 (cit. on p. 106).

[181] Sergio Jiménez-Gambín et al. “Generating Bessel beams with broad depth-of-field by using phase-only acoustic holograms”. In: *Scientific Reports* 9.1 (2019), p. 20104 (cit. on p. 107).

[182] Diana Andrés et al. “Thermal holographic patterns for ultrasound hyperthermia”. In: *Applied Physics Letters* 120.8 (2022) (cit. on pp. 107, 108).

[183] Diana Andrés et al. “Holographic focused ultrasound hyperthermia system for uniform Ssimultaneous thermal exposure of multiple tumor spheroids”. In: *Cancers* 15.9 (2023), p. 2540 (cit. on p. 107).

[184] Kullervo Hynynen. “MRI-guided focused ultrasound treatments”. In: *Ultrasonics* 50.2 (2010), pp. 221–229 (cit. on p. 107).

[185] Adamos Kyriakou et al. “A review of numerical and experimental compensation techniques for skull-induced phase aberrations in transcranial focused ultrasound”. In: *International Journal of Hyperthermia* 30.1 (2014), pp. 36–46 (cit. on p. 107).

[186] Joonho Seo et al. “Three-dimensional computer-controlled acoustic pressure scanning and quantification of focused ultrasound”. In: *IEEE Transactions on Ultrasonics, Ferroelectrics, and Frequency Control* 57.4 (2010), pp. 883–891 (cit. on p. 107).

[187] Eleanor Martin et al. “Rapid spatial mapping of focused ultrasound fields using a planar Fabry–Pérot sensor”. In: *IEEE Transactions on Ultrasonics, Ferroelectrics, and Frequency Control* 64.11 (2017), pp. 1711–1722 (cit. on p. 107).

[188] FL Thurstone, NI Kjosnes, and WM McKinney. “Ultrasonic scanning of biologic tissue by a new technique”. In: *Science* 149.3681 (1965), pp. 302–303 (cit. on p. 107).

[189] Andy R Harland, Jon N Petzing, and John R Tyrer. “Nonperturbing measurements of spatially distributed underwater acoustic fields using a scanning laser Doppler vibrometer”. In: *The Journal of the Acoustical Society of America* 115.1 (2004), pp. 187–195 (cit. on p. 107).

[190] WE Moore and JA Bucaro. “Measurement of acoustic fields using Schlieren and holographic techniques”. In: *The Journal of the Acoustical Society of America* 63.1 (1978), pp. 60–67 (cit. on p. 108).

[191] Kevin Martin and Richard Fernandez. “A thermal beam-shape phantom for ultrasound physiotherapy transducers”. In: *Ultrasound in Medicine & Biology* 23.8 (1997), pp. 1267–1274 (cit. on p. 108).

[192] K Melde, T Qiu, and P Fischer. “Fast spatial scanning of 3D ultrasound fields via thermography”. In: *Applied Physics Letters* 113.13 (2018), p. 133503 (cit. on p. 108).

[193] Mathias Fink. “Time reversal of ultrasonic fields. I. Basic principles”. In: *IEEE Transactions on Ultrasonics, Ferroelectrics, and Frequency Control* 39.5 (1992), pp. 555–566 (cit. on p. 110).

[194] Dong-Lai Liu and Robert C Waag. “Propagation and backpropagation for ultrasonic wavefront design”. In: *IEEE Transactions on Ultrasonics, Ferroelectrics, and Frequency Control* 44.1 (1997), pp. 1–13 (cit. on p. 111).

[195] Xiaozheng Zeng and Robert J McGough. “Evaluation of the angular spectrum approach for simulations of near-field pressures”. In: *The Journal of the Acoustical Society of America* 123.1 (2008), pp. 68–76 (cit. on p. 111).

[196] AZ Kaloev et al. “Spatial correction of an acoustic hologram for reconstructing surface vibrations of an axially symmetric ultrasound transducer”. In: *Acoustical Physics* 68.1 (2022), pp. 71–82 (cit. on p. 116).

[197] William M Pardridge. “Drug and gene delivery to the brain: the vascular route”. In: *Neuron* 36.4 (2002), pp. 555–558 (cit. on p. 127).

[198] N Joan Abbott and Ignacio A Romero. “Transporting therapeutics across the blood-brain barrier”. In: *Molecular Medicine Today* 2.3 (1996), pp. 106–113 (cit. on p. 127).

[199] Robert A Kroll and Edward A Neuwelt. “Outwitting the blood-brain barrier for therapeutic purposes: osmotic opening and other means”. In: *Neurosurgery* 42.5 (1998), pp. 1083–1099 (cit. on p. 128).

[200] NI Vykhodtseva, K Hynynen, and C Damianou. “Histologic effects of high intensity pulsed ultrasound exposure with subharmonic emission in rabbit brain in vivo”. In: *Ultrasound in Medicine & Biology* 21.7 (1995), pp. 969–979 (cit. on p. 128).

[201] Meaghan A O’Reilly, Olivia Hough, and Kullervo Hynynen. “Blood-brain barrier closure time after controlled ultrasound-induced opening is independent of

opening volume". In: *Journal of Ultrasound in Medicine* 36.3 (2017), pp. 475–483 (cit. on p. 128).

[202] Jessica F Jordão et al. "Antibodies targeted to the brain with image-guided focused ultrasound reduces amyloid-β plaque load in the TgCRND8 mouse model of Alzheimer's disease". In: *PLoS ONE* 5.5 (2010), e10549 (cit. on p. 128).

[203] Meaghan Anne O'Reilly et al. "Investigation of the safety of focused ultrasound-induced blood-brain barrier opening in a natural canine model of aging". In: *Theranostics* 7.14 (2017), p. 3573 (cit. on p. 128).

[204] Fabrice Marquet et al. "Noninvasive, transient and selective blood-brain barrier opening in non-human primates in vivo". In: *PloS one* 6.7 (2011), e22598 (cit. on p. 128).

[205] Matthew E Downs et al. "Blood-brain barrier opening in behaving non-human primates via focused ultrasound with systemically administered microbubbles". In: *Scientific Reports* 5.1 (2015), p. 15076 (cit. on p. 128).

[206] Agessandro Abrahao et al. "First-in-human trial of blood–brain barrier opening in amyotrophic lateral sclerosis using MR-guided focused ultrasound". In: *Nature Communications* 10.1 (2019), p. 4373 (cit. on p. 128).

[207] Javier Blesa et al. "BBB opening with focused ultrasound in nonhuman primates and Parkinson's disease patients: Targeted AAV vector delivery and PET imaging". In: *Science Advances* 9.16 (2023), eadf4888 (cit. on p. 128).

[208] N McDannold, N Vykhodtseva, and K Hynynen. "Targeted disruption of the blood–brain barrier with focused ultrasound: association with cavitation activity". In: *Physics in Medicine & Biology* 51.4 (2006), p. 793 (cit. on p. 134).

[209] Daniel L Adams et al. "A biocompatible titanium headpost for stabilizing behaving monkeys". In: *Journal of Neurophysiology* 98.2 (2007), pp. 993–1001 (cit. on p. 144).

[210] HAM Mahinda and O Prakash Murty. "Variability in thickness of human skull bones and sternum–An autopsy experience". In: *Journal of Forensic Medicine and Toxicology* 26.2 (2009), pp. 26–31 (cit. on p. 144).